Julius-Maximilians-Universität Würzburg
Graduate School of Science and Technology

Doctoral thesis / *Dissertation*
for the doctoral degree / *zur Erlangung des Doktorgrads*
Doctor rerum naturalium (Dr. rer. nat.)

Electrically Connected Nano-Optical Systems: From Refined Nanoscale Geometries to Selective Molecular Assembly

Elektrisch Kontaktierte Nano-Optische Systeme: Von Komplexen Geometrien bis zur Gezielten Oberflächenmodifikation

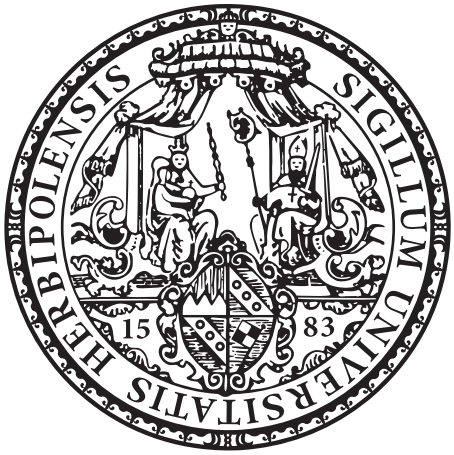

Submitted by / *Vorgelegt von*
Maximilian Thomas Ochs
from / aus
Rückers
Würzburg, 2022

Submitted on / *Eingereicht am:* .....

Stamp / *Stempel* Graduate School

Members of thesis committee / *Mitglieder des Promotionskomitees*

Chairperson / Vorsitz: .....

1. Reviewer and Examiner / 1. Gutachter und Prüfer: .....

2. Reviewer and Examiner / 2. Gutachter und Prüfer: .....

3. Examiner / 3. Prüfer: .....

Additional Examiners / Weitere Prüfer: .....

Day of thesis defense / *Tag des Promotionskolloquiums:* .....

To my family and my girlfriend Ezgi

List of Publications

This thesis is based on the following peer-reviewed articles.

Chapter 4 and 6: Reproduced and modified with permission from

René Kullock, **Maximilian Ochs**, Philipp Grimm, Monika Emmerling and Bert Hecht.
Electrically-driven Yagi-Uda antennas for Light.
Nature Communications 11, 115 (2020). doi.org/10.1038/s41467-019-14011-6.

Chapter 4 and 7: Reproduced and modified with permission from

Maximilian Ochs, Luka Zurak, Enno Krauss, Jessica Meier, Monika Emmerling, René Kullock and Bert Hecht.
Nanoscale Electrical Excitation of Distinct Modes in Plasmonic Waveguides.
Nano Letters 21 (10), 4225-4230 (2021). doi.org/10.1021/acs.nanolett.1c00182.

Furthermore, subsection 4.1.4 and chapter 5 are based on a manuscript currently in preparation:

Maximilian Ochs, Laurent Jucker, Maximilian Rödel, Monika Emmerling, René Kullock, Jens Pflaum, Marcel Mayor and Bert Hecht.
Site-Selective Functionalization of in-plane Nanoelectrode-Antennas.

Further articles by the author (not part of this thesis):

Laurent Jucker, **Maximilian Ochs**, René Kullock, Yves Aeschi, Bert Hecht and Marcel Mayor.
Development of Rotaxanes as E-Field-Sensitive Superstructures in Plasmonic Nano-Antennas.
Organic Materials 4, 127 (2022). doi.org/10.1055/a-1927-8947

René Kullock, Philipp Grimm, **Maximilian Ochs** and Bert Hecht.
Directed emission by electrically-driven optical antennas.
Proceedings Volume 10540, Quantum Sensing and Nano Electronics and Photonics XV; 1054012 (2018). doi.org/10.1117/12.2289647

Bert Hecht, René Kullock, **Maximilian Ochs**, Philipp Grimm, Luka Zurak, Patrick Pertsch, Daniel Friedrich, Jessica Meier, Benedikt Schurr and Monika Emmerling.
Electrically-driven Plasmonics.
Proceedings Volume 11462, Plasmonics: Design, Materials, Fabrication, Characterization, and Applications XVIII; 114620Q (2020).
doi.org/10.1117/12.2568370

Talks on international conferences:

Maximilian Ochs, René Kullock, Philipp Grimm and Bert Hecht.
Electroluminescence from optical Yagi-Uda antennas. DPG spring meeting. 2018 (Berlin, Germany).

Maximilian Ochs, René Kullock, Philipp Grimm and Bert Hecht.
Electroluminescence from optical Yagi-Uda antennas. NFO15. 2018 (Troyes, France).

Maximilian Ochs, René Kullock, Enno Krauss, Philipp Grimm, Monika Emmerling and Bert Hecht.
Nanoscale opto-electronic devices based on single-crystalline gold platelets. SPIE Photonics West. 2019 (San Francisco, United States of America).

Maximilian Ochs, Luka Zurak, Enno Krauss, Jessica Meier, Monika Emmerling, René Kullock and Bert Hecht.
Mode-selective electrical excitation of optical waveguides. NFO16. 2020 (Online).

Abstract

Metallic nano-optical systems allow to confine and guide light at the nanoscale, a fascinating ability which has motivated a wide range of fundamental as well as applied research over the last two decades. While optical antennas provide a link between visible radiation and localized energy, plasmonic waveguides route light in predefined pathways. So far, however, most experimental demonstrations are limited to purely optical excitations, *i.e.* isolated structures are illuminated by external lasers. Driving such systems electrically and generating light at the nanoscale, would greatly reduce the device footprint and pave the road for integrated optical nanocircuitry. Yet, the light emission mechanism as well as connecting delicate nanostructures to external electrodes pose key challenges and require sophisticated fabrication techniques. This work presents various electrically connected nano-optical systems and outlines a comprehensive production line, thus significantly advancing the state of the art. Importantly, the electrical connection is not just used to generate light, but also offers new strategies for device assembly. In a first example, nanoelectrodes are selectively functionalized with self-assembled monolayers by charging a specific electrode. This allows to tailor the surface properties of nanoscale objects, introducing an additional degree of freedom to the development of metal-organic nanodevices. In addition, the electrical connection enables the bottom-up fabrication of tunnel junctions by feedback-controlled dielectrophoresis. The resulting tunnel barriers are then used to generate light in different nano-optical systems via inelastic electron tunneling. Two structures are discussed in particular: optical Yagi-Uda antennas and plasmonic waveguides. Their refined geometries, accurately fabricated via focused ion beam milling of single-crystalline gold platelets, determine the properties of the emitted light. It is shown experimentally, that Yagi-Uda antennas radiate light in a specific direction with unprecedented directionality, while plasmonic waveguides allow to switch between the excitation of two propagating modes with orthogonal near-field symmetry. The presented devices nicely demonstrate the potential of electrically connected nano-optical systems, and the fabrication scheme including dielectrophoresis as well as site-selective functionalization will inspire more research in the field of nano-optoelectronics. In this context, different future experiments are discussed, ranging from the control of molecular machinery to optical antenna communication.

Kurzfassung

Nano-optische Systeme ermöglichen es, Licht auf der Nanoskala zu fokussieren und zu leiten - eine faszinierende Fähigkeit, die in den letzten zwei Jahrzehnten ein breites Spektrum an Grundlagen- und angewandter Forschung motiviert hat. Während optische Antennen lokalisierte Energie mit sichtbarer Strahlung verknüpfen, leiten plasmonische Wellenleiter das Licht in vordefinierte Bahnen. Bislang jedoch beschränken sich die meisten Experimente auf isolierte Strukturen, die durch externe Lichtquellen angeregt werden. Die elektrisch getriebene Lichterzeugung auf der Nanoskala reduziert den Platzbedarf dieser Systeme erheblich und ebnet so den Weg für optische Nano-Schaltkreise. Allerdings stellen sowohl die Lichtemission als auch die Kontaktierung der Nanostrukturen erhebliche Herausforderungen dar. In dieser Arbeit werden verschiedene elektrisch kontaktierte nano-optische Systeme vorgestellt. Eine zentrale Rolle spielt dabei die Kontaktierung - nicht nur für die Lichterzeugung, sondern auch für die Fabrikation der jeweiligen Strukturen. In einem ersten Beispiel werden Nanoelektroden durch Anlegen einer Spannung selektiv mit molekularen Monolagen beschichtet. Dadurch können die chemischen und elektronischen Oberflächeneigenschaften von Nanoobjekten maßgeschneidert werden, was einen zusätzlichen Freiheitsgrad bei der Entwicklung von optoelektronischen Nanosystemen darstellt. Darüber hinaus ermöglicht die elektrische Kontaktierung die Herstellung von Tunnelbarrieren mittels Dielektrophorese, was die Lichterzeugung in verschiedenen nano-optischen Systemen durch inelastisches Elektronentunneln ermöglicht. Hier werden zwei Strukturen diskutiert: optische Yagi-Uda-Antennen und plasmonische Wellenleiter. Ihre ausgeklügelten Geometrien, hergestellt aus einkristallinen Goldflocken mittels fokussiertem Ionenstrahl, bestimmen die Eigenschaften des emittierten Lichts. Es wird gezeigt, dass Yagi-Uda-Antennen das Licht gezielt in eine bestimmte Richtung abstrahlen, während plasmonische Wellenleiter das Schalten zwischen zwei propagierenden Moden ermöglichen. Damit demonstriert diese Arbeit das Potenzial von elektrisch kontaktierten nano-optischen Systemen und wird - in Kombination mit Dielektrophorese und selektiver Funktionalisierung - weitere Forschungen auf dem Gebiet der Nano-Optoelektronik anregen. In diesem Zusammenhang werden verschiedene zukünftige Experimente, von der Steuerung molekularer Maschinen bis zur optischen Antennenkommunikation, diskutiert.

Contents

1 Introduction **1**

2 Theory of Metallic Nano-Optical Systems **7**

2.1 Gold at Optical Frequencies - Rise of the Surface Plasmon 8

2.2 Optical Nanoantennas 11

2.2.1 From Classical to Optical Antennas 12

2.2.2 Electrically Driven Optical Antennas 17

2.2.3 The Yagi-Uda Design 22

2.3 Plasmonic Waveguides 25

2.3.1 Basic Geometry - The Two-Wire Transmission Line 25

2.3.2 Electrically Driven Plasmonic Waveguides 27

3 Introduction to Surface Modification **31**

3.1 Self-Assembled Monolayers on Gold Surfaces 32

3.2 Tuning the Metal Work Function 35

3.3 Electrochemical Desorption of Self-Assembled Monolayers 36

4 Experimental Techniques **39**

4.1 Sample Fabrication 40

4.1.1 General Sample Layout and Preparation 40

4.1.2 Focused Ion Beam Milling 41

4.1.3 Dielectrophoresis 44

4.1.4 Preparation of Self-Assembled Monolayers 47

4.2 Characterization of Nano-Optical Systems 47

4.2.1 White-Light Dark-Field Scattering 47

4.2.2 Electroluminescence and Current Measurements 49

4.2.3 Photoluminescence 50

4.2.4 Kelvin Probe Force Microscopy 50

5 Site-Selective Functionalization of Nanoantenna Electrodes **55**
5.1 Introduction 55
5.2 Molecular Desorption from Nanoscale Electrodes 58
5.3 Tuning the Current-Voltage Characteristics of Nanoantennas . . 64
5.4 Conclusion and Outlook: Towards Supramolecular Motion Controlled by Nanoantennas 66

6 Electrically Driven Optical Yagi-Uda Antennas **69**
6.1 Introduction 69
6.2 Structure Design 71
6.3 Feedback-Controlled Dielectrophoresis 73
6.4 Performance and Limits of Optical Yagi-Uda Antennas 75
6.5 Conclusion and Outlook: Towards Nanoantenna Communication 81

7 Nanoscale Electrical Excitation of Distinct Modes in Plasmonic Waveguides **85**
7.1 Introduction 85
7.2 Concept and Structure Design 86
7.3 Optoelectronic Characterization 89
7.4 Conclusion and Outlook 93

8 Conclusion and Outlook **95**

Bibliography **99**

Acknowledgments **117**

1 | Introduction

The interaction between light and matter is of central importance for a variety of scientific fields and its comprehension has stimulated cutting-edge research in *e.g.* lasing and microscopy. Focusing of light allows to image microscopic samples, however, this is subject to a fundamental limit first described by Ernst Abbe and Lord Rayleigh [1, 2]. Due to diffraction, the resolution is about half the wavelength of the used light; hence it cannot be focused to arbitrarily small scales - at least not with traditional optical components.

Nano-optical systems are elements able to confine light to dimensions well below this diffraction limit, i.e. on scales of few ten nanometers [3]. Even though dielectric materials also allow to control and guide light [4–8], only nanostructures made from noble metals such as gold and silver can focus light to the nanoscale. The origin of this fascinating ability are collective oscillations of the electron density in the metal - so called plasmons [3].

The advantage of confining light to the nanoscale.

Light - in the context of this thesis - has a wavelength ranging from 500 - 1500 nm. The generation of radiation, however, occurs typically on much smaller scales. Electronic transitions, *e.g.* in molecules or semiconductors, in which electrons are confined to scales below 1 nm are responsible for the emission of light. This large mismatch leads to very inefficient absorption as well as radiation of light by individual nanoscale emitters [3]. Placing such emitters close to the strongly confined and enhanced optical near-fields of a nano-optical system significantly improves the coupling between light and emitter, leading to more efficient radiation and new physical effects [9–11].

In addition, interest in technical applications has emerged based on the nanoscale footprint of these systems. Information processing in computers relies on electrical signals within transistors with dimensions of few ten nanometers. Global long range data transfer, however, is mainly facilitated by optical fibers sending near-infrared light over large distances [12]. Thus, data management requires conversion of photons to electrons, but due to the large size mismatch between those two technologies - displayed in figure 1.1 a and b - this is accompanied by high power consumption and constitutes a bottleneck for large data

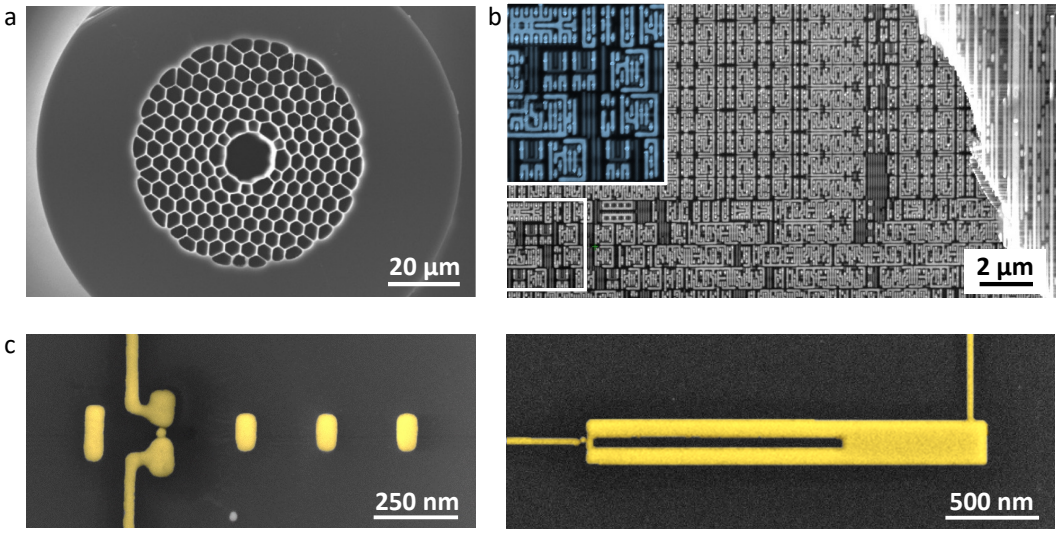

Figure 1.1: Size comparison between traditional elements of optical and electronic data transfer as well as different nano-optical systems. (a) Cross-section SEM image of a hollow-core photonic crystal fiber for data transmission with a diameter of 150 µm. The small cores have a diameter of 4 µm. (b) SEM image of an Intel i3 4160 CPU. The bottom layer including transistors and their interconnections is shown from the top. Residuals of several top layers are visible on the right. The inset shows a zoom into the white rectangle. (c) SEM images of electrically connected nano-optical systems presented in this work: an optical Yagi-Uda antenna (left) and a plasmonic waveguide (right). (a) is taken from reference [19]. (b) Copyright (2020) Piotr Krzeminski, Center for Micro and Nanotechnology UR. The left image in (c) is adapted from reference [20]. The right image in (c) is reprinted with permission from reference [21]. Copyright (2021) American Chemical Society.

centers [13]. Miniaturizing the concept of optical communication can bypass this challenge and no other systems can confine light to smaller scales than metallic nanostructures. Consequently, plasmonic nanocircuitry has the potential to combine the high bandwidth of light with the integration density of modern-day microelectronics [14–18].

The transmission of light at the nanoscale.

Plasmonic two-wire transmission lines confine and guide light via propagating surface plasmons and hence are the nanoscale analog to optical fibers. They have been employed in a variety of experiments to demonstrate complex nanocircuitry such as sorting and routing photons based on their polarization [22–24]. Moreover, coupling to single emitters has been presented [25] and a single-photon transistor was proposed in this context [26]. Yet, optical signals in plasmonic waveguides exhibit strong damping making wireless light transmis-

sion more suitable for larger distances [27].

In the macroscopic world, antennas are used to wirelessly transmit and receive radio frequency signals in mobile devices, radio and television. They translate electrical signals in metals into electromagnetic radiation. As antenna characteristics such as frequency and emission pattern depend on their dimension as well as geometry, macroscopic antennas are limited to radio frequencies [28]. The idea to shrink this concept and develop optical antennas, nanoscale metal structures that emit and receive visible light, already emerged over 60 years ago in Richard Feynman´s famous talk "There is plenty of room at the bottom" [29]. Decades later, first antennas for light were finally demonstrated [30, 31]. As they efficiently translate localized energy to far-field radiation and exhibit strong field enhancement, optical antennas have been coupled to individual emitters in order to develop ultrasmall single-photon sources as well as single molecule sensors [32–37]. Furthermore, more complex antenna geometries, *e.g.* the Yagi-Uda design, were employed to shape the radiation pattern and obtain directional emission; a prerequisite for wireless on-chip communication [38–40]. Yet, these early demonstrations of both plasmonic waveguides and optical antennas were limited to isolated structures and purely optical excitations by external light sources. Complete chip-integration of nano-optical devices, however, demands local and electrical light generation, which faces two major challenges: First, the generation of light at the nanoscale requires new excitation principles as conventional frequency generators do not support optical frequencies [41]. Second, the necessary connection wires have significant dimensions at the nanoscale and care must be taken to not disturb the device performance. Researchers from my current group overcame these challenges and designed the first electrically driven optical nanoantenna [42, 43], in which light emission is based on inelastic electron tunneling. This mechanism only requires a tunnel junction and the absence of any active material results in a large bandwidth [44, 45]. Sparked by this effort, different electrically driven light sources based on optical antennas have been presented [46–51].

The unique contribution of my thesis.

This work builds on recent progress in the community and further advances the development of electrically connected nano-optical systems. The electrical connection not only offers a way to excite the structures, but also facilitates the device assembly at the nanoscale, which is a particular focus of this thesis. In total, I present three unique contributions: (i) A toolbox for the selective surface modification of nanostructures by self-assembled monolayers is introduced. By simply applying a voltage, molecules are removed from distinct nanoscale electrodes, resulting in site-selective functionalization. This offers an additional degree of freedom to the development of functional nanodevices that

was so far limited to specific plasmonic geometries [52]. (ii) Previously, tunnel junctions for inelastic electron tunneling were either fabricated via electromigration [49] or by pushing a coated gold nanoparticle into a prefabricated gap using an atomic force microscope [43]. But none of these approaches yields the desired reproducibility. Here, I present a reproducible and scalable technique to fabricate tunnel junctions in different nano-optical systems based on dielectrophoresis [20]. A feedback systems based on real-time scattering spectra is introduced to further increase the success rate of this process. (iii) Advanced focused ion beam milling of single-crystalline gold platelets [53, 54] is used to fabricate specialized structures that allow to control the direction and polarization of light emission at the nanoscale. Figure 1.1 c shows the two electrically driven nano-optical systems presented in this thesis: an optical Yagi-Uda antenna and a plasmonic waveguide [20, 21]. While the former efficiently radiates light in a specific direction with unprecedented directionality, the latter enables the switching between two propagating plasmonic modes with orthogonal near-field symmetry. Both devices constitute important steps towards the development of integrated optical nanocircuitry and, in combination with the presented fabrication techniques, are going to stimulate future optoelectronic experiments.

The thesis is outlined as follows:

Chapter 2 covers the fundamentals of nano-optical systems. First, I explain the emergence of surface plasmons, followed by introducing basic elements of antenna theory and discussing design principles for optical antennas. An emphasis is given to the electrical excitation of such nanoantennas and the questions "where to connect" and "how to generate light" are answered. Later, the Yagi-Uda design is explained in order to design directional antennas. Finally, I present the theory behind plasmonic two-wire transmission lines, focusing again on the electrical excitation of propagating plasmons. Hence, this chapter quickly covers the most important aspects for engineering different electrically connected nano-optical systems. Chapter 3 gives a short introduction into the surface modification of gold with self-assembled monolayers. I specifically describe the influence of surface-bound molecules on the metal work function and outline how these molecules can be desorbed electrochemically. Since the employed fabrication scheme is key for the device performance, an overview of all experimental details including sample preparation and characterization is given in chapter 4. Key fabrication aspects include advanced focused ion beam milling as well as dielectrophoresis.

The next three chapters cover the experimental results of my thesis. Starting with chapter 5, a technique for site-selective functionalization of micro- and nanoscale electrodes with thiolated molecules is demonstrated experimentally. The potential of this technique for metal-organic nanodevices is discussed and I

describe a possible experiment for antenna controlled molecular machinery. In chapter 6, the first electrically driven in-plane Yagi-Uda antenna for directional light emission is presented. The fabrication of tunnel junctions via feedback-controlled dielectrophoresis is a particular focus and future steps towards optical nanoantenna communication are proposed. Chapter 7 investigates electrically driven plasmonic waveguides that enable to switch between two propagating plasmonic modes, and thus offer switchable polarization states at very small dimensions. Finally, a conclusion and outlook are given in chapter 8. I discuss current limitations of electrically connected nano-optical systems and outline multiple possible improvements for fundamental but also applied research.

2 | Theory of Metallic Nano-Optical Systems

This chapter is devoted to the theoretical foundation of nano-optical systems. First, the origin of their unique abilities is explored. At optical frequencies, metals support characteristic surface charge oscillations - so called plasmons - which are ultimately responsible for the strongly enhanced and spatially confined optical fields in the vicinity of metals [3]. Once this concept is understood, the basic theory behind antennas is covered and differences between radio frequency and optical antennas are discussed. I put a particular emphasis on nanoantennas, in which light generation is driven electrically. This process is described by two different but equivalent pictures: inelastic electron tunneling and quantum shot noise. Furthermore, the electrical wiring - a critical aspect for all nano-optical systems - is examined. To conclude the antenna section, the Yagi-Uda design is introduced. This geometry was first proposed in 1926 and has been used for decades to obtain directional emission and reception of radio frequency signals [55]. In this context, it is described how to model and design optical Yagi-Uda antennas.

Next, the focus shifts to another type of nano-optical system: plasmonic waveguides. The concept of optical two-wire transmission lines is presented and the electrically driven plasmon excitation is discussed. In particular, the modeling of fabricated devices is introduced.

In conclusion, the comprehension of this chapter provides the reader with all the information necessary to understand and design electrically connected optical antennas as well as plasmonic waveguides.

2.1 Gold at Optical Frequencies - Rise of the Surface Plasmon

The theory presented in this section is extensively described in reference [3]. Here, I review the most important aspects for the understanding of nano-optical systems.

The interaction of metals with light is dominated by weakly bound electrons moving almost freely through the crystal. An external electric field causes displacement of these free electrons which results in a polarization in the bulk metal. The exact response is described by the metal's frequency dependent complex dielectric function of the form $\varepsilon(\omega) = \varepsilon^{'}(\omega) + i\varepsilon^{''}(\omega)$. Here, $\varepsilon^{'}(\omega)$ is the real part, while $\varepsilon^{''}(\omega)$ is the imaginary part that includes losses inside the metal. Based on the Drude-Sommerfeld theory for free electrons, the dielectric function reads as

$$\varepsilon_{Drude}(\omega) = 1 - \frac{\omega_p^2}{\omega^2 + \Gamma^2} + i\frac{\Gamma\omega_p^2}{\omega(\omega^2 + \Gamma^2)}, \tag{2.1}$$

with the damping term Γ (electron scattering) and the plasma frequency $\omega_p = \sqrt{ne^2/(m_e\varepsilon_0)}$. For most metals, this material-specific frequency - with the electron density n, the electron charge e, the effective electron mass m_e and the vacuum permittivity ε_0 - lies in the ultraviolet regime. Above ω_p metals become transparent as electrons can no longer follow the oscillation of the incident electric field. At optical frequencies (below ω_p), the real part of the dielectric function becomes negative and the electrons oscillate with a delay to the excitation. Consequently, metals do not act as perfect conductors and the electromagnetic fields penetrate the material to some extent. This is in contrast to the behaviour at even lower frequencies, *e.g.* radio frequencies, where electrons respond with almost no phase lag and screen the excitation. The collective oscillation of the electron density is called surface plasmon and is characteristic for metals at optical frequencies. They give rise to strong optical near-fields confined below the diffraction limit in the vicinity of the metal.

However, the negative real part in equation 2.1 is accompanied by a large (positive) imaginary part leading to strong damping of the electron motion. It is thus advantageous for plasmonic experiments to choose a metal with relatively low imaginary part, such as silver. Yet, gold is used throughout the entire thesis as it exhibits much better chemical stability. Note, that in the case of gold, the Drude-Sommerfeld theory needs to be extended by interband transitions of bound electrons to account for the large absorption at wavelengths shorter than 550 nm. Including this effect, the dielectric function of gold can be accurately modeled as shown in reference [3].

Of special interest are surface plasmon polaritons (SPP) - surface modes propagating at the interface between a metal and a dielectric material, which are homogeneous solutions of Maxwell's equations. By solving the wave equation at

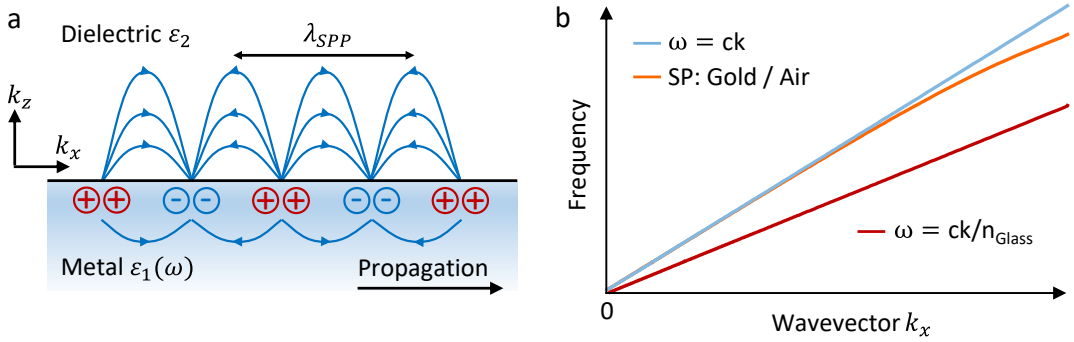

Figure 2.1: The emergence of plasmons. (a) Electric field lines and charge distribution of a surface plasmon polariton at a metal-dielectric interface. The propagation direction and the plasmon wavelength λ_{SPP} are denoted. (b) Dispersion relation of light in air and glass as well as the surface plasmon dispersion relation at a gold-air interface. The excitation of an interface plasmon requires the incident light to have an increased wavevector compared to its free-space value. Inspired by reference [3].

a plane interface, one obtains the dispersion relation in direction of propagation

$$k_x = \sqrt{\frac{\varepsilon_1 \varepsilon_2}{\varepsilon_1 + \varepsilon_2}} \frac{\omega}{c} \tag{2.2}$$

as well as perpendicular to the surface (into the dielectric and into the metal)

$$k_{j,z} = \sqrt{\frac{\varepsilon_j^2}{\varepsilon_1 + \varepsilon_2}} \frac{\omega^2}{c^2}. \tag{2.3}$$

Here, ε_1 and ε_2 are the dielectric functions of metal and dielectric, respectively, and c is the speed of light in vacuum. The imaginary part of ε_1 is neglected for now, because the absolute value of the real part is much larger. As SPPs are localized to the interface, per definition, the electromagnetic fields must decay exponentially with increasing distance to the surface and hence a purely imaginary $k_{j,z}$ is required. At the same time, k_x must be real in order to obtain a propagating mode. These two conditions are fulfilled if $\varepsilon_1 \cdot \varepsilon_2 < 0$ and $\varepsilon_1 + \varepsilon_2 < 0$ and consequently, one of the dielectric functions must have a large negative value. This further underscores the unique potential offered by metals at optical frequencies.

Figure 2.1 a illustrates the electric field lines as well as charge distribution of a SPP. Note, that the electric field penetrates the dielectric more than the metal, which can be obtained from equation 2.3 by including the imaginary part of ε_1. Furthermore, the dispersion relation from equation 2.2 is displayed in figure 2.1 b. The wavevector component of the SPP is always larger than that of a photon in air. The corresponding dispersion curves approach each other, but never

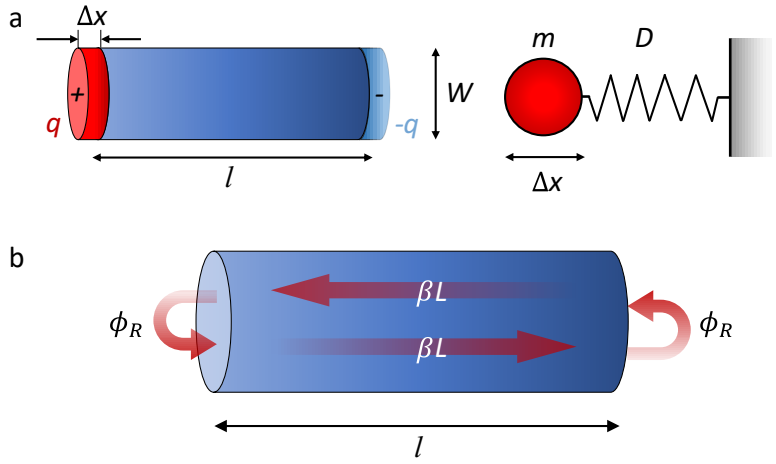

Figure 2.2: Modeling of surface plasmons in elongated particles. (a) Electrons in an elongated particle with length l and diameter W are displaced by Δx (left). As a consequence, charges q and $-q$ build up at both ends of the particle. The resulting oscillation of electrons can be treated as a harmonic oscillator with an electron mass m connected to a spring with spring constant D (right). (b) Fabry-Pérot model for a wire with finite length l. As the mode propagates along the wire, a phase of βl (with the mode constant β) is accumulated. At the wire ends, an additional phase shift Φ_R is added and consequently the mode experiences a larger effective length. Inspired by reference [3].

cross. Therefore, the plasmon wavelength $\lambda_{SPP} = 2\pi/k_x'$ (with k_x' being the real part) is always shorter than the corresponding free-space wavelength. In order to excite SPPs, energy and momentum must be conserved, *i.e.* the wavevector of the incident photon has to match or even exceed that of the surface mode. This can be achieved, for example, by guiding the light through a medium with refractive index larger than one (cf. figure 2.1 b). Confining light to the surface of metallic nanostructures offers another excitation possibility, because the strong optical near-fields contain wavevector components parallel to the interface that match k_x of SPPs.

In order to describe the plasmonic response of elongated particles, such as the structures used in this thesis, two models are introduced and illustrated in figure 2.2. In a simple picture, plasmons can be depicted as harmonic oscillations which are carried out by a mass (electrons) connected to a spring (see figure 2.2 a). Displacing the electron cloud in a metal rod by Δx leads to charges of opposite signs at the ends. This creates an electric field across the particle which gives rise to a restoring force $F = -D\Delta x$, where D is the spring constant. The resonance frequency of the system is

$$\omega_{res} = \sqrt{\frac{D}{m}} = \frac{\omega_p}{2\sqrt{2}} \frac{1}{R}. \tag{2.4}$$

It is important to note, that the resonance frequency is inversely proportional to the aspect ratio R (ratio of length to diameter). This simple relation is shaping the design of nanostructures such as optical antennas.

To further visualize propagating plasmons, the Fabry-Pérot model is applied (see figure 2.2 b). A finite metal wire supports a fundamental guided mode, which travels along the particle and is reflected at its ends. If the mode accumulates a phase of 2π per round trip, a standing wave will form in this cavity. In case of perfect reflection at the wire ends, the resonance condition is $\beta l_{res} = n\pi$, with the mode constant $\beta = 2\pi/\lambda$ and the resonance order n. At optical frequencies, however, the fields of the mode penetrate the wire ends and extent to the outside of the particle before reflection. This leads to an additional phase shift Φ_R and one obtains

$$\beta l_{res} + \Phi_R = n\pi. \tag{2.5}$$

This means that the plasmonic mode propagating along a wire experiences an even larger effective length of the wire [9], and as a result, an important scaling rule for optical nanostructures must be introduced (see subsection 2.2.1). Note, the mass-spring and the Fabry-Pérot model both predict an inverse relationship between the length of the particle and its resonance frequency.

After investigating the rise of surface plasmons, the next sections introduce concepts and design principles for nano-optical systems - starting with nanoantennas.

2.2 Optical Nanoantennas

Classical antennas link electrical signals to propagating radio waves. They can transmit and receive electromagnetic radiation and their bandwidth depends on the antenna dimensions. Optical antennas are therefore nanostructures, which convert light to localized energy and efficiently emit light from a nanoscale source [3]. The latter especially differentiates optical antennas from other nano-optical elements that only aim at storing electromagnetic radiation as long as possible [10, 11]. Even though dielectric nanostructures have been proposed [5–8], I focus on purely metallic devices with clearly defined optical resonances [14, 30, 42]. In this section, I first introduce general concepts of antenna theory and then transfer these principles to the optical regime. Challenges arising from the electrical driving at the nanoscale are discussed in more detail. Additionally, the theory behind directional Yagi-Uda antennas is covered. Besides giving a general theoretical overview, the goal of this section is to point out critical aspects that optical antenna engineers should consider.

2.2.1 From Classical to Optical Antennas

In LC circuits the energy oscillates between the electric field of a capacitor and the magnetic field of an inductor. The resonance frequency of an undamped system is

$$\omega_0 = \frac{1}{\sqrt{LC}}, \tag{2.6}$$

with the inductance L and the capacitance C. In a closed configuration, the fields are mainly confined within the circuit. But by opening it to a straight and conductive wire, one obtains the most simple antenna geometry - a dipole. Upon applying an AC voltage, this system generates time-varying electric and magnetic fields, which are radiated perpendicular to the dipole axis. In the far-field, the electromagnetic fields are decoupled from the power supply of the dipole and propagate freely through space. For this reason, antennas are modeled as open LC circuits. As shown in equation 2.6 their resonance frequency depends on L and C, which scale with the size of the antenna. Consequently, smaller antennas, and hence smaller L and C, lead to shorter wavelengths and higher frequencies [56].

Classical antennas are metallic, macroscopic (several centimeters to meters) devices operating at radio frequencies. They are usually connected to a voltage source by a two-wire transmission line as depicted in figure 2.3. After excitation, current standing waves with sinusoidal shape build up on the entire device. In case the transmission line is only terminated by an open end, *i.e.* the structure simply consists of two parallel wires, no radiation is expected (see figure 2.3 a). Instead, the current elements on both wires oscillate out of phase and the electric fields are localized between the wires, comparable to a plate capacitor. An antenna with length l can be added by bending both wires at a distance of $l/2$ from the ends (see figure 2.3 b). The current distribution in this antenna is

$$I(z) = I_{Max} sin\left[k\left(\frac{1}{2}l - |z|\right)\right]. \tag{2.7}$$

Here, I_{Max} is the maximum current amplitude and $k = 2\pi/\lambda$ is the wavevector with the free-space wavelength λ. At a bending angle of 90 ° the current elements in both antenna wires add up constructively and the antenna radiates into the far-field with maximum intensity [3, 9].

An important characteristic in antenna theory is the impedance. It describes how well power is transferred between individual elements, *e.g.* from the source to the antenna via the transmission line. The circuit of this configuration is shown in figure 2.3 c. It includes the voltage source with internal impedance Z_{in} and the two-wire transmission line with its characteristic impedance $Z_0 = U(z)/I(z)$. The antenna impedance is defined by voltage and current at

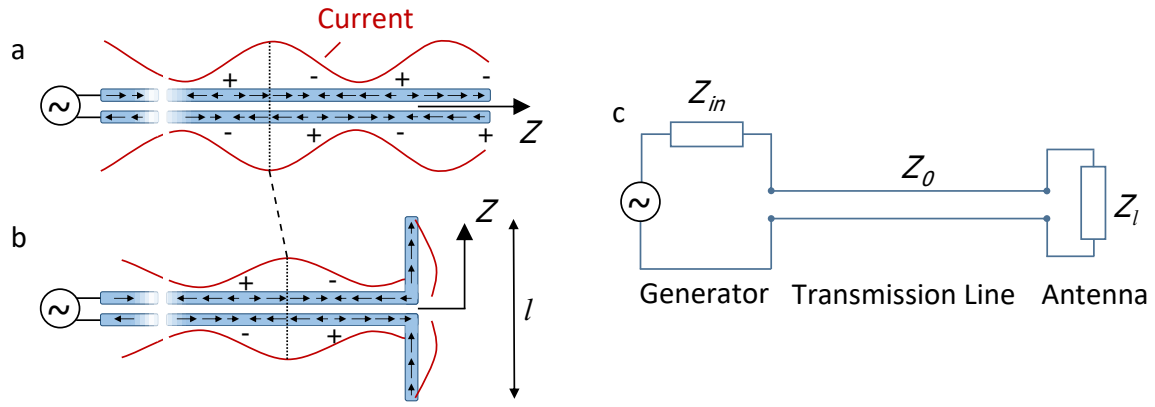

Figure 2.3: Classical antennas. An AC voltage generator drives a two-wire transmission line, which is either terminated by (a) an open end or (b) an antenna with length l. The standing current waves, the current directions as well as magnitudes (arrows) and the charge accumulations (plus and minus) are denoted. Due to destructive interference, the circuit in (a) is not radiating into the far-field. Efficient radiation is achieved by introducing an antenna as in (b). Note, that the standing wave in (b) is shifted by reflections at the bending point. (c) Circuit sketch of (b) depicting the generator impedance Z_{in}, the characteristic impedance of the two-wire transmission line Z_0 and the antenna impedance Z_l. Inspired by reference [3].

the input terminals and reads as

$$Z_l = U(0)/I(0) = R_l + iX_l. \tag{2.8}$$

An impedance mismatch between the individual elements causes reflections and minimizes the power transfer; especially at the bending points in figure 2.3 b. This is summarized by the reflection coefficient

$$\Gamma = \frac{Z_l - Z_0}{Z_l + Z_0}. \tag{2.9}$$

Interestingly, this mismatch also depends on the antenna geometry. The current at the input terminals vanishes for antennas with length $l = \lambda$ (see equation 2.7), and thus the impedance as well as Γ become very large. In order to avoid reflections in classical antennas, Z_l and Z_0 are matched by using external circuits. For nanoantennas, such impedance matching circuits are difficult to accomplish. In this case, antennas with $l = \lambda/2$ are preferred as they exhibit relatively low Z_l.

Moreover, the antenna impedance Z_l (see equation 2.8) describes, how well power is radiated away. At the antenna resonance, the imaginary part X_l can be neglected and all losses are included in the real part $R_l = R_{rad} + R_{nr}$. While

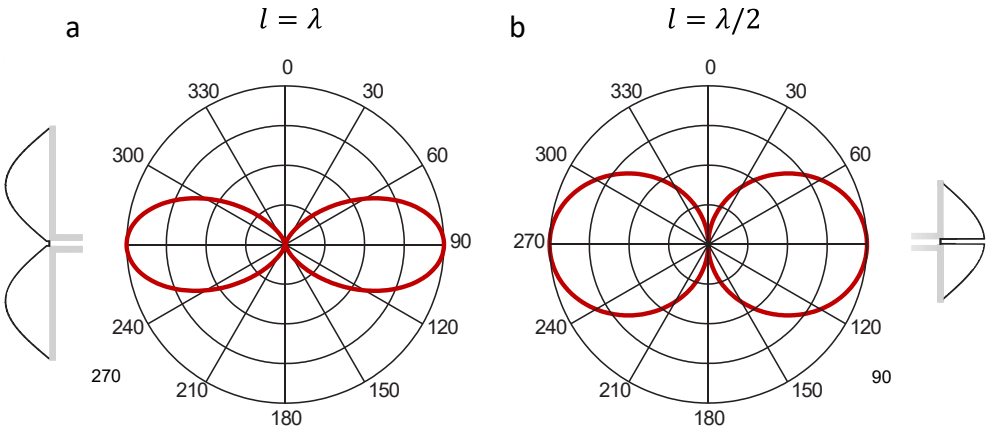

Figure 2.4: Antenna radiation pattern. Emission characteristics of antennas with (a) $l = \lambda$ and (b) $l = \lambda/2$ calculated according to equation 2.12. The current standing waves are sketched next to the patterns showing that the current amplitude close the feed gap is different for both antenna geometries. Adapted from reference [9].

R_{nr} covers non-radiative Ohmic losses, R_{rad} is the radiation resistance:

$$R_{rad} = \frac{2\pi}{3} Z_w (\frac{l}{\lambda})^2. \tag{2.10}$$

Here, $Z_w = 377\,\Omega$ is the free-space wave impedance. A high R_{rad} leads to more emission and consequently, an antenna with $l = \lambda$ radiates better than one with $l = \lambda/2$. The overall radiation efficiency of the antenna is defined as

$$\eta = \frac{R_{rad}}{R_{rad} + R_{nr}}. \tag{2.11}$$

At radio frequencies, metals are perfect conductors and Ohmic losses are small. Therefore, η is almost 1 [3, 9, 28, 57].

The emission behaviour of classical antennas is completely dominated by their geometry and the exact emission pattern can be derived from the following formula:

$$p(\theta, \phi) \sim \left| \frac{cos(\frac{1}{2} klcos(\theta) - cos(\frac{1}{2} kl)}{sin(\theta)} \right|^2. \tag{2.12}$$

θ is the angle between emission and antenna axis and ϕ is the azimuthal angle. Figure 2.4 shows calculated emission patterns of antennas with $l = \lambda$ and $l = \lambda/2$. The sketched current waves are in accordance with equation 2.7. Even though the current distributions are different, both geometries act as dipoles and radiate predominantly in the direction perpendicular to the antenna axis. As the antenna principle is reciprocal, the emission pattern is equal to the receiving

pattern.

These concepts can be transferred to any frequency regime as the operating wavelength is linked to the dimensions of the antenna (see equation 2.6). In order to design resonant devices for light, the structure size must be decreased down to the nanoscale. However, two new aspects have to be considered at optical frequencies. First, the dimensions of the electrical wiring become significant as the antenna is reduced to such small scales. For simplicity, I am now only examining isolated optical antennas without any electrical connection. This, together with the actual driving mechanism will be covered in the next subsection. Second, metals are no longer treated as perfect conductors at optical frequencies. The electromagnetic fields fully penetrate a metal wire causing volume currents in the antenna; as opposed to surface currents at radio frequencies. Furthermore, metallic nanostructures exhibit plasmonic resonances that scale inversely with particle length (see equation 2.4). The Fabry-Pérot model introduced previously shows that a plasmonic mode propagating through a metal wire feels a larger effective particle length (remember equation 2.5). This results in a modified scaling rule for antennas at optical frequencies [58]:

$$\lambda_{eff} = n_1 + n_2 \frac{\lambda}{\lambda_p}. \tag{2.13}$$

Here, $n_{1,2}$ are geometrical coefficients with dimensions of length, λ_p is the plasma wavelength and λ_{eff} is significantly smaller than λ. A quick example illustrates the effect of this new design principle: in order to fabricate a half-wave antenna operating at $\lambda = 880\,\text{nm}$, the length is $l = \lambda_{eff}/2 = 160\,\text{nm}$ instead of $l = \lambda/2 = 440\,\text{nm}$. The exact ratio λ/λ_{eff} depends on geometrical factors and is usually around 2 - 5 [3]. Simulations with the boundary element method (BEM) and the finite-difference time-domain method (FDTD) can accurately predict the resonance frequency of nanoscale metal particles and therefore aid in the development of optical antennas [9, 59–61]. The above mentioned scaling rule leads to an even smaller radiation resistance (see equation 2.10). In addition, metals exhibit higher Ohmic losses at optical frequencies leading to less efficient antennas (cf. equation 2.11). Fortunately, the presence of plasmons can counteract some of these drawbacks.

Coupling two half-wave antennas end-to-end results in the central building block for all optical antennas presented in this thesis. In terms of the mass-spring picture, this system can be modeled by introducing an additional spring between the two particles. Figure 2.5 a depicts the energy diagram and simulated near-field intensity spectra of this coupled antenna (also called two-arm antenna) as well as an individual wire. Upon coupling, two modes arise. The higher-energy antibonding mode is characterized by out-of-phase oscillations of the charge densities in the two antenna arms. It is not radiating efficiently as the dipole moments cancel each other in the far-field. The lower-energy bonding

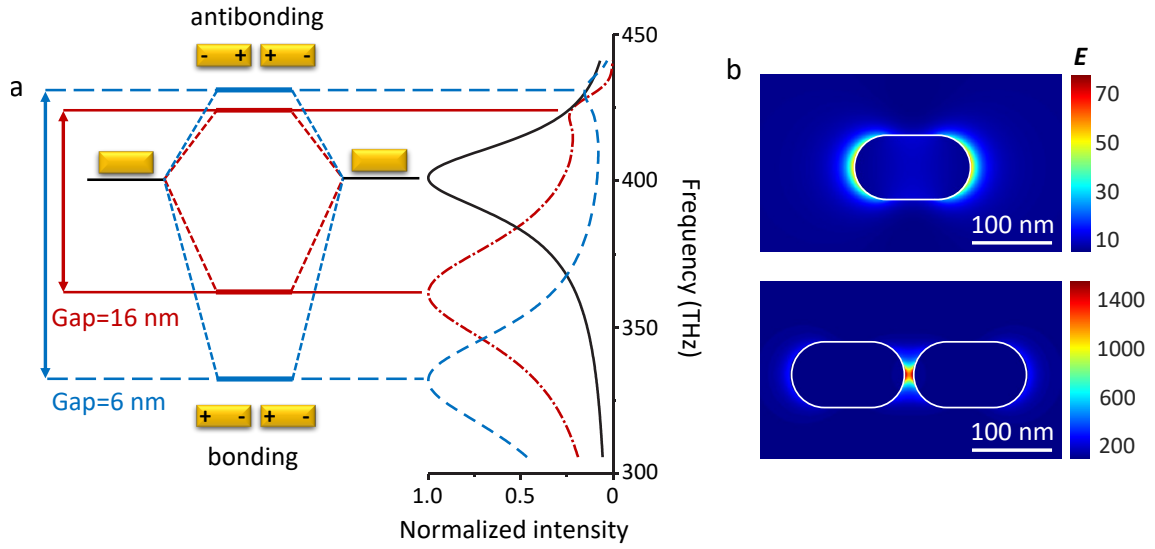

Figure 2.5: Coupling of optical antennas. (a) Energy levels and simulated near-field intensity spectra for the two antenna geometries. Black stands for single particles, while red and blue represent coupled structures with a gap of 16 nm and 6 nm, respectively. The coupling leads to two eigenmodes: bonding and antibonding. The former has a dipolar character (see charge distribution) and radiates. The latter is considered "dark", because the dipole moments cancel out in the far-field. Reducing the gap size leads to a larger spectral spacing of the two modes and the bonding mode shifts to lower frequencies. Individual particles are 30 nm high, 50 nm wide and 110 nm long. (b) Normalized electric fields for single-arm and two-arm antennas (bonding mode) simulated with the boundary element method (see subsection 2.2.3). The two-arm antenna exhibits very high fields in the feed gap due to the coupling of the two particles. (a) is reprinted and adapted with permission from reference [59]. Copyright (2010) American Chemical Society.

mode exhibits in-phase oscillations and thus has a dipolar character. By reducing the gap size, the energy splitting between the two modes increases and the resonance of the bonding mode shifts to smaller frequencies [3, 9].

Besides radiating into the far-field, the bonding mode offers highly confined and enhanced electric fields in the feed gap, exceeding those of a single particle, as illustrated in figure 2.5 b. This effect offers the potential to significantly enhance light-matter interaction. The generation as well as the absorption of light by individual nanoscale emitters is an inherently inefficient process. Coupling of photons to electronic transitions in matter is limited by the size mismatch between photon wavelength (several hundred nanometers) and electron confinement (less than one nanometer). Placing a single emitter into to the feed gap of an optical two-arm antenna bypasses this challenge. This is explained in terms of the partial local density of states $\rho_p(r, \omega)$ (LDOS), which describes the

amount of optical modes per unit volume and frequency at position r. In a simple picture, confining electric fields between the two arms increases the LDOS and intensifies the optical density experienced by a single emitter; hence increasing its absorption. In addition, by providing more optical states, the coupling between an excited emitter and one of these states becomes more likely and photons are generated more efficiently. The decay rate γ of an emitter scales linearly with $\rho_p(r,\omega)$ and one obtains [3]

$$\gamma = \frac{\pi\omega}{3\hbar\varepsilon_0} |p|^2 \rho_p(r,\omega), \tag{2.14}$$

where p is the transition dipole matrix element and $\hbar$ is the reduced Planck constant. Next, the power P_D radiated by a dipole can be linked to the LDOS by the simple relation [62]

$$\frac{P_D}{P_0} = \frac{\rho_p(r,\omega)}{\rho_0}. \tag{2.15}$$

Here, P_0 and ρ_0 are the dissipated power and the LDOS in vacuum, respectively. Smaller gaps lead to even higher LDOS, and thus faster decay as well as more radiated power. Note, the emitter should not be placed too close to the metal surface as this opens up additional channels for non-radiative energy transfer, which results in quenching [63]. The LDOS enhancement also plays a key role in the excitation of radiating and propagating modes. In case of the two-arm antenna, an emitter in the feed gap predominantly excites the bonding mode and light is radiated away with a polarization parallel to the antenna (corresponding to the charge oscillations in figure 2.5 a). The excitation of propagating plasmonic modes is discussed in subsection 2.3.2 and chapter 7.

To conclude this subsection, the main differences between classical and optical antennas are listed: (i) metals are not perfectly conducting at optical frequencies; hence, Ohmic losses are larger and electromagnetic fields penetrate the metal. (ii) The scaling rule has to be adjusted for optical antennas. (iii) The presence of plasmons offers to modify light-matter interaction. (iv) Electrical wiring and driving represent new challenges at the nanoscale. This aspect is covered in the following.

2.2.2 Electrically Driven Optical Antennas

Optical antennas have a length of 100 - 300 nm and a width of 60 - 80 nm. By using high-precision focused ion beam (FIB) milling, electrical connection wires with a minimum thickness of 30 - 40 nm can be fabricated. Such relatively large and polarizable objects influence the plasmonic resonances of nearby nanoantennas and open up new pathways for reflections. Hence, the impedance mismatch (see subsection 2.2.1) between a nanoantenna and its electrical wiring is a particular challenge. It has been proposed to drive optical antennas with

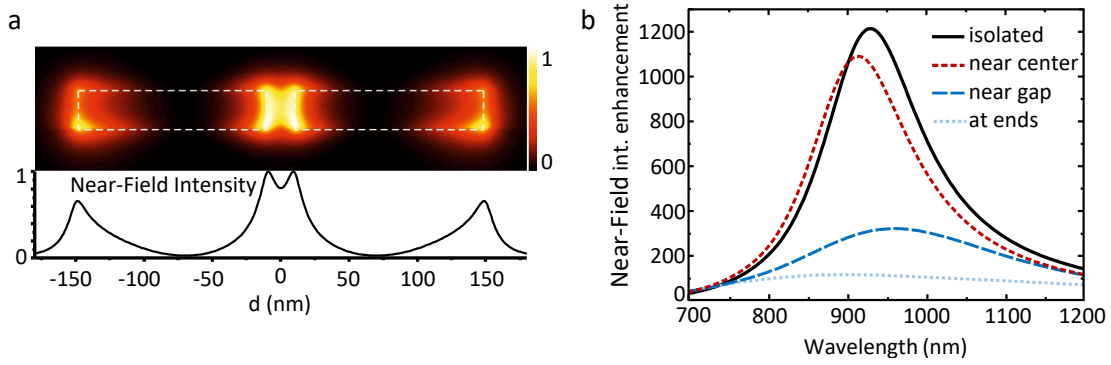

Figure 2.6: Finding the perfect connector position. (a) Normalized near-field intensity map (top) and integrated intensity (bottom) of a coupled two-arm antenna (bonding mode). Positions of low electric fields (large currents) are located around the center of the arms, slightly displaced towards the gap. (b) FDTD simulations of near-field intensity enhancement in the feed gap for different connector positions: close to the gap (blue, long-dashed, 10-fold increased), at the ends of the antenna arms (light blue, dotted, 10-fold increased) and close to the center of the antenna arms (red, short-dashed). For comparison, results for an isolated (unconnected) antenna are shown in solid black. Connectors attached near the center of the antenna arms (low electric fields) only have a minimal influence on the near-field intensity enhancement. Reprinted and adapted with permission from reference [42]. Copyright (2012) American Chemical Society.

well-matched two-wire transmission lines [64]. Yet, experimental realizations are still challenging and the exact location at which the antenna is connected by an electrical wire is of key importance.

Here, I focus on optical half-wave antennas. As discussed in the previous subsection, this geometry offers a small impedance mismatch. The simulated near-field intensity of an isolated two-arm antenna (bonding mode) is depicted in figure 2.6 a. The highest optical fields are located in the feed gap followed by the ends of the two arms, while field minima are situated near the center of the particles, slightly shifted towards the gap. In order to apply a voltage between the two antenna arms, both particles have to be connected to an external source. Figure 2.6 b demonstrates how the plasmonic resonance of this structure is influenced by attaching metal wires at different locations. Placing the connectors at positions of high field intensity (low current) leads to the excitation of plasmons, transporting energy away from the antenna, and consequently disturbs the resonance. In the context of antenna theory, this is equivalent to a large impedance mismatch. Instead, both arms have to be connected at positions of minimum field intensity (high current), *i.e.* near their centers. This results only in a small deviation from the near-field enhancement of an unconnected (isolated) antenna [42].

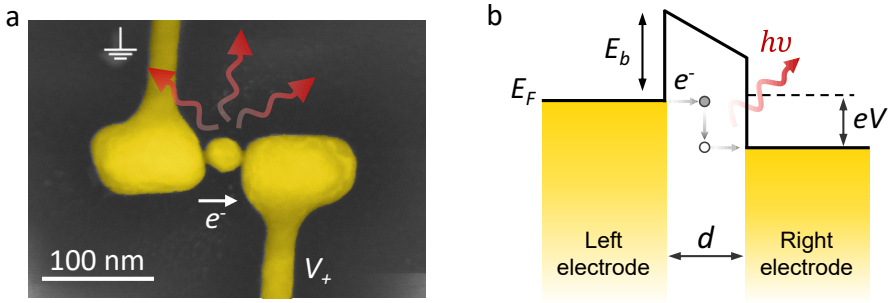

Figure 2.7: Light generation with nanoantennas. (a) Colored SEM image of an electrically connected optical antenna exhibiting tunnel junctions at the interfaces between antenna arms and gold nanoparticle. Upon applying a voltage, electrons tunnel across the junctions and light is generated. (b) Schematic of inelastic electron tunneling. An electron scatters inelastically at the tunnel barrier and a photon with energy eV is emitted.

Next, I present the light generation mechanism. Classical antennas are fed by voltage generators, which are based on high-speed transistors. However, they are not able to produce frequencies higher than 300 GHz [41]. Light, on the other hand, has a frequency above 300 THz, and is usually generated in light emitting diodes (LEDs) with dimensions much larger than optical antennas. In order to emit light at the nanoscale, several approaches have been investigated, including carbon nanotubes [65–67], inorganic nanowires [68, 69] and plasmonic LEDs [70]. In particular, inelastic electron tunneling (IET) - offering a broad bandwidth and switching times on the order of femtoseconds [71] - has been explored. First observed in planar metal-insulator-metal junctions [44, 45], it was later employed by Kern *et al.* to develop the first electrically driven optical antenna [43]. An exemplary antenna and a sketch of the IET mechanism are depicted in figure 2.7. The device does not require any semiconductor materials, instead, photon emission is based on electron tunneling. FIB milling and dielectrophoresis are used to fabricate the two-arm structure and insert a gold nanoparticle into the feed gap to create ∼1 nm tunnel junctions (see section 4.1). The connection wires are attached to both arms at positions of low fields and upon applying a DC voltage V, electrons tunnel across the gap. This process can be inelastic, *i.e.* an electron loses energy and a photon with energy eV is emitted.
IET is an inherently inefficient process as most electrons tunnel elastically. The internal quantum efficiency is defined as [3]

$$q = \frac{\gamma_{IET}}{\gamma_{IET} + \gamma_{ET}}, \tag{2.16}$$

with the inelastic (radiative) and elastic (non-radiative) tunneling rates γ_{IET}

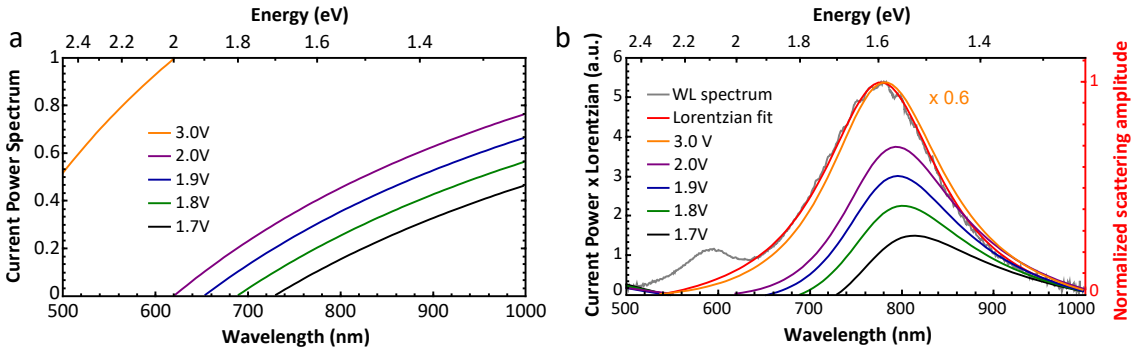

Figure 2.8: Modeling the quantum shot noise of nanoantennas. (a) Current power spectrum for different applied voltages. As the voltage increases, the current power spectrum shifts to higher frequencies. (b) By multiplying the current power spectrum with the Lorentzian fit (red) of an experimental white-light spectrum (grey), one obtains calculated emission spectra for different voltages. Reprinted by permission from Springer Nature: Nature Photonics [43]. Copyright (2015).

and γ_{ET}, respectively. This equation exhibits the same form as the radiation efficiency η (see equation 2.11). A general expression for the inelastic tunneling rate has been derived in references [48, 72] and the quantum efficiency in vacuum was calculated to be on the order of 10^{-8} per spectral segment [62, 73]. Notably, the radiative tunneling rate γ_{IET} is increased by the enhanced LDOS in the tunnel junction of optical antennas and thus, the quantum efficiency is significantly improved (see equations 2.14 and 2.15 in subsection 2.2.1). Structures similar to the one in figure 2.7 a achieve efficiencies of 10^{-4} [43, 74], while even higher LDOS yield 10^{-2} [50]. Recently, it has been shown that efficiencies on the order of 10^{-1} can be achieved by adding resonant states into the tunnel junction [75]. This process is called resonant inelastic electron tunneling and is not a focus of this thesis.

In order to predict electroluminescence (EL) spectra of antennas driven by IET, the quantum shot noise (QSN) model is introduced [43, 76]. IET and QSN are two equivalent pictures describing the same process. The latter interprets the current fluctuations through the tunnel junction as an ensemble of oscillating single-frequency dipoles with spectral density $C(\omega)$ (current power spectrum). The large optical near-fields in the gap increase the power of the dipoles, and thus, more light is radiated into the far-field. These two contributions - near-field and far-field response - are summarized in the emissivity of the antenna $A(\omega)$. The spectrum of emitted photons $I(\omega)$ is given by

$$I(\omega) \propto A(\omega)C(\omega) = A(\omega)\frac{eV}{2\pi R_0}(1-\frac{\hbar\omega}{eV}) \propto A(\omega)(eV-\hbar\omega), \tag{2.17}$$

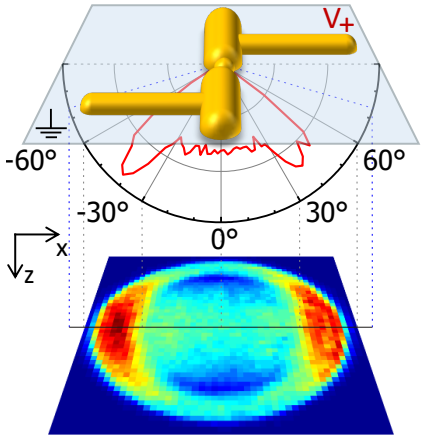

Figure 2.9: Emission pattern of an optical antenna. The sketch illustrates the orientation of the nanoantenna on the glass substrate. Measured emission pattern and corresponding *xz*-projection exhibit a dipolar pattern, but light is radiated into the glass under the critical angle of ∼41 °. Reprinted by permission from Springer Nature: Nature Photonics [43]. Copyright (2015).

with the applied voltage V and the DC junction resistance R_0. Equation 2.17 allows the simple calculation of EL spectra in three steps. First, the current power spectrum $C(\omega)$ is plotted for different applied voltages in figure 2.8 a. The cut-off frequencies become larger for increasing voltages, *i.e.* the energy of a photon cannot be larger than the applied voltage (energy conservation). Next, the emissivity $A(\omega)$ is estimated by measuring the white-light scattering spectrum of an antenna and fitting it with a Lorentzian (see figure 2.8 b). This is reasonable as the scattering spectrum includes the near-field and far-field responses of this system. Finally, EL spectra are calculated according to equation 2.17. As shown in figure 2.8 b, the resulting emission spectra resemble the antenna resonance; a direct consequence of the frequency-dependent $A(\omega)$ (also see the local density of states $\rho_p(r,\omega)$). Furthermore, EL spectra can be tuned to smaller wavelengths by increasing the applied voltage and for sufficiently high voltages, the spectrum even matches the antenna resonance.

The emission pattern of an electrically driven optical antenna is depicted in figure 2.9 [43]. Light is radiated perpendicular to the long axis of the antenna, just as in figure 2.4. However, optical antennas are not free-standing as their radio frequency counterparts, but they typically lie on a glass substrate with higher refractive index than the surrounding air, and hence most photons are emitted into the glass. Such emission patterns can be measured with an oil-immersion objective underneath the substrate and are used to characterize optical Yagi-Uda antennas in chapter 6.

2.2.3 The Yagi-Uda Design

The concept of Yagi-Uda antennas was developed in 1926 and has since been used to achieve highly directional emission in the radio frequency regime [55]. Figure 2.10 a depicts a typical five-element Yagi-Uda antenna consisting of one reflector, one feed element and three equally spaced directors. Only the feed, which exhibits a half-wave design (here as a folded dipole), is connected to a voltage source. The other elements are passive (or parasitic), *i.e.* they are driven by the feed radiation. In order to achieve directional emission, the resonance frequencies of the passive elements are detuned as shown in figure 2.10 b. The reflector is slightly longer than the feed and its resonance is shifted to longer wavelengths, while directors exhibit oscillations at shorter wavelengths. As the feed drives the antenna, phase-shifted oscillating currents are excited in all five elements. If the spacing is chosen correctly - typically in the range of $0.15\,\lambda$ to $0.25\,\lambda$ - the electromagnetic waves emitted by the individual elements interfere constructively in forward and cancel out in backwards direction (see figure 2.10 c) [28]. The directivity of Yagi-Uda antennas can be optimized by comparing the intensities in forward ($|E_{fw}|^2$) and backward ($|E_{bw}|^2$) direction, leading to the definition of the forward-to-backward (FB) ratio [20]:

$$FB[dB] = 10 \times log_{10}\left(\frac{|E_{fw}|^2}{|E_{bw}|^2}\right). \tag{2.18}$$

By considering the modified scaling rule (cf. equation 2.13), the Yagi-Uda concept can be transferred to optical frequencies [38, 40, 77]. In this thesis, the antenna introduced in subsection 2.2.2 is used as the feed element to realize an electrically driven Yagi-Uda antenna for light (see chapter 6). The optimal geometry for maximum directivity is found in an iterative process including experiments - carried out by me - and simulations - carried out by Philipp Grimm. In the following, I will give a short overview of the employed models. For more information see reference [20].

Analytical Model

An analytical model is used to quickly calculate appropriate resonance frequencies and spacing for all antenna elements [20, 77]. Particles are assumed to be much smaller than the wavelength of light, and thus, the electric field is homogeneous over each element (quasi-static approximation). The antenna elements are treated as coupled dipoles and are driven by the feed with fixed frequency ω_0 (see figure 2.11 a). Next, the local electric field is determined as the sum of all emitted fields (of the individual antenna elements), which allows to calculate the far-field emission pattern. The FB ratio is then optimized by adjusting the

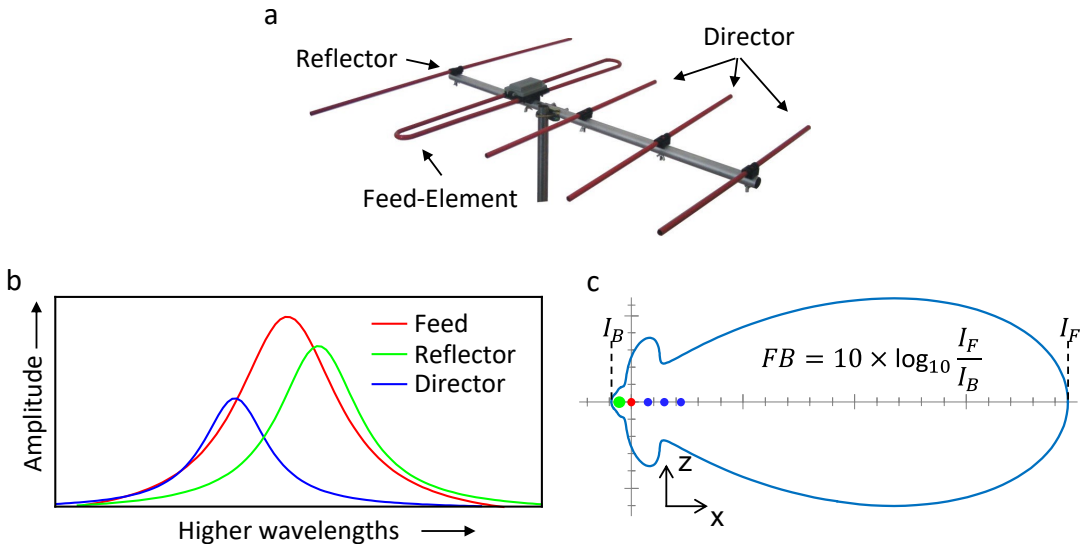

Figure 2.10: Yagi-Uda antenna principle. (a) Five-element Yagi-Uda antenna for radio frequencies with one reflector, one feed element and three directors. The feed element exhibits a half-wave folded dipole geometry. (b) The feed resonance has to be in between the resonance frequencies of director and reflector. (c) Radiation pattern of a five-element Yagi-Uda antenna in the *xz*-plane. The geometry with directors and reflector lead to constructive interference in forward direction and thus directional emission. The equation to calculate the forward-to-backward ratio is denoted. (a) is taken from reference [78]. (b) is adapted from reference [74]. (c) is adapted from reference [20]

element spacing as well as the size dependent detuning of reflector and director (δ_{ref} and δ_{dir}). This model yields a simple estimation of the antenna geometry, however, it is limited by the quasi-static approximation and the homogeneous surrounding. For this reason, numerical tools are used to support the analytical model and better mimic the experiment.

Boundary Element Method (BEM)

BEM is a numerical technique in which the problem is reduced to the surface boundaries of particles to save time and computational power. Here, the open source MNPBEM toolbox is used to solve Maxwell's equations for metallic nanostructures [60, 61]. Optical antennas are modeled as rounded and extruded polygons (see figure 2.11 b) lying on a glass substrate (refractive index n = 1.52). The top half-space is filled with air (n = 1) and data from Olmon *et al.* is used for the dielectric function of gold [79]. Importantly, BEM allows to consider retardation effects beyond the quasi-static approximation, *i.e.* the electric field is no longer assumed to be homogeneous over a particle. By calculating and optimizing the

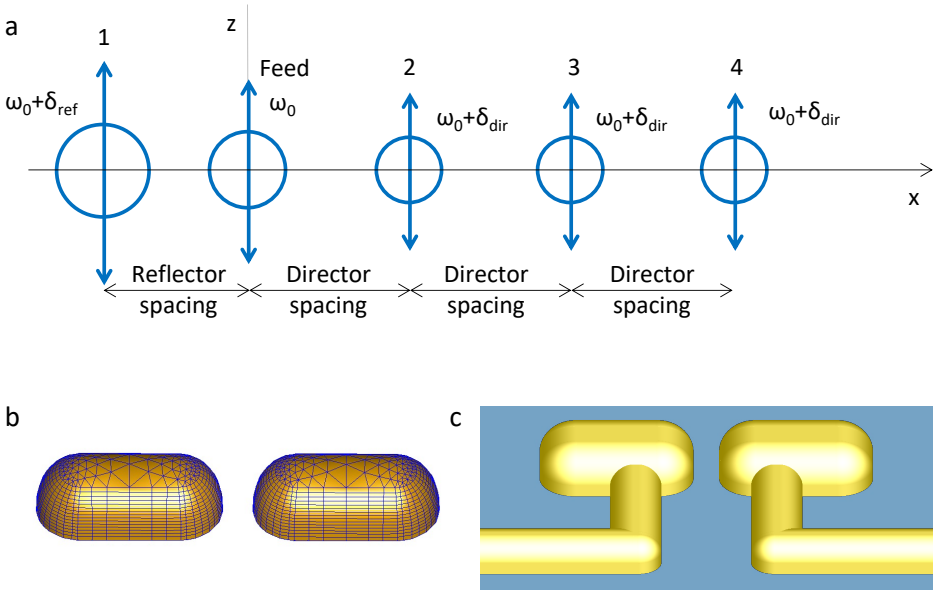

Figure 2.11: Modeling of optical Yagi-Uda antennas. (a) Analytical model describing the antenna elements as coupled dipoles in the quasi-static approximation. The feed resonance ω_0 is set to a fixed value and the reflector as well as director frequencies are detuned by δ_{ref} and δ_{dir}, respectively. (b) BEM representation of an isolated two-arm antenna. (c) Electrically connected two-arm antenna in FDTD. A homogeneous surrounding is adopted for the analytical model, while the antenna structure is lying on a glass substrate in both numerical models. Adapted from reference [20].

FB ratio with BEM, the ideal geometry for optical Yagi-Uda antennas is found. However, this tool can not simulate complex shapes such as the kinked connectors. Only unconnected structures are considered in BEM and the influence of the electrical wiring is studied with another numerical technique.

Finite Difference Time Domain (FDTD)

Unlike BEM, the FDTD method discretizes time and volume of a particle [80]. This computation heavy technique requires a finite simulation region; hence perfectly matched layers consisting of a lossy material are introduced to emulate open boundary conditions [81]. The advantage of FDTD is that connectors can be coupled to theses perfectly matched layers and treated as infinitely long wires without any reflections. For this reason, FDTD is used to study complete antenna structures including the connectors.

Fabrication constraints must be taken into account in order to design optical Yagi-Uda antennas with high directivity. In addition, the significant size of the electrical wiring has to be considered: not only can the antenna resonance

be disturbed (see subsection 2.2.2), the connectors also influence the directivity of the antenna and act as an additional reflector [20]. The final geometry is presented in section 6.2.

2.3 Plasmonic Waveguides

Plasmonic waveguides allow to confine and guide light at the nanoscale. In contrast to optical fibers, which transmit light over large distances with minimal losses, plasmonic structures usually consist of metals offering much larger confinements, yet more damping (see section 2.1). Early work focused on plasmonic nanoparticle arrays [82–86], grooves and channels [87,88] as well as single metal wires [89–94], but soon plasmonic two-wire transmission lines (TWTL) became a popular building block for optical nanocircuitry [64, 95–97]. They support two lowest-order propagating modes, which can be excited separately [22], and allow for advanced light routing at the nanoscale [23, 24]. In this section, I first present the basic properties of optically driven plasmonic TWTLs. Next, devices are electrically connected (just like optical antennas; see subsection 2.2.2) and propagating plasmons are launched by IET. The modeling of the electrical excitation with FDTD simulations is described and helps not only to design plasmonic waveguides, but also to understand the experimental results presented in chapter 7.

2.3.1 Basic Geometry - The Two-Wire Transmission Line

The design of an optically driven plasmonic TWTL is illustrated in figure 2.12 a. Two shortcuts connect the metal wires - the incoupler at the beginning and the mode detector at the end of the structure. An optical excitation at the incoupler launches plasmons into the TWTL, which offers two lowest-order propagating plasmonic modes. Their electric field profiles are depicted in figure 2.12 b. The symmetric mode is confined to the outside of the TWTL, while the asymmetric mode propagates mainly through the gap between the two metal wires. Based on the different mode symmetries (indicated by their charge distribution) a specific plasmonic mode can be excited by controlling the polarization of the incident light (see figure 2.12 a): A light beam polarized parallel (perpendicular) to the waveguide launches the symmetric (antisymmetric) mode. At the mode detector, the plasmonic modes are then separated spatially and radiate into the far-field with corresponding polarization. The antisymmetric mode - confined to the TWTL gap - scatters at the gap termination, while the symmetric mode is unaffected by obstacles in the gap and scatters at the waveguide termination. If the mode detector is long enough, the two plasmonic modes can be distinguished in optical experiments [22].

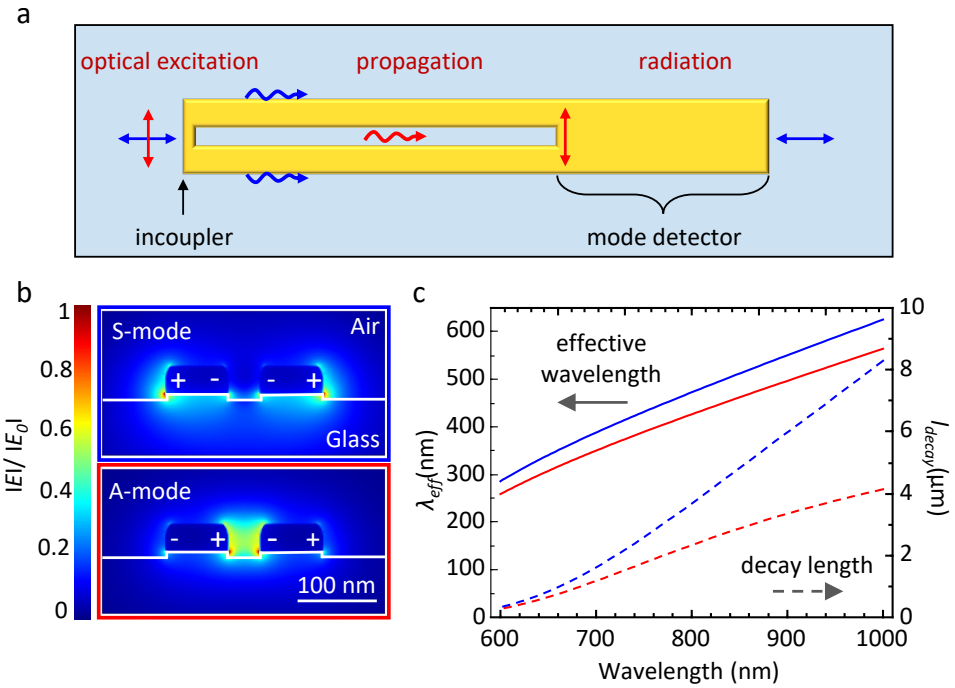

Figure 2.12: Plasmonic two-wire transmission line. (a) Sketch of a plasmonic TWTL with mode detector. Upon optical excitation at the incoupler, two orthogonal plasmonic modes - the symmetric (S; blue) and the antisymmetric (A; red) mode - propagate along the TWTL. At the mode detector, both modes are separated spatially and polarized light is radiated into the far-field. Wavy arrows denote plasmon propagation; straight arrows indicate the polarization of excitation as well as emission for a specific mode. (b) Simulated electric field profile of the two modes. The S-mode is propagating at the sides of the TWTL (close to the substrate), while the A-mode is confined to the gap. Surrounding medium, substrate and charge distribution are denoted. (c) Effective wavelength λ_{eff} (solid) and decay length l_{decay} (dashed) of both modes as a function of free-space wavelength λ. Reprinted and adapted with permission from reference [21]. Copyright (2021) American Chemical Society.

Interestingly, effective wavelength λ_{eff} and decay length l_{decay} are slightly different for both modes (see figure 2.12 c). The antisymmetric mode exhibits stronger confinement, and thus experiences a shorter decay length and a shorter effective wavelength [21]. As discussed previously, λ_{eff} is much shorter than the free-space wavelength (compare section 2.1).

2.3.2 Electrically Driven Plasmonic Waveguides

Distinct modes in plasmonic TWTLs can not only be excited optically, but also electrically. Therefore, the IET mechanism presented in subsection 2.2.2 is reapplied. The waveguide is connected to an external voltage source via a thin metal wire and a small nanoparticle is introduced to create a tunnel junction between connection wire and waveguide (see figure 2.13). As the TWTL provides plasmonic modes, the energy of an electron tunneling inelastically can not only be transferred to a photon but also to a propagating plasmon.

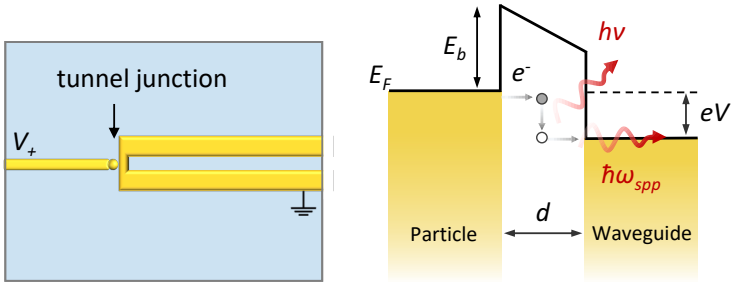

Figure 2.13: Illustration of the electrical excitation. Left: A TWTL is connected by a thin metal wire. Similar to optical nanoantennas a small sphere between connector and TWTL is used to create a tunnel junction (see subsection 2.2.2). Right: Light generation is based on inelastic electron tunneling. As a voltage V is applied, an electron (e^-) tunnels inelastically across a nanometer gap (width d, height E_b) and the energy difference eV is coupled into a plasmon ($\hbar\omega_{spp}$) or photon ($h\nu$). E_F denotes the fermi energy. Reprinted and adapted with permission from reference [21]. Copyright (2021) American Chemical Society.

Coupling between the emitter, *i.e.* IET across a tunnel junction, and a specific mode depends on the local density of states at the location of the emitter. Hence, the exact position of the tunnel junction matters. In optical antennas, for example, the emitter is located in the strongly enhanced electric fields of the feed gap allowing to efficiently excite the bonding mode (see subsection 2.2.2). But where to place the tunnel junction in plasmonic waveguides?

FDTD simulations carried out by Luka Zurak were used to study the influence of the tunnel junction's location [21]. In an intuitive approach, a dipole representing the tunnel junction is placed at different positions close to the incoupler and excites propagating plasmons (see figure 2.14 a). FDTD now allows to calculate the incoupling efficiency I_m, *i.e.* the ratio of power transferred from the dipole to a specific mode m and the dipole power in vacuum. However, this approach requires extensive computation as all possible dipole positions have to be compared in order to maximize I_m. A different approach, utilizing the reciprocity of the system, is depicted in figure 2.14 b and c. The mode of interest is fed into the waveguide from the right and propagates towards the incoupler [98].

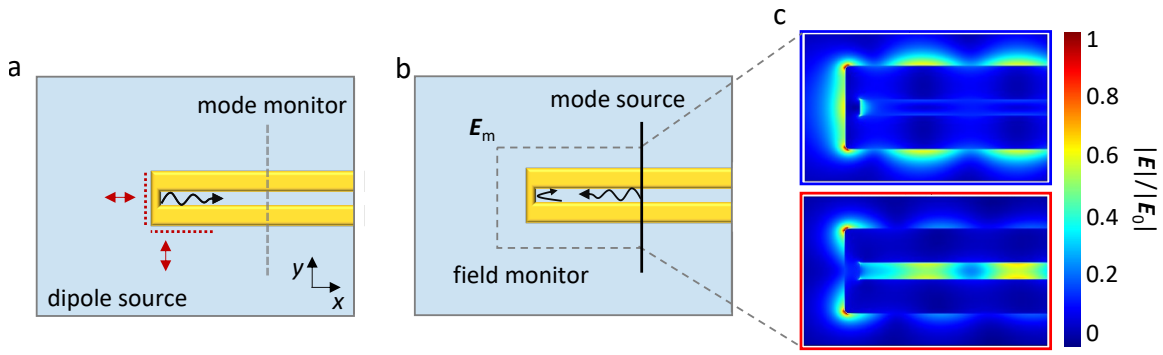

Figure 2.14: Modeling the excitation of plasmonic modes with FDTD. (a) Dipole approach: The dipole source is placed at different positions (dotted green lines) and the power coupled into the modes is calculated at the mode monitor 600 nm away from the excitation. (b) Mode approach: The mode of interest is coupled in from the right (mode source) and propagates towards the incoupler. Upon reflection, a standing wave pattern forms and electric fields are collected using a field monitor. (c) The resulting field distribution for symmetric (blue) and antisymmetric mode (red). Reprinted and adapted with permission from reference [21]. Copyright (2021) American Chemical Society.

Upon reflection a standing wave pattern forms representing the modal field distribution $E_m(r)$. Next, the incoupling efficiency I_m at position r_0 can be written as [21]

$$I_m = \frac{1}{N_m} \frac{3\pi\varepsilon_0 c^3}{4\omega^2} \left| E_m(r_0) \cdot \hat{\mu} \right|^2 , \tag{2.19}$$

with the characteristic mode power N_m (this is the poynting vector integrated over the waveguide profile, the electric field amplitude is normalized to 1 V/m) and the direction of unit vector $\hat{\mu}$. This means, the incoupling efficiency is directly linked to the modal field E_m at the position of the tunnel junction (r_0) via LDOS enhancement. Placing the tunnel junction into the high electric fields of a mode, leads to strong plasmon excitation. As symmetric and asymmetric mode exhibit different electric field distributions (see figure 2.14 c), one can find positions for the tunnel junction at which only one of the modes is excited, with negligible contribution of the other mode. Later in this thesis, the experimental demonstration of this concept is presented (see chapter 7). Note, that for optical antennas the connection wires are placed such that their influence on the antenna resonance is minimal. However, this is not feasible in this waveguide geometry. Consequently, plasmons propagating along the connection wires away from the waveguide constitute an additional loss channel. For more information about the influence of the connector-gap geometry as well as a thorough comparison between dipole and mode approach see the supplementary information of reference [21].

The spectrum of light emitted at the mode detector can be modeled according to the following equation [62]:

$$S_m(\lambda) \propto \eta^0_{src} \cdot \frac{\rho_m}{\rho_0} \cdot \eta_{p-r_m}. \tag{2.20}$$

Here, η^0_{src} is the efficiency of inelastic electron tunneling in vacuum (ratio of inelastic and elastic tunneling). It is similar to the current power spectrum $C(\omega)$ and exhibits the same spectral shape (see equation 2.17 and figure 2.8 a). The second term of equation 2.20 describes the LDOS enhancement at the position of the tunnel junction. It is the ratio of LDOS provided by a mode ρ_m (including tunnel junction) and LDOS in vacuum ρ_0. The radiation-propagation efficiency η_{p-r_m} includes all non-radiative losses that occur during propagation along the waveguide and radiation at the mode detector. Using FDTD, one can calculate the last two terms of equation 2.20. By comparing the power radiated at the end of the waveguide to the incoupled power, one obtains $\frac{P_m}{P_0} = \frac{\rho_m}{\rho_0} \cdot \eta_{p-r_m}$ (compare to equation 2.15).

3 | Introduction to Surface Modification

Surfaces play a key role in defining the properties of nanoscale objects. As the surface area of a particle declines slower than its volume, a large amount of atoms in nanoscale objects are located at or close to their surface and most chemical, optical and electronic properties are dominated by particle interfaces. Consequently, tuning the interfacial environment by chemically modifying the metal surface has become a popular route to tailor device properties.

Since their discovery on rough gold surfaces [99, 100], thiol-terminated self-assembled monolayers (*SAMs*) have emerged as one of the main tools to modify not only flat gold, but also nanostructures [101–103]. They comprise individual molecules binding to gold, and attractive intermolecular forces lead to the formation of higher-order structures (the monolayer). Among the most common *SAM* components are linear alkanes as well as polyethylene glycols (*PEGs*), but it is the chemical variability of *SAMs* that enables the addition of advanced functionality to nanoscale devices. This includes the preparation of hydrophobic or hydrophilic surfaces for applications in the field of biochemistry [102] as well as tuning device properties in organic electronics [104].

In this thesis, the electrical connection of nanostructures is used to enable selective functionalization of nanoscale objects with alkanethiol and thiolated *PEG SAMs*; hence offering an additional degree of freedom to the design and development of nano-optical systems. This chapter is devoted to the basic principles of *SAM* functionalized gold surfaces and electrodes. First, I explain the formation of *SAMs* using alkanethiols as an example. The surface crystallinity plays an important role in *SAM* growth, and here, single-crystalline gold ($Au\,(111)$) is considered to match the experimental conditions. Next, the influence of a tightly packed *SAM* on the metal work function is discussed. This effect not only allows to measure the presence of molecules on a gold surface, but also offers the ability to tune charge injection barriers at metal-organic contact electrodes. The chapter is concluded by introducing the principles of electrochemical desorption which is the foundation for the site-selective functionalization of nanostructures, such as optical antennas. The corresponding experimental demonstrations are presented in chapter 5.

3.1 Self-Assembled Monolayers on Gold Surfaces

SAMs consist of individual molecules binding to a metal surface. The interaction between these subunits can lead to the assembly of a more complex structure, *i.e.* a monolayer of molecules standing almost upright. In the context of this section, alkanethiols on clean *Au* (111) are used as a model system. Note, that growth and order of *SAMs* strongly depend on the type of molecule as well as the substrate.

Figure 3.1 a illustrates a decanethiol molecule (*C10-SH*) within a standing-up *SAM*. It consists of - like any other *SAM* molecule - an anchor group (sometimes called head group), a backbone (hydrocarbon chain) and a terminal group (methyl). The anchor is a thiol (*SH*) able to bind to gold. X-Ray photoelectron spectroscopy and other measurements suggest the scission of the *SH* bond and subsequent formation of a covalent *Au-S* bond, although the fate of the hydrogen atom remains controversial. This bond is relatively strong with an interaction energy of 30 - 50 kcal/mol (126 - 209 kJ/mol or 1.3 - 2.2 eV; the reported values vary depending on the exact measurement technique) [101, 103]. I would like to note that even though most experimental data favors a covalent bond, it has recently been proposed that the physisorbed character of the Au-SH bond prevails in break junction measurements [105].

Hydrocarbon chains of alkanethiols attract each other via van der Waals interaction leading to the formation of a densely packed monolayer of molecules. The interaction energy is reported to be 1 - 2 kcal/mol per methylene; meaning that the stability increases with chain length. As displayed in figure 3.1 a, the molecules are not completely perpendicular to the substrate, but exhibit a tilt angle α, which is about 30 ° for linear alkanethiols [103]. The exact orientation is not only determined by the interaction between hydrocarbon chains but also by the directional gold-sulfur bond, and is molecule dependent [106, 107]. Note, that *SAM* backbones are not limited to hydrocarbon chains, but *PEGs*, aromatic rings and other molecular units are also possible [102, 108].

The terminal (or active) group can be modified in order to introduce different functionality to the *SAM*. While decanethiols are terminated by a simple methyl group (CH_3) leading to a hydrophobic *SAM*, alkanethiols terminated by a hydroxy group (*OH*) form hydrophilic surfaces. Moreover, functional end groups can serve as a docking station for more complex molecules, *e.g.* DNA, peptides or light emitting chromophores [102, 106].

In this thesis, *SAM*s are grown from solution and the exact procedure is described in subsection 4.1.4. The self-assembly of alkanethiols comprises the following individual steps (see figure 3.1 b) [103]: (i) First, molecules physisorb on the gold surface due to van der Waals interaction between hydrocarbons and substrate. The interaction energy scales almost linearly with chain length and is reported to be about 15 kcal/mol for decanethiol [101]. (ii) As molecules

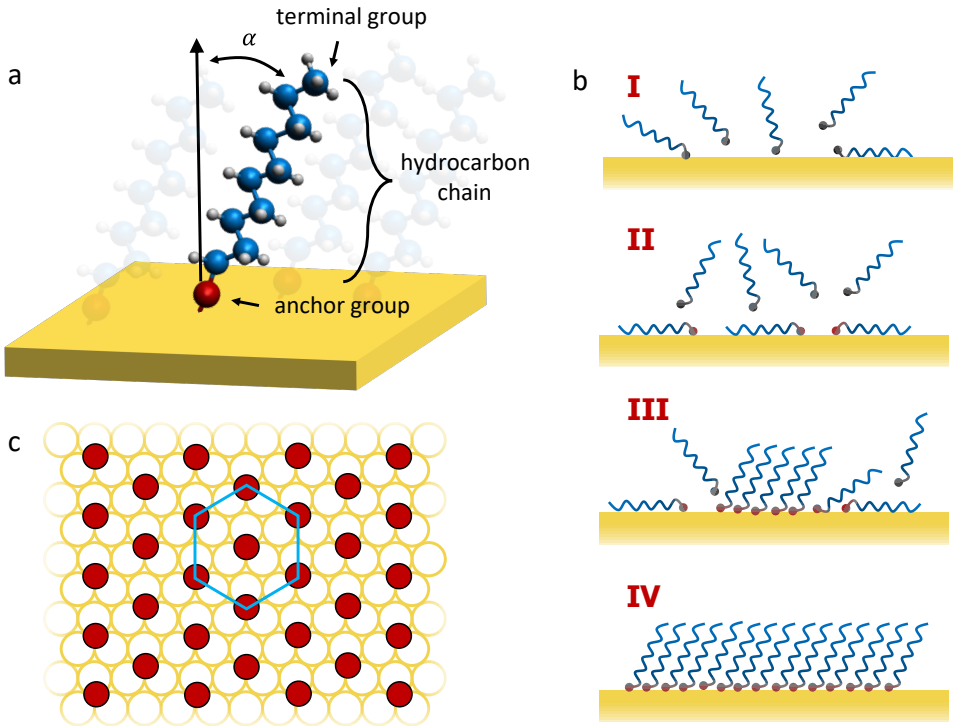

Figure 3.1: Self-assembled monolayers on gold. (a) Illustration of decanethiol on *Au* (111). Individual molecules are tilted by an angle α and consist of a terminal group (here CH_3), a hydrocarbon chain and a anchor group (sulfur). Blue: carbon; grey: hydrogen; red: sulfur. (b) Different steps of *SAM* formation. I: Physisorption. II: First molecules are chemisorbed (red anchor group). III: Formation of standing-up phase. IV: Growth of standing-up phase. (c) Schematic of alkanethiol arrangement on *Au* (111). Gold atoms are illustrated as open circles, while the anchor groups of chemisorbed *SAM* molecules are displayed in red. The hexagonal structure is highlighted. (a) and (b) are inspired by reference [103]. (c) is inspired by reference [106].

remain close to the surface for long enough, the probability of chemisorption increases. After an activation barrier of 7 kcal/mol (0.3 eV) is overcome, the aforementioned *Au-S* bond is formed with an interaction energy said to be independent of chain length (30 kcal/mol for decanethiol; energy values are typically determined via temperature programmed desorption after the *SAM* is deposited from gas phase in ultrahigh vacuum, and, thus, the conditions in solution are not exactly matched) [101, 109]. This process can take a few minutes and is usually accompanied by the formation of a lying-down (or stripped) phase of molecules. In this context, I would like to mention the possible reconstruction of the gold surface, which has gained increased interest in the *SAM* community over the last years [103]. Upon chemisorption, gold atoms are lifted from the surface of the substrate, become adatoms and facilitate *S-Au-S* bonds. It has been shown that these adatoms form gold islands on the surface after the

SAM is desorbed [110]. While this process is not completely understood, it might explain why molecules preferentially bind to defect sites as surface reconstructions are energetically less favored on perfectly crystalline substrates. (iii) Next, small islands of standing-up molecules are formed due to the interplay of van der Waals interaction and the *Au-S* bond. Transition from lying-down to standing-up molecules is accompanied by surface stress, which should be considered for the functionalization of fragile nanostructures. (iv) These islands grow and form densely packed crystalline monolayers – a process, which takes several hours to days depending on the molecule. As a rule of thumb, the required time increases as the chain length decreases. Note, that self-assembly in solution involves the displacement of solvent molecules as well as substrate adsorbates throughout all four steps.

SAMs (especially alkanethiols) exhibit ordered domains commensurate to the crystallinity of the underlying substrate. This can be observed by a variety of measurement techniques, *e.g.* scanning tunneling microscopy. The most common alkanethiol structure on *Au* (111) is the hexagonal arrangement shown in figure 3.1 c (in Wood's notation: $(\sqrt{3} \times \sqrt{3})R30°$). In this illustration, filled red circles represent the thiols of *SAM* molecules binding to gold atoms (open circles) with a distance of 0.5 nm between nearest neighbours [103]. Other surface structures have been observed as well, such as the $c(4 \times 2)$ superlattice, but are not described in detail here (see references [101–103] for more information).

Regardless the final molecule arrangement, *SAM* quality strongly depends on the quality of the underlying surface. But defect free *SAMs* do not exist, with possible imperfections being missing molecule rows or vacancies. Furthermore, it has been reported that *SAMs* degrade over time due to ozone exposure and ultraviolet radiation [111]. Defect-heavy surfaces, *e.g.* nanostructures fabricated via focused ion beam milling, exhibit *SAMs* with lower quality, however, they seem to be more resistant to *SAM* degradation making nanostructures an intriguing platform for *SAM* functionalization [103].

In this work, *SAMs* of 1-octadecanethiol (*C18-SH*) and the specifically designed fluorescent *C-PEG* are grown. While the basic principles of self-assembly apply to *PEGs* as well, these molecules do not form *SAMs* which are as densely packed and upright-standing as alkanethiols. Instead of straight chains, *PEGs* exhibit helical or zigzag chains, which are located closer to the gold surface [112, 113].

3.2 Tuning the Metal Work Function

One specific and extensively studied effect of *SAMs* is the modification of the metal work function [103, 114–117]. This not only allows to tune electronic properties in metal-organic devices, but also to verify the presence of a *SAM* by measuring the change in work function, *e.g.* via Kelvin probe force microscopy (KPFM; see subsection 4.2.4). Figure 3.2 a depicts the influence of an alkanethiol *SAM* on the gold work function W_{Au}, which represents the minimum energy needed to remove an electron from the metal surface. Upon *SAM* adsorption, the surface dipole at the *Au-SAM* boundary is changed and the vacuum energy level shifts, leading to a modified work function W_{Au+SAM}.

The shift can be derived quantitatively by treating the surface dipole layer as two parallel charge sheets with distance l and surface charge density σ (given by the amount of *SAM* molecules per area). The potential drop $\Delta\Phi$ caused by the *SAM* is now obtained by integrating the electric field over the entire dipole layer [114]:

$$\Delta\Phi = \int_0^l \frac{\sigma}{\varepsilon_r\varepsilon_0} dx = \frac{\sigma l}{\varepsilon_r\varepsilon_0} = -\frac{Nel}{\varepsilon_r\varepsilon_0} = -\frac{N\mu_\perp}{\varepsilon_r\varepsilon_0}. \tag{3.1}$$

ε_0 and ε_r are the vacuum and dipole layer permittivity, N is the molecule density (about $10^{18}\mathrm{m}^{-2}$) and $\mu_\perp$ is the total dipole moment perpendicular to the surface. As shown in figure 3.2 b, chemisorbed *SAMs* can further be divided into two dipole layers, the *SAM* dipole μ_{SAM} (pointing towards the surface in this example) and the dipole originating from the covalent *Au-S* bond μ_{Chem} (pointing away from the surface). This leads to the following expression for the work function change relative to a clean *Au* (111) surface

$$\Delta W = -eN\left[\frac{\mu_{SAM}}{\varepsilon_{SAM}\varepsilon_0} + \frac{\mu_{Chem}}{\varepsilon_{Chem}\varepsilon_0}\right], \tag{3.2}$$

with ε_{SAM} and ε_{Chem} being the relative permittivities of the respective dipole layers. μ_{Chem} is a direct consequence of the electron reordering in molecules and gold surface upon chemisorption and is approximately the same for all *SAMs* with a single thiol group. Its contribution is very weak, and, thus, ΔW is dominated by μ_{SAM}, which depends on the *SAM* backbone and terminal group [115]. For this reason, the direction of the *SAM* dipole determines the sign of the work function change. Pure alkanethiols terminated by CH_3 exhibit a dipole pointing towards the surface and therefore lower the work function (see figure 3.2; the negative part of the dipole is closer to the substrate). By introducing a strongly electronegative terminal, *e.g.* CF_3 the dipole direction reverses and the work function is increased [115, 118, 119]. Importantly, μ_{SAM} is the dipole component of the *SAM* perpendicular to the surface; hence, it also depends on the molecule orientation within the *SAM* (tilt angle in figure 3.1 a). For example, a

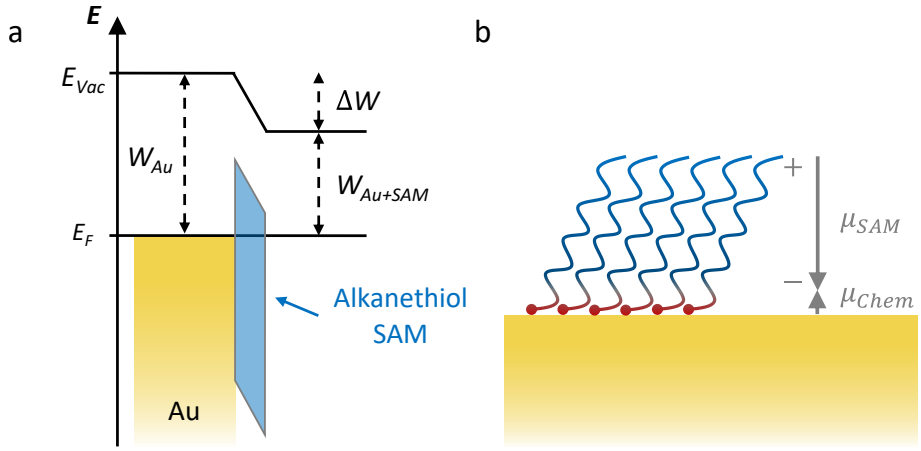

Figure 3.2: Tuning the work function. (a) The alkanethiol *SAM* introduces an interface dipole at the *Au-SAM* boundary which lowers the vacuum energy E_{Vac} and consequently reduces the work function to $W_{Au} - \Delta W = W_{Au+SAM}$. E_F is the fermi energy. (b) Alkanethiol *SAMs* on gold are modeled as two dipole layers (green arrows) including the *SAM* dipole component perpendicular to the surface (μ_{SAM}) and the dipole resulting from the gold-sulfur bond (μ_{Chem}). Plus and minus signs exemplarily denote the charge distribution along μ_{SAM}.

SAM molecule with a strong inherent dipole moment, but rather flat orientation parallel to surface is not leading to large ΔW. According to UV-photoelectron spectroscopy measurements in vacuum, alkanethiols on *Au* (111) lead to a work function reduction of 1 - 1.4 eV [116, 117]. KPFM measurements carried out under ambient conditions typically observe smaller values due to measurement artifacts and disturbing water layers as discussed in chapter 5.

3.3 Electrochemical Desorption of Self-Assembled Monolayers

In the following subsection I want to quickly present the electrochemical desorption of chemisorbed *SAMs* from *Au* (111) surfaces, which was first reported by Widrig *et al* [120]. Typically, this procedure is carried out in cyclic voltammetry cells in order to apply well known electric potentials to the *SAM* covered metal surface (working electrode) relative to a calibrated reference electrode, while all electrodes are immersed in a basic electrolyte such as *KOH* or *NaOH*. As the voltage is slowly swept to higher potentials, *Au-S* bonds are broken and *SAM* molecules are desorbed from the gold surface. This reaction occurs at reductive and oxidative potentials of about $\pm$1 - 1.5 V depending on the type of electrolyte, its concentration and the exact *SAM* molecule [120–125]. The electrolyte plays a key role in desorption; it not only facilitates the electrochemical processes, but

also solvates and stabilizes desorbed molecules in micelle and bilayer structures that can be washed away in a subsequent rinsing step [126]. Due to its simple reaction mechanism involving the transfer of a single electron, reductive desorption has been investigated more often. It is based on the following reaction [120]

$$AuSR + 1e^- \longrightarrow Au(0) + RS^-. \tag{3.3}$$

Measuring the current flowing between the *SAM* covered metal surface and a counter electrode now allows to calculate the amount of thiolated molecules that has been removed from the surface. However, desorbed thiolate moieties remain close to the surface which is still covered with electrolyte and might readsorb. In contrast, the mechanism of oxidative desorption is more complex and might involve the transfer of multiple electrons according to the following reactions

$$AuSR + 2H_2O \longrightarrow Au(0) + RSO_2^- + 3e^- + 4H^+, \tag{3.4}$$

$$AuSR + 3H_2O \longrightarrow Au(0) + RSO_3^- + 5e^- + 6H^+. \tag{3.5}$$

Resulting sulfinates (RSO_2^-) and sulfonates (RSO_3^-) have a much lower binding affinity to gold than thiolates, and thus, this process is less affected by readsorption of molecules [111, 124, 127]. For this reason, oxidative desorption is used in order to achieve site-selective functionalization of nano-optical systems, which is presented in chapter 5.

4 | Experimental Techniques

Surface quality and well defined geometries are decisive for the optical properties of nanostructures. In order to manufacture devices with reproducible performance, small fabrication tolerances are required. For example, imperfections in nanoantenna fabrication, such as few-nanometer deviations in gap size, lead to strong resonance shifts (see section 2.2.1). In this regard, the Nano-Optics Group at the University of Würzburg has performed pioneering work and advanced the fabrication of nano-optical systems by establishing single-crystalline gold platelets as base material. This enables the reproducible fabrication of ultrasmooth nanostructures with improved optical properties compared to their polycrystalline counterparts [14]. Building on this foundation, my colleagues and I have developed advanced fabrication techniques and continuously improved existing methods over the last years. Furthermore, we have set up a variety of optical and optoelectronic laboratories that allow for in-depth characterization of nano-optical systems.

This chapter is divided into two parts: Section 4.1 outlines the production line for electrically connected nanostructures. In the beginning, I present the sample layout and explain general preparation steps. Next, the top-down fabrication of nanoantennas and waveguides via focused ion beam (FIB) milling is described. This procedure has been continuously improved throughout my thesis and is still subject to further development. Tunnel junctions for electrically driven nanodevices are prepared in a separate step. In the past, electron tunneling was facilitated by pushing gold nanoparticles into the antenna gap using an atomic force microscope (AFM) tip [43]; however, this approach has a low yield and is not suitable for complex geometries such as Yagi-Uda antennas. For this reason, I developed a method based on dielectrophoresis (DEP). Its concept as well as the employed setup are discussed in this chapter. Moreover, I describe the procedure to deposit self-assembled monolayers (*SAMs*) on gold surfaces, a bottom-up technique to further tune properties of nano-optical systems.

Section 4.2 summarizes the employed measurement techniques. White-light dark field (WL) scattering and electroluminescence (EL) measurements are used to characterize nanoantennas as well as plasmonic waveguides. In addition, I describe the setup used to acquire photoluminescence (PL) maps, and explain the concept of Kelvin probe force microscopy (KPFM). Both methods are em-

ployed to verify the site-selective *SAM* functionalization of gold electrodes.

Text and figures of this chapter are adapted from the supplementary information of references [20, 21].

4.1 Sample Fabrication

4.1.1 General Sample Layout and Preparation

Single-crystalline gold platelets (*Au* (111)), grown by a previously described wet-chemical synthesis [53, 54], have been established as the base material for plasmonic nanostructures. In contrast to evaporated polycrystalline gold, they do not suffer from grain boundaries, and thus offer advanced optical properties and allow for more precise fabrication [14, 24, 43]. However, directly connecting platelets to a voltage source, *e.g.* by contacting them with micromanipulator needles, remains challenging due to their stiffness [43]. As an alternative, platelets are placed on softer, evaporated gold electrodes, which facilitate the electrical contact.

The sample layout is depicted in figure 4.1 a. Three *Au*/*Cr* electrode areas (70nm/5nm thickness) with six top, six bottom and one ground contact are evaporated on a microscope cover slip (#1, Gerhard Menzel GmbH, Saarbrücken, DE). Single-crystalline gold platelets with lateral sizes of ~100 µm and thicknesses of ~50 nm are grown on separate glass substrates and subsequently placed in the center of the electrode areas using an in-house developed transfer technique: individual platelets are encapsulated with droplets of Polymethylmethacrylate (PMMA) and tempered at 100 °C for 1 hour. The hardened droplets containing the platelets are then transferred to the electrodes using a micromanipulator needle. After further drying the droplets for 5 hours at 100 °C, the PMMA is removed by an acetone bath or acetone steam. Next, FIB milling is used to process the platelets and fabricate nanostructures (see subsection 4.1.2).

An exemplary gold platelet after FIB is shown in figure 4.1 b. The platelet is cut into several parts, each contacting at least one of the 13 evaporated *Au*/*Cr* electrodes. It contains ten electrically connected and isolated nanoantennas (a maximum of twelve per platelet is possible), one of which is depicted in figure 4.1 c and d. Two straight connection wires connect the antenna to the remaining platelet, and thus to two evaporated electrodes. Owing to the good electrical contact between platelet and *Au*/*Cr* electrodes, a voltage can now be applied to the antenna by contacting the macroscopic *Au*/*Cr* electrodes with micromanipulator needles (see subsection 4.2.2) [20, 21].

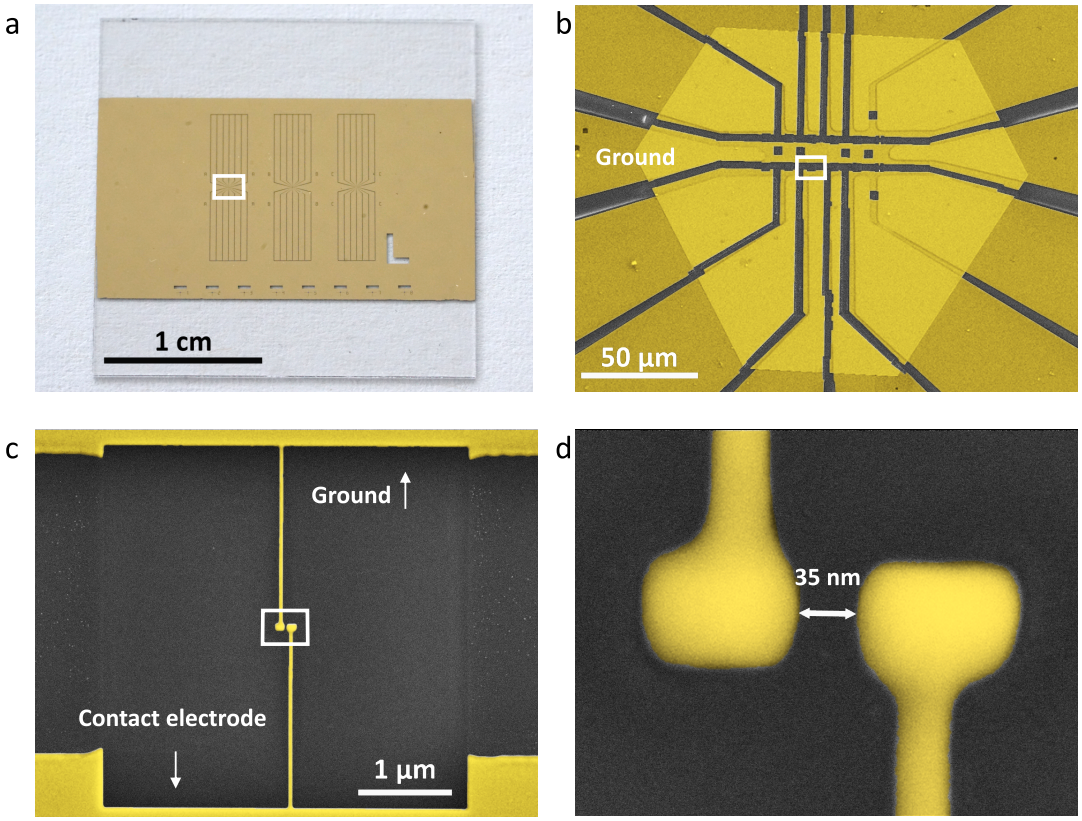

Figure 4.1: General Sample Layout. (a) Optical photograph of a sample chip. It consists of a microscope glass cover slip with three evaporated *Au/Cr* electrode structures. (b) SEM image of single-crystalline gold platelet which was transferred to the center electrode structure (white rectangle in (a)) and subsequently processed by focused ion beam milling. (c) Electrically-connected nanoantenna milled into the gold platelet via focused ion beam milling (see white rectangle in (b)). (d) Zoom-in to the antenna region showing a feed gap of 35 nm after gold etching.

4.1.2 Focused Ion Beam Milling

Fabrication of accurate nanostructures requires advanced FIB milling of single-crystalline gold platelets. Multi-element systems, *e.g.* optical Yagi-Uda antennas (see figure 1.1 c), are especially demanding as individual elements must be accurately structured and positioned in close proximity. Moreover, the directionality of these antennas strongly depends on their dimensions. Gallium FIB achieves minimum beam diameters of ~10 nm (at 30 kV acceleration voltage), and thus, allows to fabricate nanostructures with higher resolution than conventional optical lithography techniques [128]. Here, I am going to explain the concept of FIB milling and describe the advanced fabrication process employed in this thesis, which also includes etching of gold [20, 21]. The FIB procedure

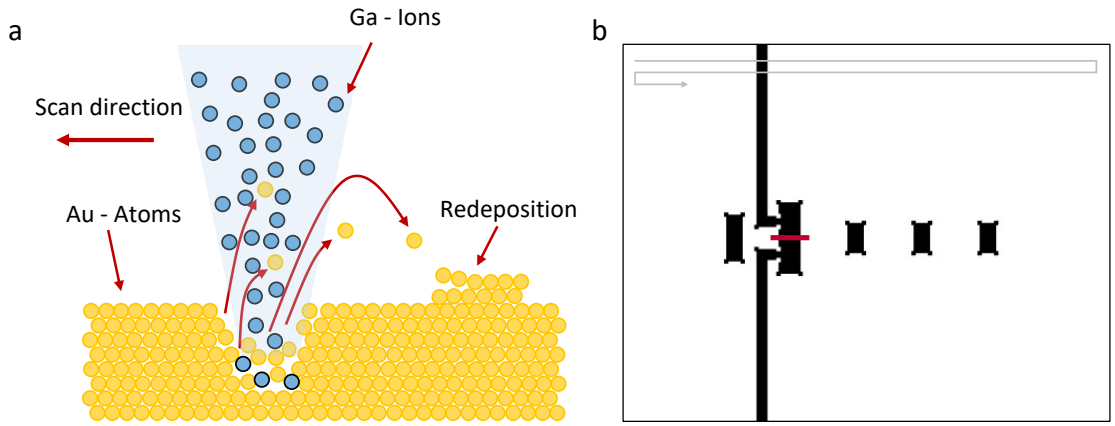

Figure 4.2: Focused ion beam milling. (a) Illustration of the milling process. Gallium (Ga) ions are accelerated onto the surface and subsequently remove gold atoms, which are redeposited opposite to the scan direction. (b) Bitmap image used to fabricate optical Yagi-Uda antennas. The image is loaded into the machine and the white area is milled in two steps, first from top to bottom (along the grey arrow) and then from bottom to top. The gap is milled afterwards (denoted by red line). Extra pixels are added to the corners of the individual structures to realize well shaped features. In the end, the black elements remain and form the optical antenna. Adapted from reference [74].

is constantly being improved in our research group, specifically since the inception of a helium ion microscope (HIM; Zeiss Orion NanoFab). Yet, in this thesis, most nanostructures are fabricated exclusively using a Helios Nanolab 600 (FEI) equipped with a scanning electron microscope (SEM) and a gallium FIB.

Before FIB, one has to choose proper gold platelets, which are suitable for the structures of interest. As a rule of thumb, thinner gold platelets allow narrower FIB cuts. Here, platelets with thicknesses of 30 - 40 nm are used for demanding nanostructures such as Yagi-Uda antennas, while thicker 50 nm platelets can be used for less demanding plasmonic waveguides. Charge-induced drift during the milling process is avoided by employing a custom-made sample holder grounding all macroscopic Au/Cr electrodes.

Figure 4.2 a illustrates the milling principle. Gallium (or helium) ions are accelerated to energies of around 30 keV and directed at the gold surface. Upon impact, the ions have enough kinetic energy to remove gold atoms from the platelet, which then redeposit opposite to the scan direction. As the ion beam is scanned across the surface, structures of arbitrary shape can be manufactured [14]. Nanostructures are typically milled with an ion current of 10 pA, while larger gold areas are removed with higher dose.

In practice, the target geometry is transcribed from bitmap images; such a file for Yagi-Uda antennas (compiled using Matlab scripts) is depicted in figure 4.2 b. The structure is milled based on the color code of the pixels: while the ion

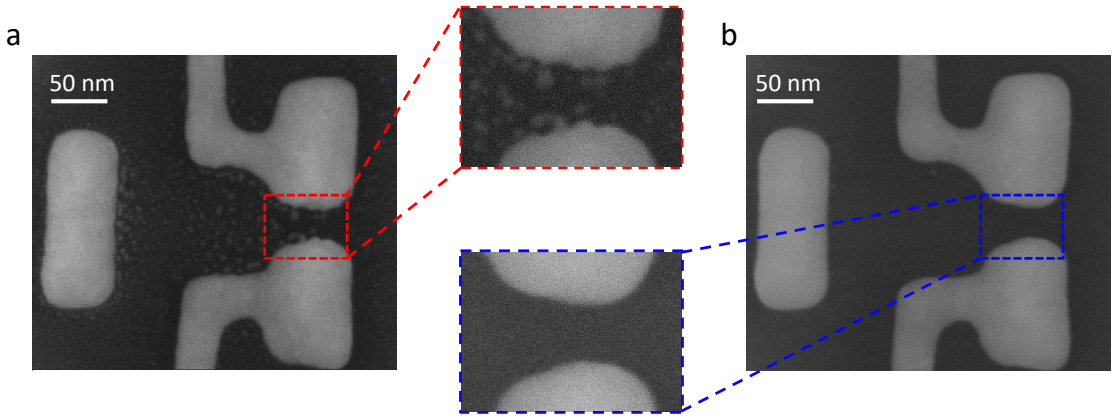

Figure 4.3: Gold etching. SEM images of an optical Yagi-Uda antenna (a) before (b) after gold etching. Dashed squares depict zoom-ins into the feed gap region. Taken from reference [20].

beam is turned off at black pixels, the white area is milled with constant, but specifically set dwell time. This is the time the beam stays at a certain pixel, and is thus correlated to the milling depth. Extra pixels at corners are added or omitted to reduce proximity effects and to obtain well defined features. In order to minimize redeposition effects and achieve symmetric shapes, the structure is first milled from top to bottom (following the grey arrow in figure 4.2 b), and then again from bottom to top. Afterwards, the feed gap is fabricated with a single line cut (see red line in figure 4.2 b) ensuring accurate and reproducible gap sizes of 30 nm. Not just Yagi-Uda antennas, but almost all electrically connected structures are fabricated according to this procedure. Only the sharp gaps of particular waveguide structures are manufactured with HIM, as helium ion milling offers even finer features with a resolution approaching 1 nm. This is quickly discussed in chapter 7 and reference [21].

Figure 4.3 a shows that small gold clusters remain around freshly milled antenna elements and inside the feed gap. These residuals cause leakage currents upon applying an electromagnetic field and interfere with DEP as well as EL measurements. Gaps are cleaned by applying a home-made etching solution of iodine and potassium iodide for 15 - 25 s ($I_2 : KI : H_2O = 1\,mg : 4\,mg : 40\,ml$ and then further diluted 1:1000 with purified water). After etching, the structures are imaged via a Zeiss Gemini 2 SEM to see if the gaps are indeed clean. The process of etching and SEM imaging can be repeated multiple times, but one etching step is typically sufficient. As depicted in figure 4.3 b, gold etching slightly enlarges the gap, but also removes all residuals resulting in well defined feed gaps. Next, the devices are optically characterized using WL scattering (see subsection 4.2.1) and are then ready for the next fabrication steps (either DEP or *SAM* formation). [21].

4.1.3 Dielectrophoresis

The tunnel junction is the heart of any electrically driven and light emitting nanostructure presented in this thesis. Inelastic electron tunneling requires ~1 nm gaps, which cannot be milled with gallium FIB. Even helium milling, which basically offers the necessary resolution, is not suitable as tiny gaps tend to close again after the cut. Electromigration has been used to create break junctions for tunneling experiments [46, 49, 129], however, this process results in unstable gap geometries (and thus unstable currents) and lacks the required reproducibility. Better stabilities are achieved by fabricating 25 - 30 nm gaps via FIB and further reducing their size by inserting 30 nm gold particles coated with a 1 nm insulating organic shell. This was previously realized by a drop-and-push approach [43]. A particle containing water droplet was deposited on the sample and, after the droplet dried, particles were pushed into the feed gap using an AFM tip. Although this method worked for proof-of-principle structures, it has low yield and is not applicable to sophisticated geometries *(e.g.* the Yagi-Uda design). Particles cannot be pushed over large distances, thus a coverage of one particle per micrometer is necessary, and stick to antennas at unintended locations. Moreover, excess particles close to the nanostructure need to be removed in order to not disturb the optical characterization. I therefore implemented a process based on dielectrophoresis (DEP) [130], which takes advantage of the strong electric fields in the gap of nano-optical systems such as optical antennas. By simply applying an AC voltage to the antenna, a nanoparticle, which is dissolved in a water droplet, is pulled into the feed gap leading to 1 nm tunnel junctions between coated particle and antenna arm. The theory of this procedure as well as the measurement setup are described below. Corresponding experimental results are shown in chapter 6 and 7.

A polarizable particle situated in a non-uniform electric field experiences a non-zero net force, *i.e.* the DEP force F_{DEP}. For a homogeneous sphere with radius R that is suspended in a medium with dielectric function ε_1 the time-average force has the expression [131]

$$\langle F_{DEP} \rangle = 2\pi\varepsilon_1 R^3 Re\left[K(\omega)\right] \nabla E_{rms}^2. \tag{4.1}$$

E_{rms} is the root-mean-square value of the electric field and $Re\left[K(\omega)\right]$ represents the real part of the frequency dependent Clausius-Mossotti function, which can be written as

$$Re\left[K(\omega)\right] = \frac{\varepsilon_2 - \varepsilon_1}{\varepsilon_2 + 2\varepsilon_1} + \frac{3(\varepsilon_1\sigma_2 - \varepsilon_2\sigma_1)}{\tau_{MW}(\sigma_2 + 2\sigma_1)^2(1 + \omega^2\tau_{MW}^2)}. \tag{4.2}$$

Here, ε_2 is the dielectric function of the particle. σ_1 and σ_2 are the conductivities of surrounding medium as well as particle, respectively, and $\tau_{MW} = \frac{\varepsilon_2+\varepsilon_1}{\sigma_2+2\sigma_1}$ is the Maxwell-Wagner charge relaxation time. Equation 4.1 shows that F_{DEP}

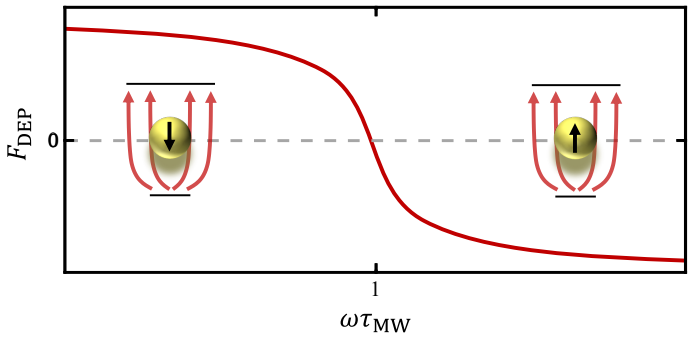

Figure 4.4: Principle of dielectrophoresis. The asymmetric electrodes in the inset create an inhomogeneous AC electric field. At low frequencies, the dielectrophoretic force F_{DEP} is positive and a particle is attracted to regions of high electric field (smaller electrode). At high frequencies, F_{DEP} is negative and the particle is drawn to smaller electric fields (larger electrode). Adapted from reference [20].

strongly depends on particle size and electric field gradient. The direction of the force further depends on the frequency of the applied electric field, which can be seen by simplifying equation 4.2 for high and low frequencies:

$$Re\left[K(\omega)\right] \rightarrow \begin{cases} \frac{\sigma_2-\sigma_1}{\sigma_2+2\sigma_1}, \ \omega\tau_{MW} \ll 1 \\ \\ \frac{\varepsilon_2-\varepsilon_1}{\varepsilon_2+2\varepsilon_1}, \ \omega\tau_{MW} \gg 1 \end{cases} . \tag{4.3}$$

For gold particles dissolved in water (as in this work) one gets $\varepsilon_2 < \varepsilon_1$ and $\sigma_2 > \sigma_1$. Therefore, the force becomes positive at low frequencies and negative at higher frequencies (see figure 4.4). Importantly, particles are attracted (repelled) by regions of high electric field when F_{DEP} is positive (negative).

Optical antennas, which exhibit strongly localized and enhanced fields in their feed gap (see section 2.2), are thus ideal for trapping nanoscale objects. In addition, these nanostructures offer gap size dependent resonances that can be used as feedback. Note, however, that the applied frequency must be carefully chosen in order to place only a single particle of specific size into the gap. If the frequency is too low, the average DEP force pulling the particles becomes too large and multiple objects are quickly drawn to the gap before the voltage is switched off. Having many particles in the gap, however, might disturb subsequent EL measurements. For this reason, multiple DEP tests have been conducted previously to find the optimal frequency for different antenna geometries [20, 74].

The 30 nm gold particles (A11C-30-CTAB-1, Nanopartz) used in this work are suspended in water and covered with Cetrimonium bromide (*CTAB*). The organic shell reduces cluster formation and serves as a 1 nm insulating layer between particle and antenna arm [132]. To further remove particle agglomerates,

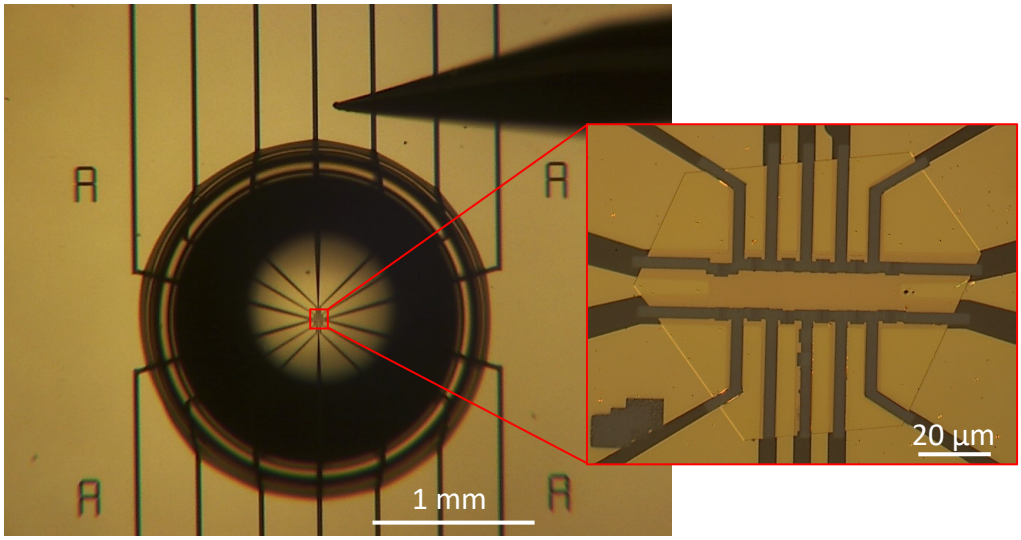

Figure 4.5: Setup of dielectrophoresis. 30 nm gold nanoparticles are immersed in water and drop cast onto an electrode structure containing a processed gold platelet (zoom-in). A micromanipulator needle (above the droplet) is employed to contact the antenna electrodes and apply an AC voltage. This contact scheme is used for all electrical measurements. White-light dark-field scattering spectra can be acquired during this procedure from below (through the glass cover slip). Taken from reference [20].

the solution is sonicated for one minute, diluted 1:500 with purified water (for antennas; 1:5000 for waveguides) and again sonicated for one minute. Next, the sample chip is mounted onto the Nikon setup (cf. subsection 4.2.2), and the solution is drop cast as depicted in figure 4.5. An AC voltage with specific frequency is applied to an antenna by contacting the corresponding Au/Cr electrode with a micromanipulator needle (copper-beryllium; MM-7H, Micromanipulator), which in turn is wired to a frequency generator (DS345, Stanford Research Systems). The second antenna electrode is grounded simultaneously (not visible in figure 4.5). Purified water is added to the sample occasionally to avoid dry out, and after DEP is finished, the droplet is rinsed off with water and ethanol.

In case of optical antennas, the DEP event can be monitored by measuring the antenna's scattering spectrum in real-time, which further increases the success rate. This feedback-controlled DEP is presented in section 6.3. The gap geometry in electrically connected waveguides, however, does not exhibit strong far-field scattering, and thus the feedback is omitted. Instead, a specific voltage is applied for a short and fixed period of time, which has been optimized by performing numerous tests.

The loaded devices (structures filled with a nanoparticle) are now ready for electroluminescence measurements followed by SEM imaging.

4.1.4 Preparation of Self-Assembled Monolayers

Here, 1-octadecanethiol (*C18-SH*) and newly designed *C-PEG* are deposited on *Au* (111) surfaces as a way to further tune electronic interface properties (see chapter 5). The corresponding protocols are outlined in the following.

SAMs of *C18-SH* are prepared by adding 12 mg of molecules (O1858, Sigma-Aldrich) to 15 mL of absolute ethanol. The solution is sonicated for ten minutes, in order to dissolve all molecules. Next, the sample chip is immersed in the solution and the container is backfilled with nitrogen. After an incubation time of about 24 hours, the sample is taken out of the solution, rinsed with absolute ethanol to remove excess molecules and dried with a stream of nitrogen.

C-PEG was specifically synthesized for this work by Laurent Jucker (Department of Chemistry, University of Basel). A few grains of molecules are added to 2 mL of methanol and the solution is sonicated until all molecules are dissolved. The thiol group of *C-PEG* is protected, *i.e.* it is a thioacetate (the molecule structure is depicted in figure 5.1 chapter 5) which is not binding well to gold, but protects the molecules against disulfide formation. In order to grow *SAMs* of *C-PEG*, the thiol group is deprotected by adding a single droplet of sodium methoxide (5.4 M, Acros Organics) to the solution and immersing the sample chip immediately for 20 minutes. Afterwards, the sample is rinsed with purified water and dried with a stream of nitrogen.

4.2 Characterization of Nano-Optical Systems

4.2.1 White-Light Dark-Field Scattering

WL scattering is the standard technique to investigate the optical properties of nanoantennas. As explained in subsection 2.2.1, the resonance of a gold antenna (bonding mode along the antenna axis), and thus its far-field scattering, depend on the dimensions length, width, height and gap size. Therefore, WL scattering yields valuable information about the antenna geometry right after FIB milling. It is used to further optimize the milling and etching procedure, and to predict EL spectra of light-emitting antennas (see figure 2.8). In addition, the gap size sensitivity is exploited to monitor the trapping of individual gold nanoparticles by DEP.

WL measurements are carried out at a Nikon TE2000-U inverted microscope equipped with a nano positioning stage (Nano-LPS200, Mad City Labs Inc.). Figure 4.6 depicts the corresponding beam path [43]. White light of a stabilized halogen lamp (Thorlabs SLS201L/M) is coupled into a 20 µm multi-mode fiber and subsequently coupled out by a reflective collimator (Thorlabs RC08). In order to limit the excitation spot, the beam passes through a 300 µm pinhole followed by an iris aperture. Next, the light is focused (50 cm lens) on the back

focal plane of an oil-immersion microscope objective (Plan-Apochromat, 100×, NA = 1.45, Nikon) to excite individual antenna structures with a collimated beam (diameter of 1 - 2 µm). The light scattered by the antenna is collected using the same microscope objective and a circular beam block is placed into the detection path to remove all direct reflections. Finally, the light is focused onto (20 cm spectrometer lens) and analyzed by a spectrometer (Shamrock 303i, 80 lines/ mm blazing at 870 nm) combined with an electron-multiplied charge-coupled device (EMCCD, iXon A-DU897-DC-BVF, Andor) [20]. The scattering spectra are always normalized to the reflection of glass to account for the transfer functions of all optical elements in the beam path. Conventional spectra are acquired using a stitching method ("step 'n glue", Andor), which covers the wavelength range from 500 nm to 1000 nm. Live spectra for DEP on the other hand, are measured across a variable range with a width of 330 nm. The corresponding WL measurements are presented in chapter 6.

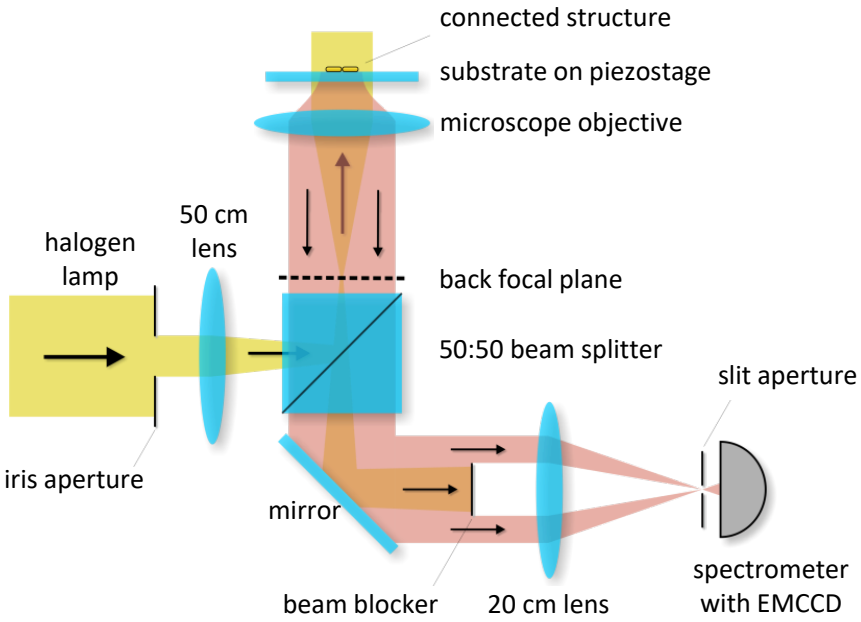

Figure 4.6: Schematic of white-light dark-field scattering. White light from a halogen lamp is focused (50 cm lens) on the back focal plane of an oil-immersion microscope objective in order to illuminate nanostructures with a collimated beam. The scattered light is collected by the same objective and direct reflection is blocked (spherical beam blocker). Next, a 20 cm lens is used to focus the scattered light on a spectrometer with EMCCD. Reprinted by permission from Springer Nature: Nature Photonics [43]. Copyright (2015).

4.2.2 Electroluminescence and Current Measurements

Electrical experiments are of central importance for the fabrication and characterization of electrically connected nano-optical systems. DEP and EL measurements are recorded at the same setup introduced in the previous subsection. The electrochemical desorption of *SAMs* as well as current-voltage characteristics are acquired at an electrical setup with similar equipment.

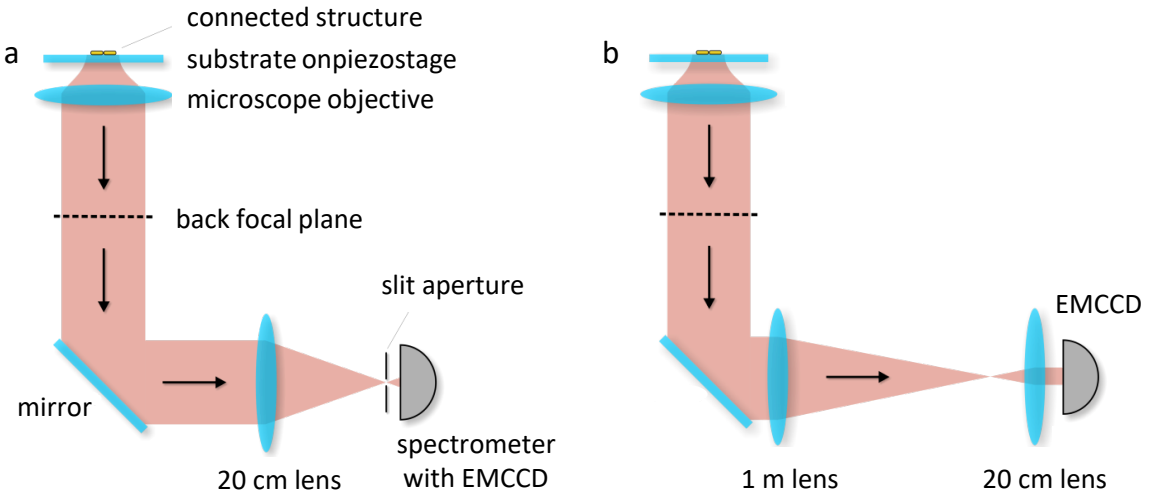

Figure 4.7: Setups for electroluminescence measurements. Upon applying a voltage, optical antennas as well as waveguides emit light, which is collected by an oil-immersion microscope objective. (a) In order to measure spectra, the light is focused (20 cm lens) onto a spectrometer and subsequently detected with an EMCCD. (b) Emission patterns are recorded with the EMCCD by adding an additional 1 m lens. Reprinted by permission from Springer Nature: Nature Photonics [43]. Copyright (2015).

As described above (see figure 4.5), *Au/Cr* electrodes of nanostructures are contacted with copper-beryllium probe needles (MM-7H, Micromanipulator) mounted to micromanipulators (DPP220, Cascade Microtech). *SAM* desorption, EL and current measurements are carried out using a source measure unit (Keithley 2636B, Keithley Instruments Inc.), which is wired to the micromanipulators via triax cables. In order to perform DEP, the Keithley is replaced by a frequency generator (DS345, Stanford Research Systems).

Figure 4.7 a depicts the beam path for measuring EL spectra. The setup resembles that shown in figure 4.6, but the internal beam splitter and the circular beam block are removed. Instead of white light illumination, single devices are excited by applying a DC voltage and the resulting EL is collected and analyzed using the same spectrometer and EMCCD. A Wollaston prism can be added in front of the spectrometer, to split the light into two orthogonally polarized beams. Figure 4.7 b illustrates the setup used to acquire EL emission patterns.

A 1 m lens is added in front of the 20 cm lens and the grating is replaced by a mirror. In order to record the image plane emission (especially for waveguides), the 20 cm lens is removed and the 1 m lens is used to focus on the EMCCD, which results in a magnified image [20, 21].

A home-made LabVIEW program is employed to synchronize the source measure unit (Keithley) and EMCCD camera throughout all EL measurements. Typical integration times are 100 ms for spectra, 1 - 10 s for image plane and 30 s for emission patterns. The corresponding EL measurements are presented in chapter 6 and 7.

4.2.3 Photoluminescence

PL maps are recorded to observe light emitting *C-PEG* molecules on gold surfaces, and, hence, help to verify the site-selective *SAM* functionalization presented in chapter 5. These measurements are carried out at a different setup; its beam path is depicted in figure 4.8 a.

Light from a 532 nm laser diode (AIST-NT ROU006) is reflected by a dichroic mirror (Thorlabs Di01-R532) and focused on the top side of the sample using a 50 x air objective (Olympus MPlanFLN; NA = 0.8). Photoluminescence is recorded by the same objective, filtered (Semrock LP03-532RS-25) and analyzed by a spectrometer (Horiba iHR 320, 150 lines/mm) in combination with an electron-multiplied charge-coupled device (Andor Newton 970P EMCCD). In order to acquire hyperspectral maps, the sample stage is scanned relative to the laser spot and a spectrum is measured at each pixel (see figure 4.8 b). The integration time per pixel is 20 ms and the laser power measured in front of the objective is 500 µW.

4.2.4 Kelvin Probe Force Microscopy

Atomic force microscopy (AFM) is widely used to image the topography of nanoscale structures by detecting forces between a scanning probe tip and the sample. KPFM is an extension of this technique, which measures the surface potential, *i.e.* the work function difference between probe tip and sample surface (also called contact potential difference; CPD). In this work, it is employed to investigate the change in gold work function induced by site-selective *SAM* formation on nanoantennas (for more details about *SAMs*, see chapter 3). In order to provide a better understanding, the following section covers the concept of KPFM and outlines experimental details, while corresponding results are presented in chapter 5.

The setup is schematically depicted in figure 4.9 a. A conductive probe tip, *e.g.* a silicon tip with platinum-iridium (Pt/Ir) coating, is slowly scanned over gold structures, while a voltage with DC and AC components is applied to the

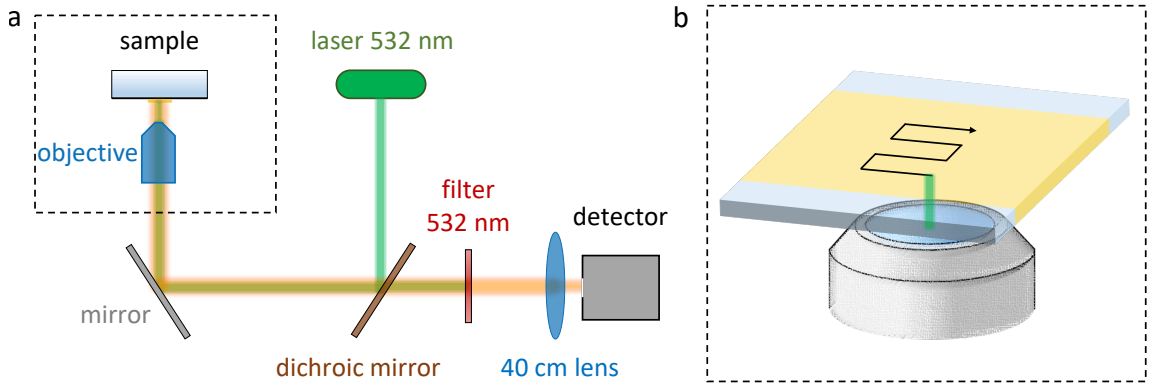

Figure 4.8: Schematic of photoluminescence measurement. (a) A 532 nm laser is focused onto the sample using an air objective. Reflected laser light is blocked by a 532 nm long pass filter and photoluminescence is recorded and analyzed by a detector (spectrometer with EMCCD). (b) In order to record hyperspectral photoluminescence maps, containing a spectrum at each pixel, the sample is scanned relative to the objective (and laser spot) and spectra are acquired continuously.

tip (the sample is grounded). This allows to simultaneously obtain information about topography (AFM) and surface potential (KPFM). Figure 4.9 b illustrates the principle of measuring the surface potential at a specific point of the sample [133]. Tip and sample have different work functions W_T and W_S, respectively. Once in contact, electrons flow from lower to higher work function (*e.g.* from tip to sample) until the corresponding fermi levels $E_{F,T}$ and $E_{F,S}$ align and an electric field builds up, which counteracts the work function difference (the vacuum levels are no longer aligned). This field is defined as

$$U_{CPD} = -\frac{W_T - W_S}{e}, \tag{4.4}$$

where e is the elementary charge. In order to determine U_{CPD}, a voltage with DC and AC components is applied to the tip until the electric field is offset. This field-free point is detected by measuring the associated electrostatic force, which is given by

$$F_{ES}(z) = -\frac{1}{2}U^2\frac{dC(z)}{dz}. \tag{4.5}$$

Here, C is the capacity of the tip-sample system and depends on the distance z (normal to the surface). $U = U_{CPD} + U_{DC} + U_{AC}sin(\omega t)$ is the total potential difference between tip and sample, and not only includes U_{CPD}, but also the applied voltages U_{DC} and U_{AC}. By inserting U into equation 4.5, one obtains a force which consists of three components. In the context of KPFM, the most important component is the frequency dependent force

$$F_\omega = -\frac{dC(z)}{dz}(U_{DC} + U_{CPD})U_{AC}sin(\omega t). \tag{4.6}$$

This force results in oscillating deflections of the probe tip, which can be measured by employing a lock-in amplifier (the applied frequency ω is known). As shown in equation 4.6, F_ω can be nullified by gradually increasing the DC voltage until $U_{DC} = -U_{CPD}$, and once F_ω is zero, the contact potential difference is known [133].

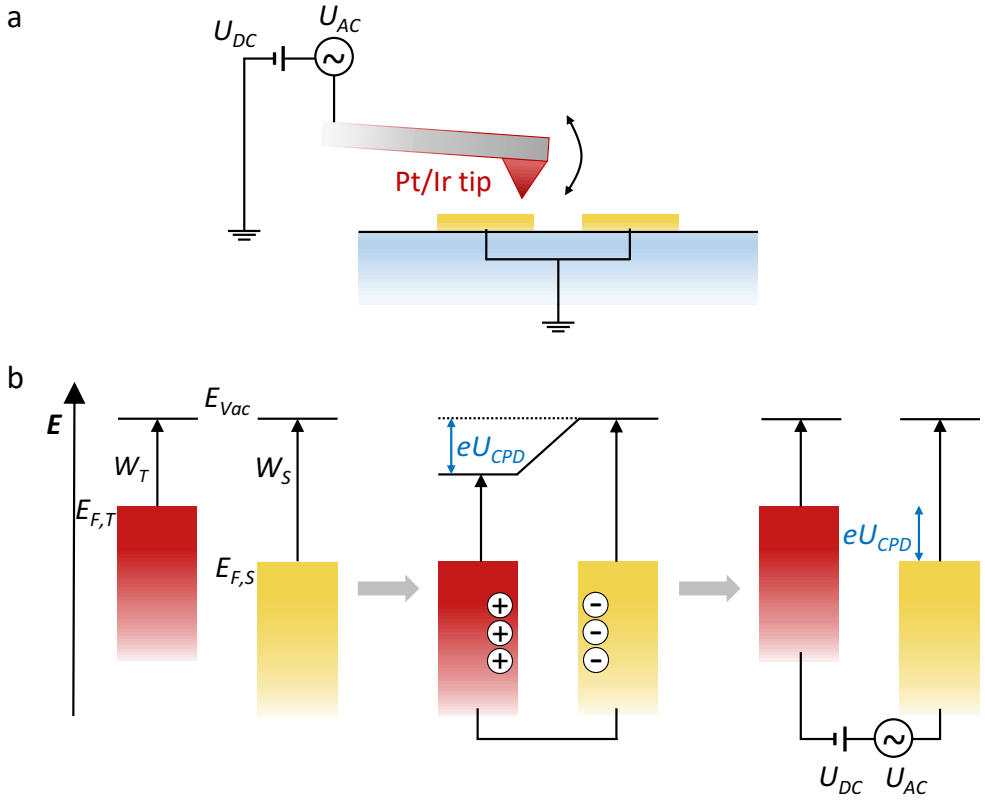

Figure 4.9: Concept of Kelvin probe force microscopy. (a) A *Pt/Ir* coated KPFM probe tip is scanned over the structure (gold) while a voltage with DC component U_{DC} and AC component U_{AC} is applied to the tip. The structure is grounded during the measurement. (b) Tip (red) and structure (gold) have different work functions W_T and W_S, respectively. By connecting the two, electrons flow to the metal with larger work function (*e.g.* the gold structure) until an electric potential U_{CPD} (CPD: contact potential difference) builds up, which compensates the work function difference (see equation 4.4). The value of U_{CPD} is determined by applying U_{AC} and U_{DC} and gradually increasing the latter until the force associated with the electric field is offset. $E_{F,T}$: tip fermi energy; $E_{F,S}$: sample fermi energy.

This technique is also called amplitude modulated KPFM and is used in this thesis. In conclusion, the DC voltage is applied to compensate and determine U_{CPD}, while the AC voltage facilitates the force measurement via lock-in amplifier. Note, that W_S can be obtained, if W_T is known (see equation 4.4). This is achieved by calibrating the measurement with substrates that exhibit well known work functions. However, it is not the goal of this work to measure the true work function, but rather to observe a work function contrast upon site-selective *SAM* functionalization of nanoscale electrodes.

In the measurements presented here, KPFM maps are recorded using a Horiba AIST-NT CombiScope-1000 SPM equipped with PPP-NCHPt conductive probes (Nanosensors; *Pt/Ir* coating, frequency = 330 kHz, radius < 25 nm). Scanning is carried out in tapping mode with scan rates of 0.2 - 0.4 Hz and a lift height of 30 nm. Moreover, all experiments are conducted under ambient conditions and at room temperature.

5 | Site-Selective Functionalization of Nanoantenna Electrodes

Large parts of this chapter are included in a manuscript currently in preparation: *Site-Selective Functionalization of in-plane Nanoelectrode-Antennas* by Maximilian Ochs, Laurent Jucker, Maximilian Rödel, Monika Emmerling, René Kullock, Jens Pflaum, Marcel Mayor and Bert Hecht.

5.1 Introduction

Applying voltages to nano-optical systems can serve a variety of functions ranging from light generation [20, 43, 50] and ultrafast signal modulation [15, 134] to optical rectification [49, 135]. Moreover, as demonstrated in this work, the electrical connection of nanostructures offers new strategies for the assembly of nanoscale devices.

As surfaces become increasingly important at small scales (cf. chapter 3), it is of great interest to tailor the interface properties of nano- and microdevices; either to add chemical functionality or to tune their electronic properties, *e.g.* by modifying the metal work function. Stacked organic optoelectronic devices already make use of different work functions by employing different electrode materials, resulting in efficient charge carrier injection. Lateral electrode arrangements - like those presented in this thesis - can be scaled down to nanometer dimensions and have the advantage to be shaped as optical antennas that radiate light from subwavelength volumes (see section 2.2). However, fabricating lateral nanoscale electrodes with different work functions is rather challenging, yet crucial for further advancing the development of highly efficient optoelectronic nanodevices. Instead of using different electrode materials, in this chapter, I present a technique based on the selective functionalization of gold (*Au* (111)) electrodes with self-assembled monolayers (*SAMs*). By exploiting the electrical connection of optical nanoantennas, the molecule coverage on the individual nanoscale electrodes can be manipulated allowing to tune electronic properties and possibly add new functionalities.

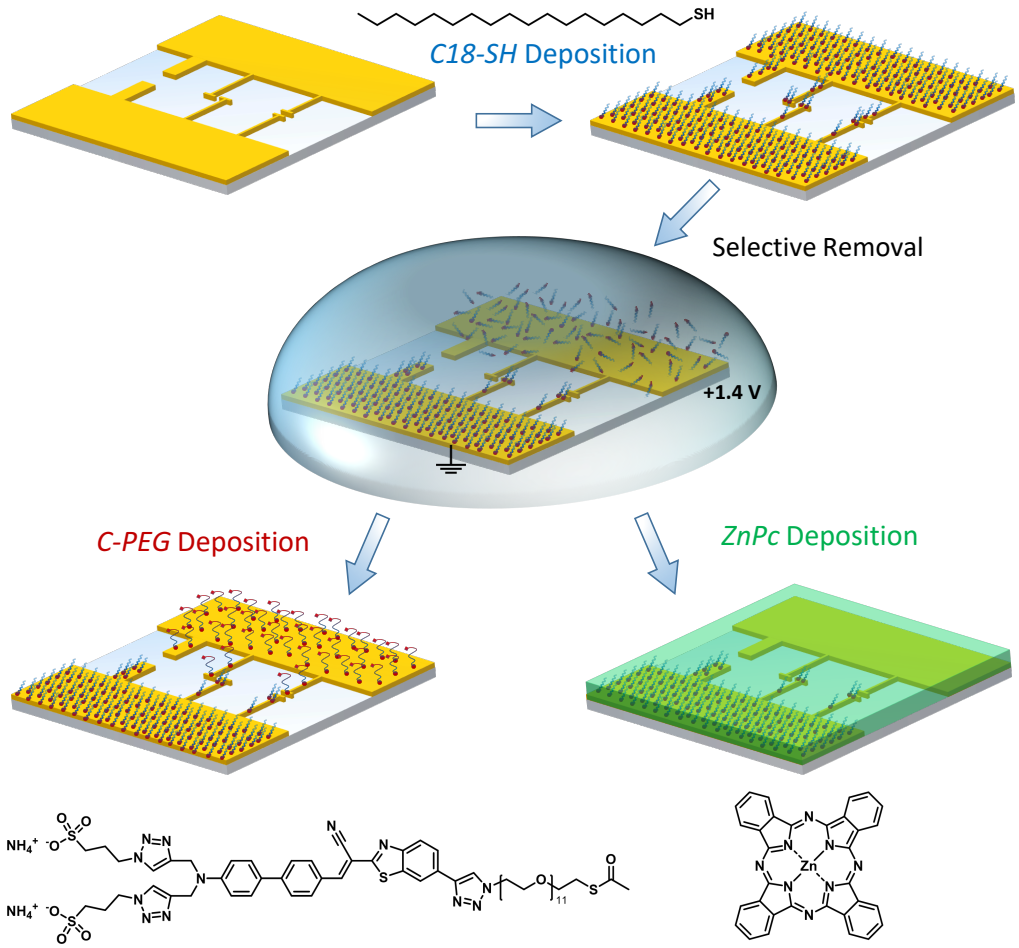

Figure 5.1: Concept of site-selective functionalization. After forming a monolayer of *C18-SH* on the sample, a droplet of electrolyte is applied and molecules are desorbed from the biased electrode via oxidative desorption. Subsequently, a different *SAM*, *e.g.* the chromophore containing *C-PEG*, is deposited on the stripped electrode (see bottom left). The *C18-SH SAM* covering the opposite electrode acts as a blocking layer. Alternatively, an organic semiconductor, here zinc phthalocyanine, is evaporated onto the asymmetrically functionalized electrodes to study interface modifications introduced by *C18-SH* (see bottom right).

Thiolated *SAMs* are extensively studied tools to chemically tailor the surface properties of various metals [101, 103]. A quick introduction to this field is given in chapter 3. Owing to their chemical variability, *SAMs* offer a versatile approach to add new and advanced surface functionalities to nano - and microstructures with possible applications ranging from biochemistry [102] to organic electronics [104]. As discussed in section 3.2, the presence of a *SAM* modifies the work function of the underlying surface. In this context it has been shown that functionalizing metal electrodes with *SAMs* in organic light emitting diodes (OLEDs) and field-effect transistors (OFETs) is a promising

strategy to improve charge carrier injection at metal-organic contact interfaces [104, 118, 136]. In the simple symmetric case, both electrodes are covered by the identical *SAM*, but introducing asymmetry is a common method to further enhance device performance as it selectively promotes the injection of either electrons or holes at the respective contact. In addition, the broad range of functionality offered by *SAMs* paves the road for advanced device concepts based on molecular switches [137] and machines [138, 139].

As the minimum droplet size in *SAM* deposition from liquid phase exceeds the dimensions of up-to-date's nano - and microelectrodes by far, new preparation techniques have to be implemented in order to achieve asymmetric functionalization on such small dimensions. On a comparatively large scale of several hundred micrometers, protective masks [140], microcontact and ink jet printing [102] have been employed for lateral patterning of *SAMs*. Significantly higher resolution is attained by dip-pen lithography (also called nanografting), yet tip-dependent artifacts limit this method to flat substrates [141]. Lithography techniques based on the partial removal of *SAM* molecules include electron beam [142] and ultraviolet photolithography [143], but neither has been used so far to fabricate functional devices. In another approach, molecules are desorbed from laser-excited plasmonic nanostructures via hot-electron mediated gold-sulfur cleavage [52]. While in principle allowing for functionalization at sub-particle resolution, the need for plasmonic resonances and homogeneous illumination limits this technique to small areas of specific device geometries. In addition, a sophisticated laser setup is required.

The electrochemical desorption in a cyclic voltammetry cell offers a much more simple and direct way to remove *SAMs* from gold surfaces [120, 122, 125, 126, 144]. Oxidative as well as reductive desorption have been investigated in the literature and both processes are explained in section 3.3. The reductive desorption is used more frequently, has been extended to coat substrates with different *SAMs* and was scaled down to electrode distances below the optical diffraction limit as verified by Kelvin probe force microscopy (KPFM) [123, 145]. In pursuit of even smaller electronic and optoelectronic devices, however, there exists a great demand for techniques that selectively address individual electrodes of nanoscale extensions and a spacing of only few ten nanometers, while preserving the delicate nature of these structures. Confirming the success of such functionalization with the required nanometer resolution constitutes a further challenge.

Here, an easy-to-use technique for site-selective functionalization of laterally arranged and arbitrarily shaped nanoelectrodes with different types of *SAMs* is demonstrated. As substrates, standard microelectrodes as well as electrically connected optical nanoantennas of different geometries are used [43, 51]. Both are fabricated from single-crystalline $Au(111)$ platelets, as outlined in section 4.1. The procedure is sketched in figure 5.1. Instead of using sophisticated electronic or optical setups, this method is based on oxidative desorp-

tion of thiols in a droplet of electrolyte. Upon applying an electric potential across nanoscale gaps, surface-bound molecules are removed selectively from positively charged electrodes. In contrast to the usually employed reduction where thiol anchoring groups are removed as thiolates, the oxidative removal leads to sulfinates and sulfonates in the presence of oxygen (which is also present in solution). As these oxidized species have a considerably reduced affinity to gold surfaces, this method is less prone to issues and artefacts arising from readsorbed molecules [111, 124, 127]. This is the key feature for site-selective functionalization of nano-sized objects, as already a few readsorbed molecules might have a strong impact on the overall surface properties. By utilizing the steric hindrance imposed by long-chain alkanethiols, such as 1-octadecanethiol (*C18-SH*), a second *SAM* based *e.g.* on a chromophore containing polyethylene glycol (*C-PEG*) is deposited on the stripped/uncovered electrode. In order to verify the successful site-selective functionalization, the surface coverage is mapped by KPFM and photoluminescence measurements (PL; see section 5.2). In a separate section, I demonstrate the tuning of the electronic properties of metal-organic nanodevices by assembling a functionalized hybrid antenna structure covered by the prototypical organic semiconductor zinc phthalocyanine (*ZnPc*; see section 5.3).

Moreover, the presented technique represents a step towards the integration of oriented assemblies of molecular machines into nanoelectrode systems; an idea, which is further discussed in section 5.4.

5.2 Molecular Desorption from Nanoscale Electrodes

This chapter covers the selective desorption of *C18-SH* molecules from nanoscale antenna electrodes monitored by KPFM. Later, the more complex light-emitting *C-PEG* is deposited, and the surface coverage is observed by recording PL maps. In this context, two methods are compared: the direct removal of *C-PEG* based on oxidative desorption and the use of *C18-SH* as a blocking layer.

Figure 5.2 a illustrates the asymmetric functionalization of a plasmonic nanoantenna by site-selective removal of a chemisorbed *SAM*. An SEM image of an exemplary two-arm antenna is shown in figure 5.2 b. The structure consists of a pair of electrically connected antenna electrodes (arms) separated by a 30 nm gap. In a first step, *C18-SH* is deposited from ethanolic solution and thiol groups (*SH*) form covalent bonds with the *Au* (111) electrode surfaces (see subsection 4.1.4). Next, 0.1 mM solution of potassium hydroxide (*KOH*) in n-butanol is drop-casted on the sample and a DC voltage of +1.4 V is applied to the left antenna electrode for 30 s. The *Au-S* bonds on this electrode are consequently broken [120] and the released molecules are rinsed off with ethanol, while the *SAM* covering the opposite antenna electrode remains intact and firmly bond. As desorbed molecules may remain close to the surface [124, 126], the rinsing

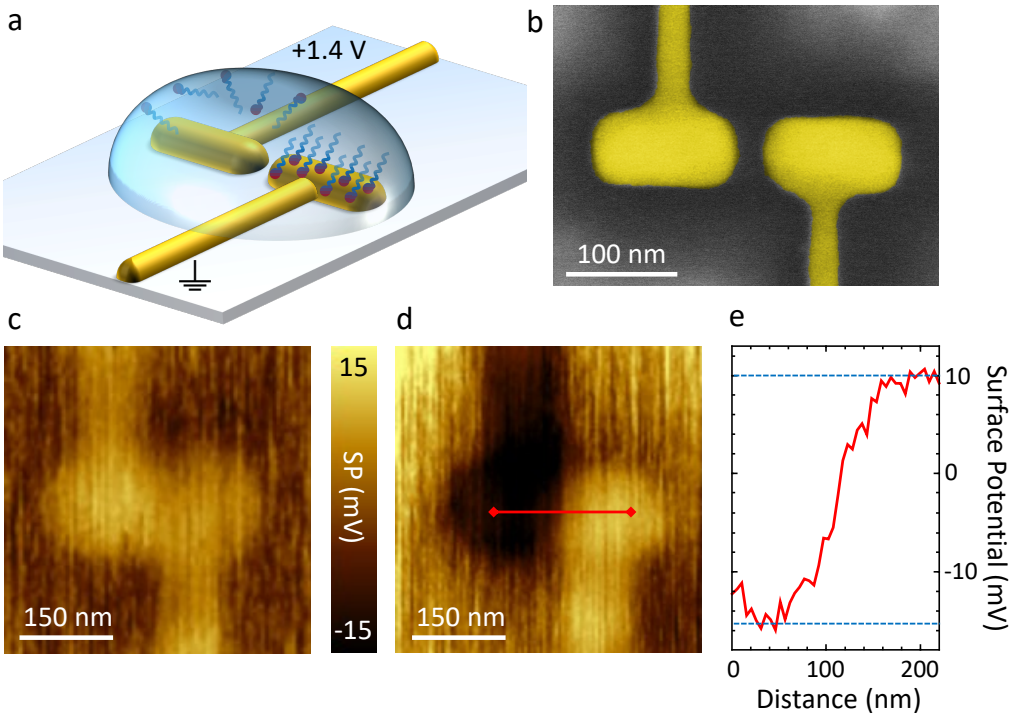

Figure 5.2: Oxidative desorption from nanoscale electrodes. (a) Illustration of molecule removal. An electrically connected nanoantenna is immersed in *KOH*/butanol and one antenna arm is biased at +1.4 V to break *Au-S* bonds. (b) SEM image of an exemplary plasmonic nanoantenna with a gap of 30 nm. (c) and (d) KPFM images of a plasmonic nanoantenna (c) after deposition of *C18-SH* and (d) after selectively removing the *SAM* from the left arm. SP: surface potential. Fast scan direction is bottom to top. (e) Effective surface potential along the red line in (d) showing a difference of 25 mV between the two antenna arms. Dotted blue lines are a guide to the eye.

step is crucial and the solvent should be adjusted to fit the *SAM's* polarity and solubility. The voltage amplitude is a careful trade-off between sufficient desorption and minimum electrode damage. In principle, the voltage can be applied multiple times for 30 s to improve overall molecule removal; however, the associated risk of gold surface oxidation may lead to inferior adsorption of a second *SAM*.

In order to verify the site-selective functionalization at the nanoscale, one can look at the modification of the surface dipole upon adsorption of the *SAM*. This change is dominated by the effective dipole moment of the monolayer with negligible contribution from the *Au-S* interaction which is determined by the strength and orientation of the molecule's dipole moment and the *SAM* density. An altered surface dipole will lead to a shift of the vacuum energy level and, thus, increase or decrease the *Au-SAM* electrode work function, depending on the direction of the *SAM* dipole moment. For example, CH_3-terminated alkanethi-

ols reduce the work function (compared to a pure gold (111) surface), while their CF_3-terminated derivatives lead to the opposite effect [114, 115, 118, 119]. This can be qualified by KPFM, which maps the effective surface potential (SP) - a figure correlated to the work function difference of sample and probe tip [133, 145]. Hence, KPFM allows to measure work function variations induced by different molecule coverage. A short introduction to KPFM is given in subsection 4.2.4 and section 3.2 provides more information about the surface dipole modification induced by *SAMs*.

KPFM images of an antenna before and after site-selective desorption of molecules are shown in figure 5.2 c and d. Both antenna arms have the same effective SP after deposition of a homogeneous *C18-SH SAM*. Upon selective removal from the left antenna arm, KPFM reveals a clear SP contrast of 25 mV between the two electrodes (see figure 5.2 d and e). This indicates that only the right antenna electrode and its connector are still covered by an intact *SAM*. Note, that this shift is far below values measured by ultraviolet-photoelectron spectroscopy in vacuum [116]. This is attributed to the following experimental challenges: (i) The 50 nm diameter of the KPFM probe tip is larger than the antenna gap, and thus the tip collects signal from both antenna electrodes while scanning across the gap. In addition, the cantilever - which is coated with *Pt/Ir* (just like the tip) - also collects SP signals over a larger range. This limits spatial resolution and observable SP contrast. (ii) Imaging is carried out under ambient conditions; hence, a water layer forms on the uncovered gold surface and induces a dipole moment, which is parallel to the *SAM* dipole on the *C18-SH* covered gold surface [146]. (iii) The antenna surface is not perfectly flat after focused ion beam milling, which leads to distortion of the *SAM* in respect of packing and alignment. While the last two points cannot be discriminated in the current setup, probe and sample size related artifacts can be accounted for by calibrating the KPFM measurement.

The corresponding procedure is demonstrated in figure 5.3 at the example of microelectrodes with a spacing of 2 µm. One of the two electrodes is covered with *C18-SH*, while the other electrode was stripped as described before (see figure 5.3 a). During the KPFM measurement, a voltage is applied to the top electrode and gradually increased until the SP contrast disappears. Figure 5.3 b displays the SP measured across both electrodes for different applied voltages. As expected, the SP changes at the top and remains constant at the bottom electrode (which is grounded). The gradual SP plane at the top gold surface is attributed to a slightly inhomogeneous desorption of *C18-SH*. Next, the SP contrast between the electrodes is plotted as a function of applied voltage in figure 5.3 c (error bars account for gradual SP plane). An uncorrected SP contrast of ~100 mV is recorded at zero voltage, but 200 mV need to be applied in order to equalize the SP potentials. The entire analysis results in a correction factor of ~2 and a corrected SP contrast of 200 mV is found for the site-selective functionalization with *C18-SH*. Note again, that this correction only includes probe and sample

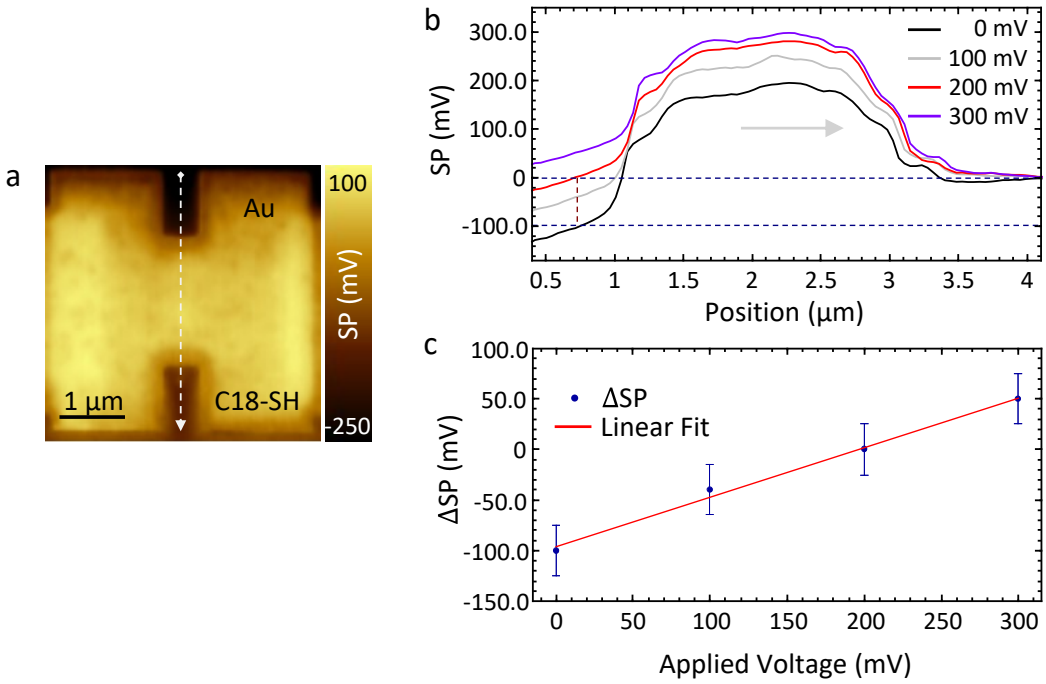

Figure 5.3: KPFM correction. (a) KPFM image of microelectrodes after removing *C18-SH* from the top electrode (surface coverage is denoted). No voltage is applied during this KPFM measurement. (b) Effective surface potential (SP) measured along the white arrow in (a) for different voltages applied to the top electrode (bottom electrode is grounded). SP is normalized to the bottom electrode (covered with *C18-SH*) in all measurements. Dashed lines are used to identify the SP contrast between the electrodes (ΔSP) at 0 mV and 200 mV. (c) ΔSP as a function of applied voltage. Error bars originate from the SP plane at the top electrode (see (b)). A slope of 0.49 is obtained using a linear fit (red) leading to a correction factor of ~2 for the true SP.

size related artifacts. The influences of water layers and non-perfect surface topographies - especially for very small nanostructures - also limit the measurable SP. As feature sizes become smaller than the KPFM probe the uncorrected SP contrast further decreases, *e.g.* see figure 5.2 d and e. Based on the previous correction, the 200 mV are assumed to represent an upper limit for the corrected SP contrast in this experiment - even for nanoantennas. Although, KPFM lacks quantitative value (in this setup), it yields qualitative results and allows to verify the site-selective desorption of *SAM* molecules from nanoscale electrodes.

Next, I demonstrate the applicability of this technique towards more complex molecules. The highly hydrophilic *C-PEG* which combines the well-studied *PEG* chains with a chromophore was chosen for this purpose (the molecule is depicted in figure 5.1). The light-emitting *SAM* offers a fluorescence-based optical feedback from larger microelectrodes, which allows to further corroborate that *SAM* removal is indeed complete. *C-PEG* was designed and synthesized by Laurent

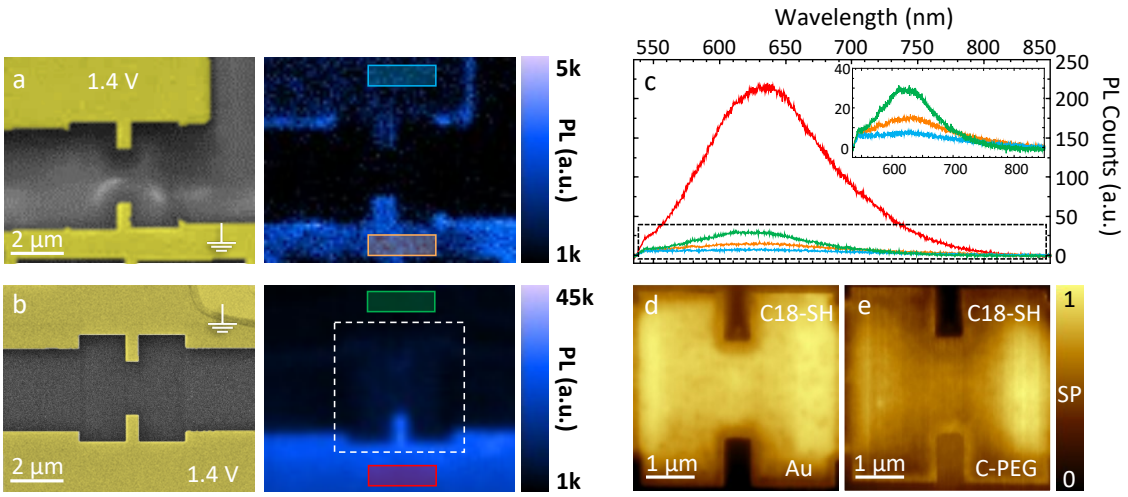

Figure 5.4: Site-selective functionalization with light-emitting *SAM*. (a) and (b), Left: SEM images of two microelectrodes. Right: Hyperspectral PL maps of the same electrodes after site-selective functionalization with light emitting *C-PEG*. Each pixel contains a spectrum, which is integrated to give the total PL counts. (a) Direct desorption of *C-PEG*. Molecules are removed from the top electrode by applying +1.4 V. (b) *C18-SH* as a blocking layer. The structure is first covered with *C18-SH* followed by selectively removing the molecules from the bottom electrode by applying +1.4 V. Next, *C-PEG* is deposited and binds only to the bottom electrode. (c) Average PL spectra of the pixels in the colored rectangles of (a) and (b). The inset shows a zoom into the dashed black rectangle. (d) and (e) Normalized KPFM images of the area marked in (b; white rectangle) taken (d) after site-selective desorption of *C18-SH* and (e) after subsequent deposition of *C-PEG* on the stripped electrode. The surface coverage is denoted.

Jucker (Department of Chemistry, University of Basel), and the *SAM* preparation is outlined in subsection 4.1.4. Long *PEG* chains ensure sufficient emitter-metal distance to minimize quenching once molecules are immobilized on the gold [147], while the dye can be excited at 532 nm and has a broad emission in the red spectral regime close to the antenna resonance.

Figure 5.4 a depicts the direct removal of *C-PEG* from one of two microscopic electrodes milled into a single-crystalline gold (111) platelet. Desorption from the top electrode is carried out as described above, but 0.1 mM *KOH* in water is used to ensure the solubility of *C-PEG*. Next, a hyperspectral PL map is recorded showing almost no light emission from the top surface, while PL is still observed at the bottom electrode. Some molecules remain at the edges of the stripped electrode owing to the large amount of surface defects. In addition, a small unintended desorption from the opposite electrode surface is observed. This is attributed to unstable *SAM* formation of the *PEG* chains, and, hence, solvents with high affinity for the molecules, *e.g.* dimethyl sulfoxide and water can easily remove *SAM* molecules during the washing step (even without ap-

plied voltage). Nevertheless, PL measurements verify that *C-PEG* is removed from specific electrodes upon oxidative desorption.

In order to protect *C-PEG* against any other solvent, the procedure is modified: First, *C18-SH* is deposited on the substrate and selectively removed from one of the electrodes as described before. Next, *C-PEG* is added and mainly binds to the stripped (uncovered) electrode, while *C18-SH* acts as a blocking layer on the other side. As depicted in figure 5.4 b, this method results in a high-quality, unperturbed *SAM* with homogeneous light emission from the bottom electrode. The other electrode, instead, is still covered with *C18-SH*, and thus almost no PL is detected. Figure 5.4 c shows spectra extracted from the two hyperspectral PL maps. Minimal light emission from the surface covered with *C18-SH* is detected (green) as a result of competitive *SAM* formation, but emission from the surface without blocking layer (red) is much stronger and significantly exceeds the one obtained in figure 5.4 a (orange). The spectra collected from all four surfaces share the same shape, thus the PL spectrum is independent of the chosen functionalization procedure. Furthermore, no signs of chromophore degradation - usually accompanied by a spectral shift - are observed in this spectral window. This indicates that the washing step after direct *C-PEG* removal indeed leads to partial desorption of the *SAM* from the opposite electrode (see figure 5.4 a). Next, KPFM maps of a set of microelectrodes are recorded to demonstrate the homogenous coverage of surfaces with molecules. Figure 5.4 d is taken after removing the *C18-SH* blocking layer and depicts the expected uniform contrast between covered and uncovered electrode surfaces. This contrast is reversed upon formation of the subsequent *C-PEG* monolayer (see figure 5.4 e) owing to its strong dipole moment. One can deduce that it is oriented parallel to the dipole moment of *C18-SH* and has a larger absolute value leading to a stronger SP shift [114–116].

According to these results it is concluded that (i) a significant portion of alkanethiol molecules is removed upon oxidative desorption; (ii) the use of a blocking layer is the preferred method for asymmetric functionalization by unstable *SAMs*, which can easily be desorbed from the surface (*e.g.* *C-PEG*) and (iii) the surface is not noticeably oxidized during desorption, because it would hamper the formation of an additional *SAM*.

5.3 Tuning the Current-Voltage Characteristics of Nanoantennas

In this section I demonstrate that the technique introduced above is suitable to selectively modify metal-organic interfaces in a laterally arranged nanodevice. Figure 5.5 a depicts a schematic of the structure as well as an exemplary SEM image. A stack similar to organic light emitting antennas (OLEAs) is employed [51]. After focused ion beam milling, only one of the antenna electrodes is functionalized by *C18-SH* (as described in the previous section) and a 30 nm layer of the organic semiconductor zinc phthalocyanine (*ZnPc*; green) is vacuum deposited on top of the structure. The grains visible in the SEM image are caused by *ZnPc* domains.

The energy diagram for antenna electrodes with and without *C18-SH* is illustrated in figure 5.5 b. Note, *ZnPc* deposited on clean gold (111) surfaces, *e.g.* the stripped antenna electrode, is characterized by preferential hole injection (smaller injection barrier) [51]. As explained in section 3.2, the presence of the *C18-SH SAM* shifts the vacuum energy at the *Au-SAM-ZnPc* boundary and consequently lowers HOMO and LUMO levels of *ZnPc* relative to the metal work function. In contrast, the stripped (uncovered) electrode experiences only a small shift of the vacuum energy due to a weaker interface dipole at the *Au-ZnPc* boundary. Hence, the antenna electrodes exhibit selectively modified injection barriers for electrons and holes. The charge carrier injection can further be influenced by the morphology of *ZnPc*, which is different on a *SAM* covered electrode compared to a pure gold surface [104].

In order to investigate the effect of asymmetric functionalization, current-voltage characteristics of several devices are recorded. In all measurements, functionalized electrodes are grounded and the voltage is applied to the stripped antenna arm (cf. figure 5.5 a). As shown in figure 5.5 c and d, all five devices exhibit asymmetric *IV*-curves, *i.e.* higher currents at positive voltages, which is in line with a reduced injection barrier for electrons and an increased injection barrier for holes at the functionalized antenna electrode. Small current variations for different antennas are attributed to slight deviations at the metal-organic boundaries. As asymmetric *IV*-curves are not expected for symmetrically functionalized or completely unfunctionalized electrodes, this experiment is a further proof that *SAMs* can be selectively desorbed from specific nanoscale electrodes. Moreover, this method allows to tune the electronic, and maybe also structural interface properties of advanced metal-organic nanodevices.

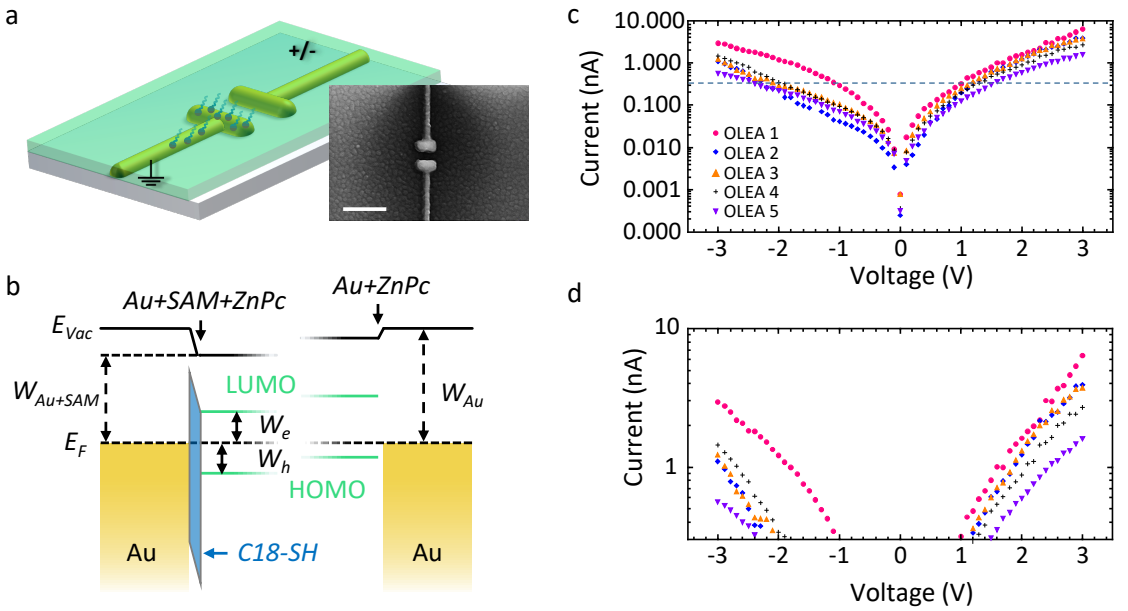

Figure 5.5: Tuning the gold-organic interface. (a) Illustration of metal-organic nanoantenna (OLEA) with asymmetric *SAM* functionalization. *ZnPc* (green) is evaporated, after *C18-SH* is removed from the top electrode. Inset: SEM image of a finalized antenna. The bottom electrode is covered with *C18-SH*. The granular texture stems from *ZnPc* domains. Scale bar; 300 nm. (b) Energy diagram of the two electrodes with (left) and without (right) *C18-SH* monolayer. *ZnPc* evaporated on clean gold exhibits a larger injection barrier for electrons (W_e) than for holes (W_h). The *SAM* introduces an interface dipole, which shifts the vacuum energy level E_{Vac} and lowers the HOMO and LUMO levels relative to the metal work function W_{Au} (identified by the Fermi energy E_F). Thus, injection barriers for electrons and holes are modified. Note, the *Au-ZnPc* boundary also exhibits a small interface dipole. (c) Absolute current as a function of applied voltage for five devices with similar dimensions. Covered electrodes are grounded. (d) Zoom into the region above the dashed line in (c). Higher currents at positive voltages indicate the asymmetric injection behavior at the antenna electrodes.

5.4 Conclusion and Outlook: Towards Supramolecular Motion Controlled by Nanoantennas

In summary, this chapter demonstrated an easy-to-use and straightforward technique for site-selective functionalization of nano - and microelectrodes with different *SAMs*. Instead of relying on complicated optical setups, the technique is based on oxidative desorption of molecules. First, single-crystalline gold (111) surfaces are covered with *C18-SH* or fluorescent *C-PEG* monolayers, and next, a positive voltage of 1.4 V is applied to the target electrode, while the sample is immersed in an electrolyte (0.1 mM *KOH* in butanol or water). The *Au-S* bonds on this electrode are broken and the resulting sulfinates and sulfonates can be washed away easily. Note, that these oxidized compounds have a low affinity to gold surfaces, and thus the probability for readsorption is very low. This is a key advantage over reductive desorption, where the adsorption of previously removed compounds is typically observed [124]. As a result, only one of two laterally arranged nanoantenna electrodes is covered with the respective *SAM*. Moreover, the use of *C18-SH* as a blocking layer was demonstrated. Due to its steric hindrance, a second *SAM* is not forming well on gold surfaces which are already covered with *C18-SH*. This is not only beneficial for *C-PEG* monolayers, which are unstable upon exposure with a highly affine solvent (*e.g.* during direct removal), but also allows to cover neighboring electrodes with completely different *SAMs*. Significant gold oxidation was not observed during the procedure, as it would hinder the subsequent formation of a second *SAM*. The confirmation of selective *SAM* functionalization was a further challenge - especially for electrodes with nanoscale distances. While the homogeneous desorption from larger microelectrodes was verified by recording the PL of light-emitting molecules, KPFM was used for nanoelectrodes with gap sizes of 30 nm. Even though a correction procedure for KPFM was introduced, the results should rather be seen as a qualitative confirmation of site-selective functionalization.

By making use of the manifold properties of *SAMs* an extra degree of freedom is added to the design and development of laterally arranged nano-optical systems. In order to demonstrate the potential for future nano-optoelectronic devices, metal-organic nanoantennas were assembled, in which only one electrode was covered by *C18-SH*. As a consequence, the electrode work functions and thus the charge injection barriers were selectively modified, resulting in asymmetric *IV* - curves.

In future experiments, the diversity of *SAMs* will further add to the amount of possible functionalities. By using *SAMs* with tailored dipole moments and even photoswitchable components [108, 137, 148] the precise engineering of structural as well as electronic interface properties of nanoscale objects seems feasible. Furthermore, site-selective functionalization enables oriented assemblies of molecular machines between laterally arranged metallic nanoelectrodes. In

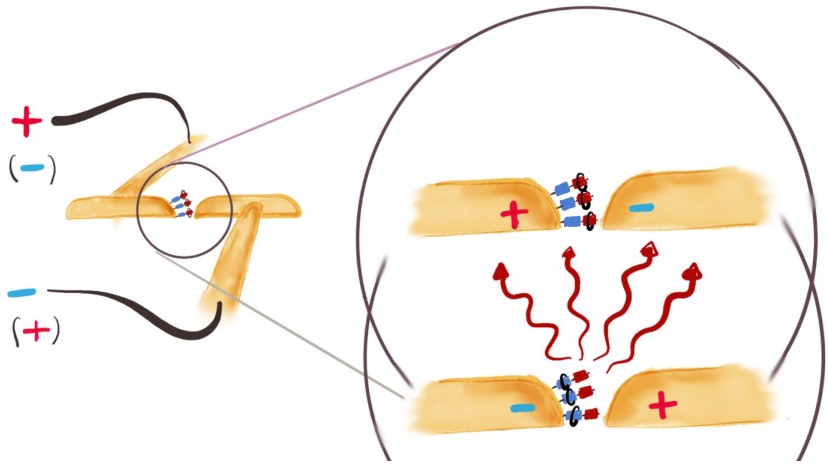

Figure 5.6: Towards supramolecular machinery controlled by nanoantennas. Only one electrode of a two-arm antenna is covered with a rotaxane, *i.e.* a molecular superstructure consisting of a charged macrocycle (black ring) that can move along a molecular rod (blue box). This rod is equipped with a chromophore (red box) that can be quenched by the macrocycle. Upon applying a voltage, an electric field is created in the antenna gap and the macrocycle is moved in a specific direction. If it is close to the chromophore, light emission is suppressed. But if it moves away from the chromophore, light is emitted (optical excitation necessary). Due to the strong field enhancement in the feed gap, the emission will be dominated by rotaxanes in the antenna gap (although the entire left electrode is covered with molecules). Site-selective functionalization is necessary in order to obtain rotaxane assemblies with clearly defined orientation.

fact, the developed method represents a step towards supramolecular translation controlled by optical nanoantennas.

Figure 5.6 illustrates a possible experiment in which only one electrode of a two-arm antenna is covered by a specifically designed rotaxane. This fascinating system takes advantage of the previously described site-selective functionalization, the laterally arranged nanoantenna electrodes as well as the high field enhancement offered by nano-optical structures. The rotaxane consists of a charged macrocycle (ring-like moiety) moving along a molecular axle (rod-like moiety, *e.g.* *PEG* chain). The latter incorporates a chromophore, whose light emission depends on the position of the macrocycle. In this example, the emission is quenched by charge-transfer effects if the ring is located above the chromophore, but if the ring moves away, light is radiated. Note, that depending on the exact chromophore, the reverse case is also possible, *i.e.* the emission could be enhanced by the macrocycle [149, 150]. By applying a voltage to the antenna, an electric field is created in the gap, which is strong enough to drive the translational motion of charged macrocycles along their molecular axles. This movement is then monitored by recording the light emission of the integrated chromophores. I want to emphasize that site-selective functionalization is a key

aspect in this experiment. As sketched, the remaining rotaxanes form oriented assemblies within the feed gap, and thus the movement of the macrocycle relative to the chromophore is clearly defined. The antenna has two functions: it controls the supramolecular translation and facilitates the read-out by enhancing the emission of the chromophores. Therefore, the antenna resonance needs to be adjusted to the dye. In this case, the emission intensity is dominated by rotaxanes in the vicinity of the feed gap as they experience the highest field enhancement. For this reason, only the molecules close to the gap are displayed in figure 5.6, but in principle the entire left electrode is covered.

However, there are still a few challenges to be overcome. The shortest possible resonance wavelength of the antenna is limited by the properties of gold and lies around 600 nm [3]. Synthesizing a suitable chromophore that emits red light and is still compatible in size with the macrocycle is particularly challenging (preliminary results are presented in references [149–151]). The antenna resonance can in principle be shifted to the green regime by using silver instead of gold allowing to employ "simpler" green chromophores. Notably, the growth of large single-crystalline silver platelets has been demonstrated [152, 153], which means that high quality silver antennas can be fabricated. A protection layer is usually applied [154], since silver is chemically less stable than gold; however, this is not suitable for the proposed experiment, because thiolated molecules need to bind directly to the metal. Nevertheless, the fabrication of silver antennas is currently being investigated in our research group. The exact configuration of the molecular superstructure on the antenna surface is another open question. It will be interesting to see if rotaxanes carry out translational motion in air (in the presence of water layers on the gold surface) or if they require additional solvent. In the latter case, it should be noted that *C-PEG* monolayers - a potential basis for the rotaxanes - are degraded upon exposure to a highly affine solvent.

The current work lays a foundation for the proposed experiment - especially the established site-selective functionalization is a key aspect - and I am confident that the remaining challenges can be overcome. Even though highly ambitious, this measurement promises fascinating insights into the motion of rotaxanes and might establish an interface between molecular machinery and nanoscale optoelectronic devices, which is so far unprecedented.

6 | Electrically Driven Optical Yagi-Uda Antennas

Large parts of this chapter are published in *Electrically-driven Yagi-Uda antennas for light* by René Kullock, Maximilian Ochs, Philipp Grimm, Monika Emmerling and Bert Hecht. Nature Communications **2020**, 11, 115. doi.org/10.1038/s41467-019-14011-6

6.1 Introduction

Radio frequency (RF) antennas - linking propagating electromagnetic waves with electric currents in metals and integrated circuits - are the key components of wireless communication; hence, they are integral parts of all mobile devices, such as smartphones and laptops. The resonance frequency of simple dipole antennas scales with size, so that smaller structures are resonant at higher frequencies. This means, that shrinking antennas to the nanoscale not only decreases their footprint, but also leads to much higher resonance frequencies in the optical regime, which in principle enables higher transmission bandwidths (see subsection 2.2.1). With advances in fabrication technology, first antennas for light were developed almost two decades ago [30]. However, these simple nano-optical systems are limited to purely optical excitations and most experiments aim at enhancing light-matter interaction [14, 32–35, 132, 155]. Later, Kern *et al.* developed the first optical antenna, electrically driven by inelastic electron tunneling (IET) [20]. This structure, although a major step towards chip-integrated nanoantennas, is not suitable for point-to-point communication, as it radiates light with a dipolar emission pattern (see subsection 2.2.2). Hence, optical antennas of the next generation not only need to generate light locally, but efficiently radiate it into a specific direction.

In the radio wave regime, Yagi-Uda antennas are well known for efficient point-to-point transmission and reception of information, having played an important role in establishing television broadcasting [55]. Their large directionality originates from interference effects within a sophisticated antenna geometry comprising a reflector, an active feed element and multiple directors.

A detailed description of the working principle is provided in subsection 2.2.3. Miniaturizing the Yagi-Uda concept from the RF to the optical regime promises high-bandwidth data transfer on very small dimensions; the devices exhibit wavelength-scale footprints and could represent a link between electron-based integrated computer chips and photon-based fiber networks in the future. As such antennas outperform subwavelength waveguides for longer distances [27], enable multiple beam crossings and are not restricted by Joule heating [156], they are particularly interesting for on-chip optical data communication.

Although a considerable amount of work was put into the development of optical Yagi-Uda antennas, starting with the optimization of design parameters [77] to the fabrication of different in-plane antennas [38, 40, 157–159], all these experimental demonstrations relied on external optical excitations using bulky lab-scale setups. The electrical and local generation of light - a prerequisite for chip-integrated antennas - was still missing. For this purpose, multiple approaches have been investigated, *e.g.* light emission in carbon nanotube junctions [65–67] or feeding nanoantennas with perfectly matched transmission lines [64]. Yet, as discussed before, IET has been established as the most common method to electrically drive optical antennas [43, 47, 50]. So far, directed emission in such a configuration has been achieved by twisting the arms of electrically driven dipole antennas in order to break the point symmetry [46]. This structure - it is not a Yagi-Uda antenna - exhibits only limited geometrical definition and directionality. Furthermore, it is by design not scalable to significantly higher values, and thus, not suitable for cross-talk free on-chip optical data communication. Key breakthroughs in antenna design, quality and fabrication are still needed to achieve the same performance, versatility and usability as classical RF antennas.

This work significantly advances the state of the art of optical antennas. In this chapter, I present in-plane electrically driven optical Yagi-Uda antennas, which generate light locally via IET and radiate it in a specific direction due to their refined geometries. The structure design is discussed in section 7.2. Particular challenges include the accurate fabrication of nanostructures along with the exact positioning of delicate connection wires - which is solved by employing focused ion beam milling (FIB) of single-crystalline gold platelets - and the preparation of 1 nm gaps for electron tunneling. Tunnel junctions are fabricated reproducibly via feedback-controlled dielectrophoresis (DEP), whereby single surface-passivated gold nanoparticles are placed in the antenna feed gap (see section 6.3). I experimentally show that optical Yagi-Uda antennas have unprecedented forward-to-backward (FB) ratios of up to 9.1 dB and are scalable up to 15 elements resulting in 13.2 dB (see section 6.4). Simulations further suggest that hybrid systems consisting of antennas embedded in high-index films can even outperform conventional RF Yagi-Uda antennas. This work is thus a major step towards on-chip optical antenna communication. Remaining challenges as well as the next development steps are discussed in section 7.4.

6.2 Structure Design

The exact device geometry has been found in an iterative process consisting of simulations and experimental characterizations. Philipp Grimm carried out the former, employing analytical and numerical models to optimize the directionality of the antenna. The Yagi-Uda concept as well as the modelling are discussed in subsection 2.2.3, for more information see references [20, 74]. Here, I quickly present the optimized antenna geometry.

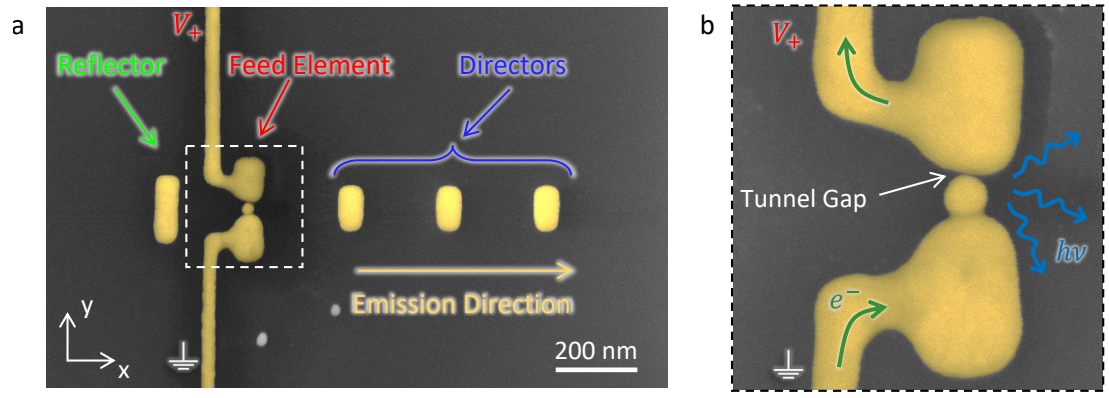

Figure 6.1: Electrically driven optical Yagi-Uda antenna. (a) SEM image of an antenna exhibiting one reflector, three directors and a feed element. The structure is connected to two external electrodes via kinked connectors. As opposed to RF antennas, this optical antenna is not free-standing, but lies on a glass substrate. (b) Zoom to the feed element. The feed gap is filled with a 30 nm gold particle, which is connected to the bottom antenna arm, thus creating a tunnel junction towards the top arm. Upon applying a voltage V_+, electrons (e^-) tunnel inelastically and photons ($h\nu$) are emitted. The emission direction is denoted in (a). Adapted from reference [20].

Figure 6.1 depicts SEM images of an exemplary electrically driven Yagi-Uda antenna for light. The structure consists of one reflector, an electrically connected feed element and three directors. According to simulations, a maximum FB ratio is obtained at a driving frequency of 850 nm and reflector and director resonances at 890 nm and 680 nm, respectively (see also figure 2.10 b). The reflector is placed 200 nm away from the feed element. This spacing is slightly larger than the optimal values obtained from simulations, but ensures that reflector, connectors and feed are not too close and can be fabricated accurately. The length of individual elements is used to tune the associated resonances, while the width is set to a minimum of 60 nm. A director spacing of ~130 nm or ~240 nm yields the largest directionality, but for practical reasons, the latter spacing is chosen for the experiments. The exact dimensions are listed in table 6.1. Note, that the FB ratio is very sensitive to small deviations from these values, and thus, the fabrication is very demanding. To ensure the required

Parameter		Dimension (Experiment)
Gold Platelet	Height	40 nm
Connector	Width	30 nm
	Spacing	100 nm
Reflector	Length	166 nm
	Width	60 nm
	Spacing	200 nm
Feed	Length	115 nm (each arm)
	Width	80 nm
	Gap	25-30 nm
Director	Length	108 nm
	Width	60 nm
	Spacing	240 nm
Particle	Diameter	30 nm

Table 6.1: Optimized geometric dimensions of five-element optical Yagi-Uda antennas.

accuracy, highly precise gallium FIB milling of single-crystalline gold platelets is employed and carried out as outlined in section 4.1. As thinner platelets allow finer cuts, platelets with a thickness of 30 - 40 nm are chosen.

The heart of the antenna is the feed element, which resembles the two-arm dipole antenna introduced in subsection 2.2.1 (see figure 6.1 b). It is electrically connected via FDTD-optimized kinked connection wires without disturbing the feed resonance [42]. As both wires are attached from the same side, the connectors act as an additional reflector, which even increases the directionality (not shown here; see reference [20] for more information). Light is generated via IET and the necessary tunnel junction is created by placing a single *CTAB* passivated 30 nm gold particle into the prefabricated feed gap. In the example shown in figure 6.1 b, the particle is in contact with the bottom antenna arm, resulting in a tunnel gap between top antenna arm and particle (facilitated by the *CTAB* shell). By applying a voltage, electrons tunnel across this barrier - a process, which can be elastic or inelastic. In the latter case, the electrons lose energy and photons are emitted (see subsection 2.2.2). Subsequently, the feed element excites the passive reflector and director elements leading to constructive interference in forward and destructive interference in backward direction (the emission direction is denoted in figure 6.1 a). Note, the entire antenna is situated on a glass substrate and light emission is detected via an oil-immersion objective from below. Due to the higher refractive index of glass, light is not ra-

diated in-plane, but propagates into the glass under the critical angle.

Now that the structure design is established, the next section presents the fabrication of tunnel junctions via feedback-controlled DEP.

6.3 Feedback-Controlled Dielectrophoresis

Although DEP offers advantages over the previously employed drop-and-push approach via atomic force microscopy [43], mainly its ease of implementation, scalability as well as applicability to complex geometries, a feedback is required to stop the attraction of particles once the gap is loaded. Here, I focus on such a feedback system, which was specifically developed for optical antennas, while working principle and experimental setup of DEP are presented in subsection 4.1.3. Note, the method is presented for two-arm antennas, but is applicable to any electrically connected nano-optical system, which exhibits strong far-field scattering, *e.g.* optical Yagi-Uda antennas.

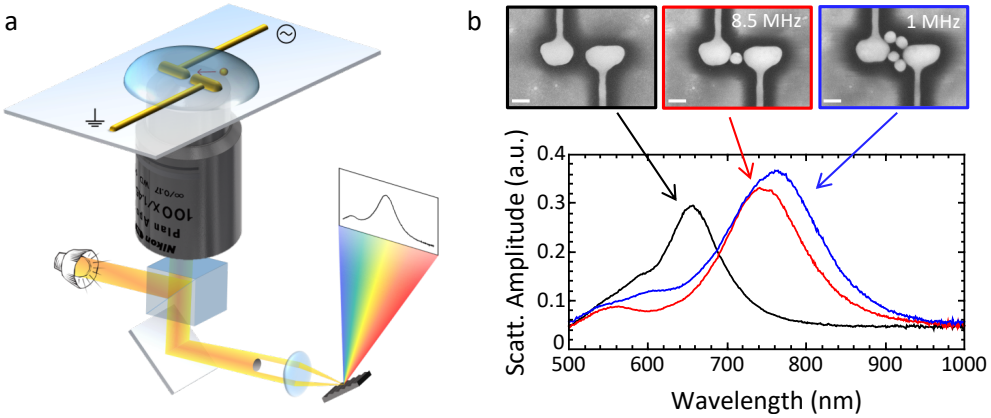

Figure 6.2: Feedback-controlled dielectrophoresis. (a) Schematics of the setup (see subsection 4.2.1 for more information about the measurement). The antenna (*e.g.* a two-arm antenna), immersed in a particle containing water droplet, is excited with white light and scattering spectra are continuously acquired in real-time, while an AC voltage is applied. Due to the DEP force, a particle moves into the feed gap. (b) White-light dark-field scattering spectra and corresponding SEM images of two-arm antennas: before DEP (black), after applying 8.5 MHz (red; same structure; 3 V) and after applying 1 MHz (blue; 2 V). The presence of a particle significantly redshifts the spectrum, which is used as feedback. As soon as this spectral shift is detected, the voltage is turned off. The optimal frequency for single-particle attraction is 8.5 MHz in this case, while too many particles are attracted at low frequencies such as 1 MHz. A stronger redshift as well as a spectral broadening are typical signs of multiple-particle attraction. Scale bars; 50 nm. Adapted from reference [20].

Figure 6.2 a illustrates the procedure for feedback-controlled DEP. The sample is mounted on a Nikon TE2000-U inverted microscope and a water droplet containing gold particles is placed on top of the antenna (practically the entire gold platelet). One of the two antenna electrodes is grounded, while an AC voltage is applied to the other electrode. Depending on voltage and frequency, particles are then attracted to regions of the highest field gradient, *i.e.* the feed gap, due to the dielectrophoretic force. In order to ensure that exactly one particle is placed into the antenna gap, the white-light scattering spectrum of the antenna is continuously monitored at a 10 Hz repetition rate. Exemplary spectra before and after DEP as well as the corresponding antennas are shown in figure 6.2 b. The empty structure has a resonance at around 660 nm before DEP (black). By applying 8.5 MHz (3 V), a particle moves into the feed gap, which decreases the gap size from ∼30 nm to 1 nm (red), and consequently redshifts the antenna resonance by almost 80 nm (cf. figure 2.5). Once this happens, the voltage is turned off immediately to prevent the attraction of even more particles. However, if the frequency is too low, *e.g.* 1 MHz (2 V), the dielectrophoretic force is large and multiple particles are attracted before the DEP is stopped (see figure 4.4). This case can be identified *in-situ* as the presence of many particles in and around the antenna typically leads to a stronger redshift as well as a spectral broadening (blue). Thus, the DEP frequency plays a critical role, and it must be optimized for each structure geometry and for a given particle concentration. Detailed frequency tests as well as simulations of the DEP procedure are presented in references [20, 74]. For two-arm antennas, 8.5 MHz is ideal, but larger frequencies of 12 MHz and 15 MHz need to be applied for Yagi-Uda antennas and plasmonic waveguides, respectively (see chapter 7). The voltage, on the other hand, is usually increased gradually. In a typical experiment, a voltage with specific frequency and low amplitude (*e.g.* 1 V) is applied for one minute. If no redshift is observed, the voltage is slightly increased and again applied for one minute. This process is repeated until the resonance redshifts and the gap is filled. Note, a maximum voltage of 5 V is chosen to avoid structural damage to the antenna.

After optimal settings were found, DEP is performed for 27 two-arm and 39 Yagi-Uda antennas, and the results are depicted in figure 6.3. The success rate, *i.e.* one particle is inside the gap, was 56 % for two-arm antennas and dropped slightly to 44 % for the more complex Yagi-Uda design. Overall, single particle attraction was the most common event with 48.5 %. 15 structures (22.7 %) remained empty after reaching the voltage limit and applying 5 V for 60 s. This event is more favorable than attracting multiple particles (28.8 %), because empty antennas can be reused and filled in an additional DEP experiment with a new particle solution.

In conclusion, the feedback system allows to carefully increase the voltage until a redshift is observed, which significantly reduces the attraction of multiple particles and leads to a high success rate. Importantly, single particles inside

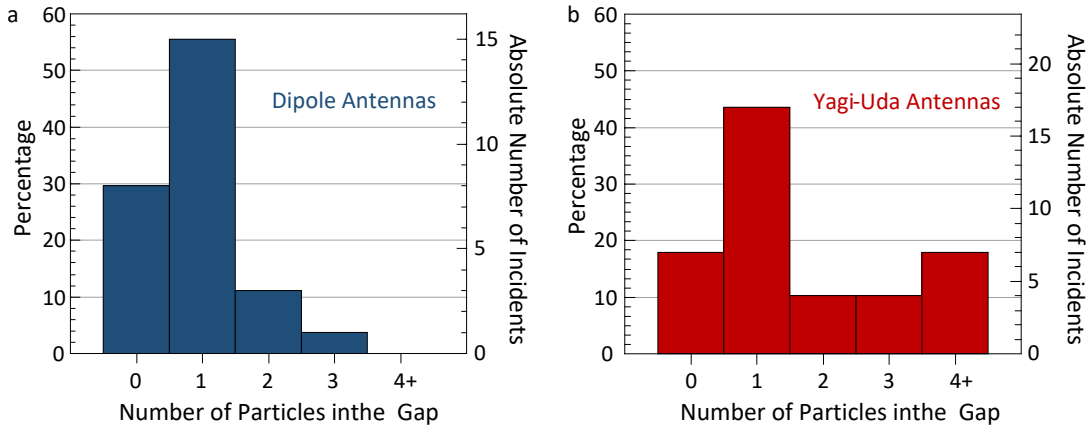

Figure 6.3: Statistics of dielectrophoresis with optimized parameters. Number of incidents for (a) 27 dipole (two-arm) antennas and (b) 39 Yagi-Uda antennas. Overall, the likelihood of having a single particle inside the gap was above 48 %. Antennas, which were not filled by the first run of DEP, were reused. Adapted from reference [20].

the gaps result almost always in light emission based on inelastic electron tunneling; reasonable electroluminescence spectra were recorded in 78 % of these cases.

6.4 Performance and Limits of Optical Yagi-Uda Antennas

This section is devoted to the experimental characterization of optical Yagi-Uda antennas including white-light dark-field scattering (WL) and electroluminescence (EL) measurements (see section 4.2 for measurement details). Particular emphasis is given to the directionality of antennas, with the FB ratio being the key performance metric. Moreover, optical antennas are compared to their RF counterparts and limits as well as possible improvements to the antenna design are discussed on the basis of simulations.

As mentioned in section 7.2, optimizing the geometry is done by iterating simulations and experiments. This includes WL measurements of individual elements (reflector, feed, director) and complete Yagi-Uda antennas to identify their resonance positions and make adjustments. In figure 6.4 a, scattering spectra of optimized elements as well as a fully assembled antenna are shown; corresponding SEM images are displayed in figure 6.4 c-f. The spectra nicely resemble the pattern presented in figure 2.10 b. As intended, the resonance positions of the reflector and directors occur at 890 nm and 680 nm, respectively, while the Yagi-Uda antenna and its loaded feed element are resonant around 820 nm (see section 7.2). Although the target was 850 nm, the feed resonance is nicely positioned, because the driving frequency, *i.e.* the emission wavelength,

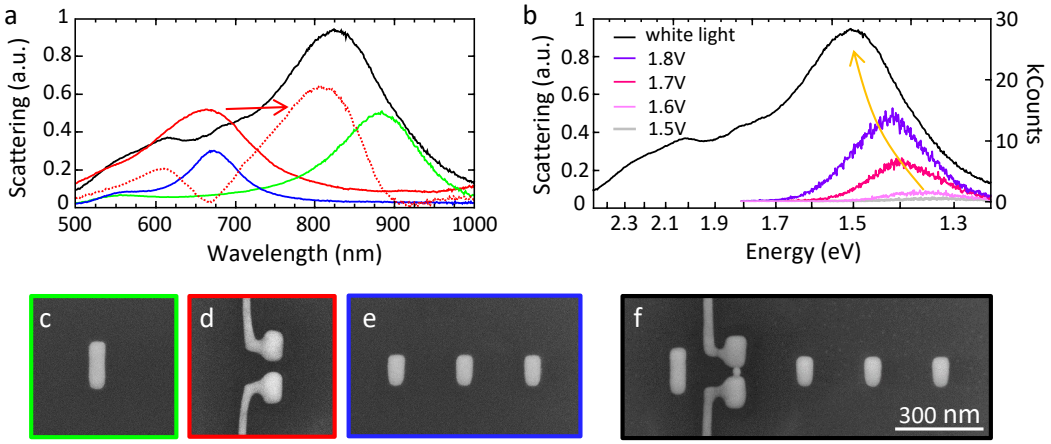

Figure 6.4: Characterization of optical Yagi-Uda antennas. (a) White light dark-field scattering spectra of optimized antenna elements (green: reflector; red: unloaded feed element; blue: three directors) and complete Yagi-Uda antenna (black). The dotted red line corresponds to the loaded feed within the complete Yagi-Uda antenna. It is calculated by substracting the spectra of reflector and director elements from the complete Yagi-Uda spectrum. (b) Electroluminescence spectra of the same Yagi-Uda antenna for different applied voltages together with the scattering spectrum. As the voltage increases, the intensity becomes stronger and shifts to the blue. The voltage drop-off is close to zero. (c)–(f) Associated SEM images. Taken from reference [20].

is on the red side of this resonance. This becomes clear by considering the EL spectra of the Yagi-Uda antenna. Note, the redshift of the feed resonance upon loading the gap depends on the exact particle position, and is thus difficult to predict [43]. In order to achieve large directionalities, the (loaded) feed resonance must be located between reflector and director, and - due to the uncertain resonance position of the feed after DEP - the spectral window spanned by the passive elements is chosen to be especially large (210 nm). For comparison, an unloaded feed is depicted in figure 6.4 and the resonance of the loaded feed (same dimensions, with particle) within the Yagi-Uda antenna is estimated by subtracting the passive elements from the Yagi-Uda spectrum.

EL spectra of the same Yagi-Uda antenna are depicted in figure 6.4 b. Upon applying a DC voltage, light is emitted based on inelastic electron tunneling and, as predicted by the quantum shot noise model (cf. figure 2.8), the emission peak blueshifts with increasing voltage. The quantum efficiency, *i.e.* the number of emitted photons per tunneling event (calculated from total measured current), is on the order of 10^{-5} to 10^{-4}, which is comparable to previous results in similar structures [43]. To prevent destruction of the antenna, the applied voltage is limited to 1.8 V in this case, resulting in an emission maximum around 870 nm that is close to the ideal driving wavelength of 850 nm. The voltage drop-off, *i.e.*

the difference between applied voltage and maximum emitted energy, is almost zero, which indicates that a single tunnel barrier is present. Note, the emission wavelength is correlated to the used material (gold) and was chosen to achieve large FB ratios. Yet, the antenna could be adapted to emit visible light by using *e.g.* silver as the base material.

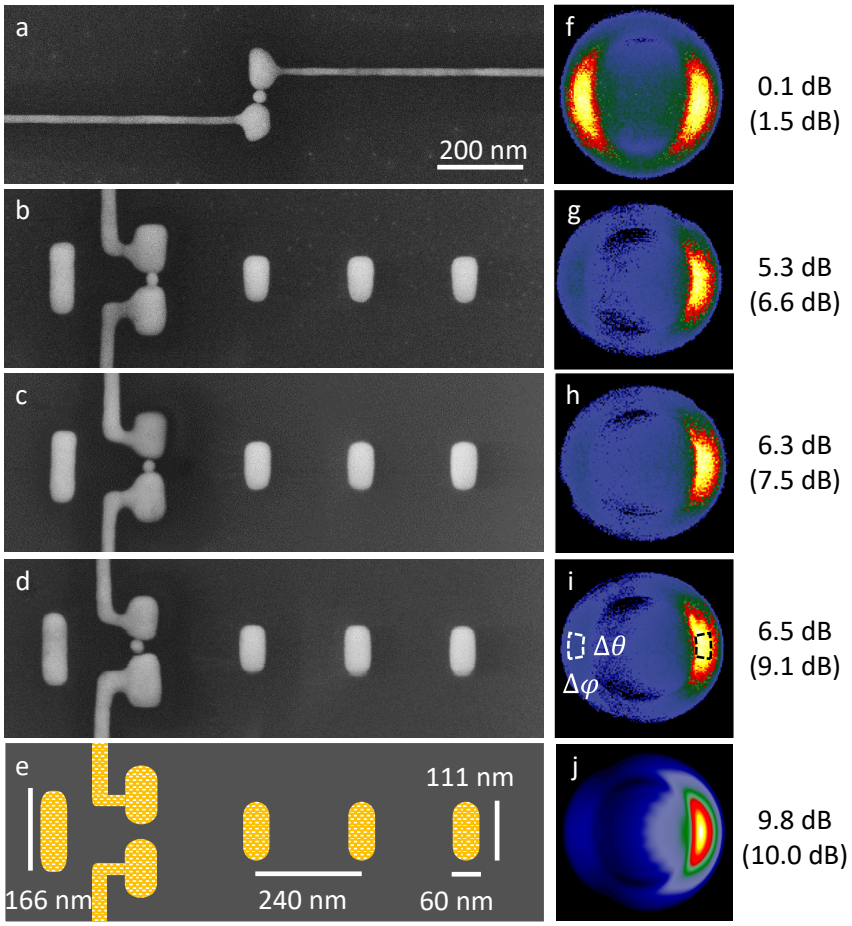

Figure 6.5: Directionality of dipole and Yagi-Uda antennas. (a)-(d) SEM images of one dipole (two-arm) and three Yagi-Uda antennas. (e) Sketch of the FDTD model. (f)–(j) Corresponding emission pattern. While the dipole antenna emits in forward (right) and backward direction, the Yagi-Uda antennas show a high directionality to the right. The resulting FB ratios determined by the areal (pixel) method are given. Integration areas ($\Delta\varphi = 20\,°$, $\Delta\theta = 15\,°$) are indicated in (i). Simulations were carried out by Philipp Grimm. Taken from reference [20].

Next, the directionality is investigated by measuring the EL emission pattern (see subsection 4.2.2). The results as well as corresponding SEM images of multiple structures are presented in figure 6.5. To evaluate the device performance and compare it to the literature, the FB ratio is calculated according

to equation 2.18. Intensities are extracted in two different ways: The "pixel" method was first introduced by Curto *et al.* [40] and simply divides the intensities of the brightest pixel in forward and its opposite pixel (not necessarily the darkest) in backward direction. Although well established in previous publications, this method is prone to errors as it is only based on two pixels and noise in the "darker" backward direction leads to large FB ratio fluctuations. For these experiments, an error of ± 1.4 dB is estimated based on emission measurements of dipole antennas. More accurate results are obtained with the "areal" method introduced by Gurunarayanan *et al.* [46], in which the emission pattern is integrated over fixed solid angle sections in forward and backward direction, and the resulting intensities are divided. This method leads to smaller FB ratios and an error of ± 0.2 dB is estimated (uncertain emission pattern size). Note, however, that the calculated values depend on the size of the solid angle sections and, for comparison, the same interval size as in reference [46] is used ($\Delta\varphi = 20\,°$, $\Delta\theta = 15\,°$; indicated in figure 6.5 i).

As a reference, a two-arm antenna is investigated, which emits two lobes perpendicular to the long axis (see figure 6.5 a and f). For this dipole-like structure one expects FB ratios of 0 dB, and indeed, values of 1.5 ± 1.4 dB and 0.1 ± 0.2 dB are calculated with the pixel and areal method, respectively. This emission pattern is in agreement with previously fabricated antennas (see figure 2.9) [43]. Next, the focus shifts to Yagi-Uda antennas. The first structure is the one discussed in figure 6.4 and exhibits a directionality of 6.6 dB or 5.3 dB (see figure 6.5 b and g), which is already larger than the maximum of 6 dB (pixel method) measured by Curto *et al.* for optically driven Yagi-Uda antennas [40] as well as the 5 dB (areal method) obtained by Gurunarayanan *et al.* with their twisted antenna approach [46]. Even better performance is achieved by the two remaining Yagi-Uda antennas shown in figure 6.5 c,h and d,i (note, the former is the same antenna as in figure 6.1). FB ratios of up to 9.1 dB (pixel method) or 6.5 dB (areal method) are reached, demonstrating that the high-quality optical Yagi-Uda antennas presented in this work clearly outperform all hitherto published approaches. Variations between antennas are attributed to slight geometrical deviations as well as particle placement. Furthermore, the results are in good agreement with the FDTD calculations displayed in figure 6.5 e and j, which indicate a limit of 10 dB for this design.

A common strategy to further enhance directionality in the RF regime is the addition of more directors [160]. Accordingly, an optical 15 element Yagi-Uda antenna (13 directors) is fabricated as described before and an SEM image as well as the measured emission pattern are shown in figure 6.6 a. Although light emission is detected, FB ratios are surprisingly low with only 3.1 dB (pixel method). In general, it is observed that the directionality decreases when antennas are equipped with more than three directors. This behaviour is explained by the antenna's air-glass surrounding in the experiment. Due to the higher refractive index of glass, the emitted light is refracted into the substrate, and

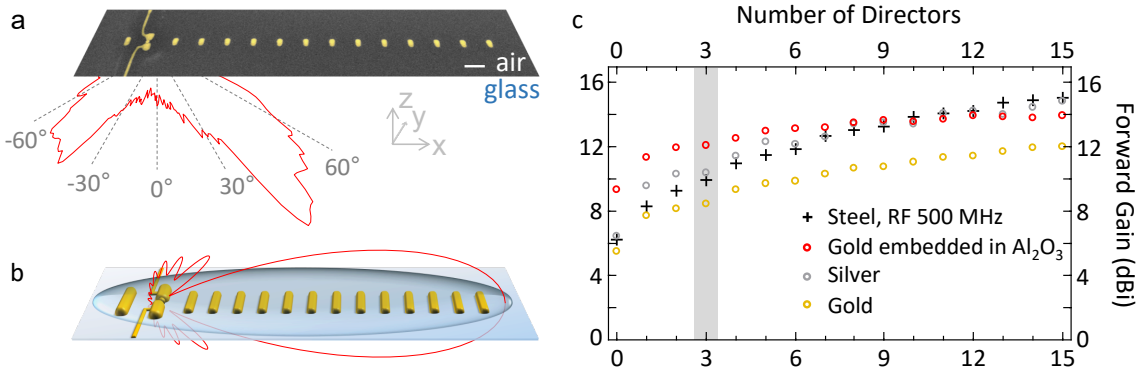

Figure 6.6: Limits of optical Yagi-Uda antennas. (a) SEM image of an actually built Yagi-Uda antenna with 13 directors and measured emission pattern. Due to the air–glass interface, the emission is refracted in the glass substrate. Scale bar, 200 nm. (b) Sketch of optical antenna with 13 directors in an homogeneous surrounding with n = 1.52. The simulated emission pattern is superimposed. (c) Calculated forward gain of different Yagi-Uda antennas with varying number of directors. Black crosses: stainless-steel antenna in air operating at radio frequencies (RF; 500 MHz). Golden circles: gold antenna operating at 870 nm. Silver circles: silver antenna operating at 870 nm. Red circles: gold antenna embedded in 300 nm Al_2O_3 layer operating at 870 nm. All optical antennas are surrounded by a homogeneous n = 1.52 medium. The case for three directors is highlighted with the gray stripe. Simulations were carried out by Philipp Grimm using FDTD as well as standard numerical algorithms [161, 162]. Taken and adapted from reference [20].

thus, directors further away from the feed are reached by less optical field (cf. figure 6.6 a). Hence, many directors in a 15 element antenna do not contribute to the directionality anymore. In addition, it is speculated that the additional path length for ligh traveling to the detector (basically sitting beneath the substrate) via distant directors results in a phase lag and consequently leads to destructive interference. As more directors are added to the antenna, this effect becomes stronger. RF antennas do not face these problems, because they are surrounded by a homogeneous medium, *i.e.* air. Such a symmetric dielectric surrounding could also be achieved in the presented experiment by adding a droplet of immersion oil on top of the antennas, which matches the refractive index of the glass substrate (n = 1.52). However, this prevents recording of emission pattern as light is no longer radiated into the substrate, but is pushed beyond the acceptance angle of high-NA objectives. These experiments require an advanced detection scheme, which is far exceeding the scope of the current work. Instead, the emission pattern of antennas embedded in a homogeneous n = 1.52 medium are simulated (all FDTD simulations were carried out by Philipp Grimm). Figure 6.6 b depicts a sketch of such a 15 element structure superimposed by the calculated emission pattern. As expected, the pattern is symmetric and exhibits

a much higher FB ratio of 13.2 dB at 870 nm.

In order to compare these simulated optical antennas with their RF counterparts and identify limits as well as possible advantages in the optical regime, the forward gain is introduced:

$$GAIN[dBi] = 10 \times log_{10}\left(\frac{I_{Fw}}{I_{Isotropic}}\right). \tag{6.1}$$

This is the figure of merit in RF antenna technology and compares the intensity in forward direction I_{Fw} with the intensity of an isotropic emitter $I_{Isotropic}$. Unfortunately, the latter cannot be easily measured in optical experiments at the nanoscale (this is why the FB ratio is used instead to compare optical antennas). Yet, in simulations, the forward gain can be calculated and is plotted in figure 6.6 c for different Yagi-Uda antennas as a function of director number. Optical gold and conventional RF antennas show a similar behavior: Starting at moderate values, the forward gain first increases strongly as more directors are added to the antenna, but then deflates and reaches a plateau. RF antennas reach much higher values of up to 15.1 dBi, but as gold is replaced with the less lossy silver, the optical antennas achieve similar values. This proves that the inferior performance of gold structures is only based on high absorption losses, and thus, concepts of classical Yagi-Uda theory (*e.g.* director scaling) can be readily transferred to the optical regime by choosing the right antenna material as well as surrounding. Moreover, silver antennas even outperform their classical counterparts for a small number of directors, which is attributed to the kinked connectors acting as additional reflectors (see reference [20]). In contrast, the connection wires do not play a significant role in the RF antennas.

The optical regime further offers the advantage to modify the propagation of light by designing a specific dielectric landscape, *e.g.* by adding a material with high refractive index. In this example, a gold antenna operating at 870 nm is embedded in a 300 nm Al_2O_3 layer. The structure is still situated on glass and the entire arrangement is encapsulated with immersion oil. This results in a dielectric landscape of $n_1 = 1.52$ / $n_2 = 1.67$ / $n_3 = 1.52$, by which light is confined to a 2D waveguide mode. As shown in figure 6.6 c (red circles), such embedded devices clearly outperform both silver and RF antennas for up to nine directors (*e.g.* 12.1 dBi for three directors). Hence, these theoretical results are especially promising for low-footprint highly directional antennas for light and will inspire future research in the field of optical antenna communication.

6.5 Conclusion and Outlook: Towards Nanoantenna Communication

In this chapter, I demonstrated the design, fabrication and characterization of electrically driven optical Yagi-Uda antennas. Light was generated by IET and radiated in-plane to a specific direction due to the sophisticated structure geometry that was milled from single-crystalline gold platelets via gallium FIB. Tunnel junctions were fabricated by means of feedback-controlled DEP, in which the scattering spectrum of the antenna was monitored in real-time to detect the placement of a single particle within a prefabricated feed gap. This technique led to reproducible tunnel gaps and relatively high success rates of almost 50 %, thus, it is more appropriate for tunnel junction fabrication than the previously presented AFM pushing [43] and electromigration [46, 49]. The presented high-quality structures reached FB ratios of up to 9.1 dB (pixel method) or 6.5 dB (areal method), respectively, clearly outperforming all hitherto published optical antennas.

Simulations showed that the directionality can be further improved and even match that of RF antennas by adding more directors, but only if a low loss antenna material (*e.g.* silver) and symmetric dielectric surrounding are chosen. In this context, it was demonstrated (in simulations) that an optical gold antenna embedded in a layer of Al_2O_3 and encapsulated by a material matching the refractive index of the substrate (*e.g.* immersion oil), even surpasses the directionalities of classical RF as well as optical silver antennas.

The novel developments that this work will stimulate can be divided into two categories: experiments based on the presented manufacturing toolbox and device specific research towards applications. First, I want to quickly address the former before I discuss the latter in more detail. The highly accurate FIB milling of single-crystalline substrates in combination with the precise positioning of tunnel barriers via DEP can readily be implemented to fabricate other complex nanostructures such as log and parabolic mirror antennas. An example of a completely different geometry is shown in chapter 7, in which electrically driven plasmonic nanocircuits with multiple tunnel junctions are presented. Additionally, feedback-controlled DEP can also be employed to place optically active nanoparticles into the antenna gaps, *e.g.* nanodiamonds, quantum dots or light-emitting molecules [65]. By slightly improving the sensitivity of the feedback, it might even be possible to deposit individual emitters paving the way for antenna enhanced single-photon sources at room temperature [35–37, 163] as well as single-molecule sensing [33, 155, 164].

Based on the results presented in this chapter, it seems feasible to combine the large directionality and functionality of RF antennas with the large bandwidth and small footprint offered by optical frequencies. A particular vision of our research group is - similar to how RF antennas are used - the direct communication

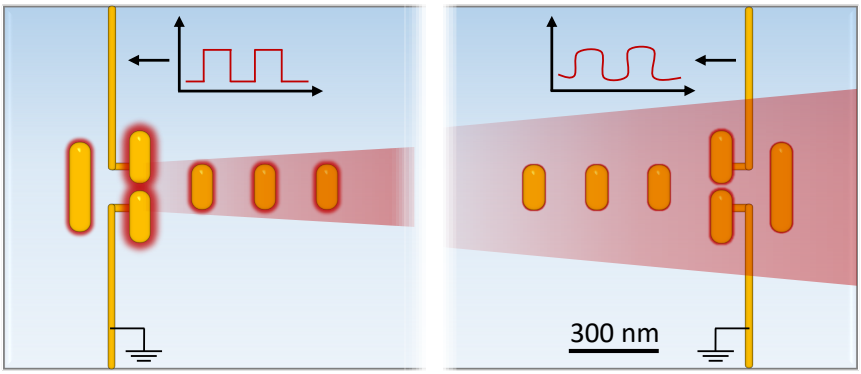

Figure 6.7: Electrically driven optical antenna communication. A pair of nanoscale Yagi-Uda antennas on a glass substrate exchange information by sending and receiving optical signals.

between two electrically driven, in-plane nanoantennas via light, as illustrated in figure 6.7. The sketched antennas exhibit the previously presented design; the directive connectors as well as the dielectric cover (potentially with high refractive index layer) are necessary and beneficial for such an optical antenna link. Yet, in this work, I focused exclusively on the transmission. What is still missing is the reception of light via nanoantennas (sometimes called rectenna).

In principle, the presented antennas as well as the process of inelastic electron tunneling are reciprocal, *i.e.* an incoming photon can trigger a tunneling process, which leads to a change in measured current. This has already been shown for non-resonant rectennas [49]. These structures are illuminated with high intensity femtosecond laser pulses (810 nm) to excite photon-assisted electron tunneling across biased break junctions. Later, this scheme was even extended to realize a wireless optical link [135]: an in-plane directional nanoantenna is again excited by a laser (785 nm) and the antenna scattering is detected by the rectenna, which is positioned a few micrometers away. The transferred power follows an inverse square relation with distance between transmitter and receiver. Although these experiments are first proof-of-principles for antenna communication at the nanoscale, this scheme is - in my opinion - not suitable for purely electrically driven devices. The proposed rectenna requires a very high illumination power of $\sim$5 mW per μm^2 to generate a photocurrent of $\sim$1 nA (this current can easily be measured in conventional electrical setups), *i.e.* roughly three million photons are needed to generate one tunneling electron. However, the IET driven Yagi-Uda antenna presented here only has a total output power on the order of 10 pW.

In order to bridge the gap between emitted and detectable power, transmitter and receiver efficiencies have to be increased significantly. Note, the sensitivity of photocurrent measurements can also be enhanced to almost 10 fA by using the sophisticated lock-in technique, yet, this would further reduce the compactness

of the setup and requires integration times of several seconds. Hence, this measurement scheme is not suitable for high bandwidth data transfer. On the receiver side, the efficiency of photon-assisted electron tunneling can be improved by increasing the photon absorption cross-section. As nanoscale devices have inherently small geometrical cross-sections, the best way is to employ resonant optical antennas (in contrast to non-resonant stripes), which strongly confine incoming light to the tiny tunnel gap, and thus enhance the coupling between photons and electrons. Considering reciprocity of emitting and receiving photons via antenna-enhanced IET, this results in a potential improvement of two to three orders of magnitude [43].

Notably, the field enhancement is further increased in silver antennas with very sharp feed gaps and it was demonstrated that external quantum efficiencies of up to 10^{-2} (here I report 10^{-5} to 10^{-4}) can be reached for light emission via IET, however the output power was still limited to 100 pW. Even if both, transmitter and receiver, exhibit such large field enhancements, the efficiencies for sending and detecting photons would most likely still be too low to wirelessly link two nanoantennas with distances of one ore more micrometers (at least without lock-in amplifier). Probably the most promising approach to further improve the efficiency, and thus the output power, of tunneling devices is to employ resonant inelastic electron tunneling. In this approach, resonant electronic states are inserted into the gap in order to increase the inelastic tunneling rate and - at least in theory - external quantum efficiency of almost 100 % might be achieved [165]. Experimentally, this was realized by placing a metallic quantum well between two metal electrodes [75]. The resulting device, that is not a single nanostructure but spans a large area of several square micrometers, exhibits an inelastic tunneling efficiency of up to 30 % with output powers on the order of 1 nW. The integration of this concept into optical antennas is challenging, but might be possible by replacing the *CTAB* shell of gold nanoparticles with molecules exhibiting resonant electronic states and placing such particles into the antenna feed gap. Electrons would then tunnel across the metal-organic-metal junction via resonant states, which are provided by the particle shell.

Although IET offers interesting advantages, *e.g.* spectral tunability in the absence of active materials or ultrafast switching times [71], the (time) stability of IET devices is usually insufficient for applications [43, 74]. The tunneling current strongly depends on the barrier width, which can change due to the extremely large electric fields in the gap region. Therefore, different mechanisms for light generation and detection at the nanoscale have been investigated and are currently a research subject in our group. For example, interfacing metallic nanoantennas with semiconductor materials allows to detect sub-bandgap photons with efficiencies on the order of 10^{-4} electrons per photon [166]. This detection-only scheme is based on the injection of hot electrons from the metal into the semiconductor over a Schottky-barrier and is facilitated by the field enhancement of the optical antenna. In a similar approach, gold antennas are

sandwiched between two electrically connected graphene sheets [167]. This yields even higher photon-electron conversion rates of up to 20 % and allows to measure illumination in the range of few microwatts. Currently, our group is developing a hot electron injection based light detector that even offers electrically tunable color and polarization sensitivity by making use of sophisticated antenna geometries.

A particularly promising route to nanoantenna communication is offered by monolayers of transition metal dichalcogenides (*TMDCs*), such as WS_2 and WSe_2 [168, 169]. These 2D semiconductors have recently gained a lot of interest from the scientific community due to their fascinating optoelectronic properties in combination with atomic-scale thickness. Compact, microscale p-n junctions based on different *TMDCs* have been fabricated that can not only detect light with high photoresponsivities (several 100 mA/W), but also offer electrically generated light emission [170–173]. In order to further enhance their optoelectronic response, multiple hybrid structures have been presented, in which *TMDCs* are coupled to optical antennas [174–177]. Such devices also offer internal photoamplification (gain) due to avalanche-like effects, making them especially intriguing for the reception of very weak optical signals [178]. Many demonstrations rely on metallic nanostructures covered with a *TMDC* monolayer, but bending the monolayer changes the electronic properties and complicates the interfacing of the 2D semiconductor. For this reason, antennas should be placed on top of perfectly flat *TMDC* sheets. This is especially challenging when nanostructures are electrically connected to larger electrodes and a transfer technique is currently being developed in our research group for this purpose. Placing the *TMDC* underneath the antenna further offers the advantage to access the semiconductor with a gate electrode, allowing to electrically tune the properties of the hybrid antenna device. It is also expected that these devices exhibit a better time stability as comparable IET-based structures. Yet, so far, no electrically driven nanoantenna has been demonstrated, which is able to emit and detect light with sufficiently high efficiencies.

Considering that the detection of few microwatts of light is already possible using nanoantennas, the gap between emittable and detectable power is currently five to six orders of magnitude. In my opinion, although challenging, it is possible to bridge this gap in the future, with the greatest improvement potential probably lying in the area of light emission.

The in-plane communication between highly directional and low-footprint optical Yagi-Uda antennas is especially promising for on-chip data communication, where information is transmitted between antennas with high bandwidth and low heat generation. The resulting communication scheme might even allow transistors from one computer chip to be directly linked to transistors on other chips, paving the way for novel architectures. Even though hardware development is constantly advancing, optical Yagi-Uda antennas are an intriguing candidate to play an important role in future computational devices.

7 | Nanoscale Electrical Excitation of Distinct Modes in Plasmonic Waveguides

Large parts of this chapter are published in *Nanoscale Electrical Excitation of Distinct Modes in Plasmonic Waveguides* by Maximilian Ochs, Luka Zurak, Enno Krauss, Jessica Meier, Monika Emmerling, René Kullock and Bert Hecht. Nano Letters **2021**, 21 (10), 4225-4230.
doi.org/10.1021/acs.nanolett.1c00182

7.1 Introduction

In the last chapter I introduced a new strategy for bottom-up assembly of electrically connected nanoantennas. By using dielectrophoresis (DEP), 1 nm tunnel junctions are fabricated in a reproducible manner - a requirement for light emission based on inelastic electron tunneling (IET). Moreover, these optical antennas are not only the smallest electrically driven light sources, but their refined geometries determine the properties of radiation, such as frequency, polarization and even the direction of emission by *e.g.* using the well known Yagi-Uda design. In this chapter, a completely different device geometry is employed to confine and manipulate electromagnetic waves at the nanoscale. Light in form of guided plasmons is electrically excited in optical nanocircuits equipped with multiple, precisely positioned tunnel junctions. Each junction is created by DEP and facilitates the excitation of a different plasmonic waveguide mode with different near-field symmetry [21].

The structure is based on a plasmonic two-wire transmission lines (TWTL). This geometry - which was already introduced in subsection 2.3.1 - offers two orthogonal, propagating plasmonic modes in the optical regime. In previous experiments, TWTLs have been employed to route optical signals [95], enhance nonlinear optical effects [25] and provide cut-off-free subwavelength localization of mid-infrared light [97]. Later it was shown, that either of the two modes can be excited selectively by controlling the polarization of the excitation light [22].

This has enabled a variety of experiments, ranging from second harmonic generation [179], quantum emitter coupling [154, 180] and mode conversion [181] to advanced polarization control at the nanoscale [23, 24]. Yet, all these demonstrations relied solely on far-field excitation using bulky laser setups.

The electrical excitation of distinct plasmonic modes is advantageous as it reduces the overall footprint of the experiment and merges plasmonic and electric nanocircuitry, potentially enabling novel nano-optoelectronic devices. In this context plasmonic organic and inorganic LEDs have been discussed [69, 70, 182, 183], but here, IET is employed, because it offers a nanoscale excitation source that can be precisely positioned by already established techniques. For more information about the electrical driving of plasmonic TWTLs and the modelling of the resulting electroluminescence see subsection 2.3.2. Although, the excitation of propagating plasmons via IET has already been shown [91, 134, 184–187], the mode-selectivity presented here has not been possible before.

This chapter demonstrates the distinct electrical excitation of the lowest-order symmetric and antisymmetric plasmonic modes in a TWTL. Mode-selectivity is achieved by precisely positioning nanoscale excitation sources, *i.e.* junctions for inelastic electron tunneling, within the electric fields of the respective modes with sub-10 nanometer accuracy (see section 7.2). This is accomplished using an advanced fabrication scheme that combines focused gallium and helium ion beam milling with DEP. Section 7.3 presents the optoelectronic characterization of several waveguide structures. Importantly, at the far end of the TWTL the propagating modes are converted into far-field radiation at separate spatial positions showing two distinct orthogonal polarizations. Hence, the mode-selective device represents the smallest electrically-driven light source with directly switchable polarization states. Potential follow-up experiments are discussed in the outlook (see section 7.4).

7.2 Concept and Structure Design

In this section, I explain the basic concept of mode selective plasmon excitation in electrically connected TWTLs. The underlying theory is covered in section 2.3. Later, the structure layout is presented including waveguide design, dimensions and fabrication details. For more information about focused ion beam (FIB) milling and DEP refer to section 4.1 as well as chapter 6.

The electrically driven nanocircuit is illustrated in figure 7.1 a. It consists of a TWTL with mode detector supporting two fundamental propagating modes: the symmetric (blue) and the antisymmetric mode (red). Simulated electric field distributions of both plasmonic modes along the waveguide are depicted in figure 7.1 b (mode excitation at 800 nm). The antisymmetric mode is confined to the gap between the gold wires, whereas the symmetric mode is guided at the outer sides of the waveguide. Electrical excitation is facilitated via IET. To this end,

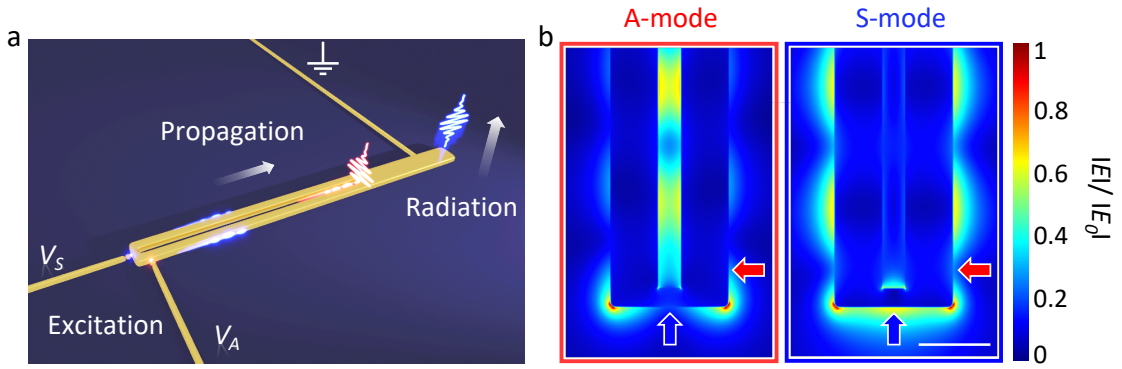

Figure 7.1: Concept of an electrically driven mode-selective plasmonic TWTL. (a) Illustration of the nanocircuit, including a TWTL with mode detector, two tunnel junctions and three connection wires. The tunnel junctions independently excite either of two orthogonal plasmonic modes, which then propagate along the waveguide. At the mode detector, they are spatially separated and emitted as orthogonally polarized light. Note, the antisymmetric mode (A-mode) is radiated at the beginning, while the symmetric mode (S-mode) is radiated at the end of the mode detector. (b) Simulated electric field distributions of the two modes (A-mode: red; S-mode: blue) along the beginning of the waveguide. These field profiles originate from interference between an excited mode and its reflection, thus forming a standing wave pattern. Optimal positions for the exclusive excitation of the A-mode and S-mode are marked by red and blue arrows, respectively. Scale bar; 100 nm. Reprinted and adapted with permission from reference [21]. Copyright (2021) American Chemical Society.

three connection wires are introduced: one to ground the TWTL and two for applying electrical signals (labeled V_S and V_A in figure 7.1 a). The latter are separated from the grounded waveguide by DEP-fabricated tunnel junctions. Upon applying a voltage, electrons tunnel inelastically across the nanometer gaps, thereby exciting accessible plasmonic modes (see subsection 2.3.2). The blue and red junction in Fig. 7.1 a excite only the symmetric and antisymmetric mode, respectively. After excitation, the modes propagate along the waveguide and reach the mode detector, where they are spatially separated. Since the field of the antisymmetric mode is mainly confined in between the waveguide wires, it is reflected and radiated to the far-field at the gap shortcut. The symmetric mode, however, propagates past the gap shortcut and is reflected and radiated at the waveguide termination. Furthermore, the out-coupled light is linearly polarized according to the near-field symmetry of the respective mode [22]. This represents a way to verify, which plasmonic mode has been excited.

The key aspects of mode selective operation are the nanoscale excitation offered by IET in combination with the exact location of the tunnel junctions. Since the excitation (incoupling) efficiency of a mode is directly linked to the local density of optical states (cf. subsection 2.2.1), and thus the modal electric

field at the position of excitation, a specific mode can be launched by controlling the nanoscale location of the tunnel junctions [21, 48, 62]. In subsection 2.3.2, the procedure to find the optimal positions is described (see figure 2.14) and an expression for the incoupling efficiency as a function of the modal field is introduced (equation 2.19). FDTD simulations were carried out by Luka Zurak, in which the respective modes are launched at the far end of the waveguide and propagate towards the incoupler (called the mode approach). Upon reflection, standing wave patterns form which represent the spatial modal fields (see figure 7.1 b). The highest incoupling efficiency is obtained by placing the tunnel junction at the field maximum of the desired mode. Note, that in order to launch single modes, the field distribution of the other mode must be taken into account as well and a position must be found that exhibits high fields for one and close to zero fields for the other mode. The ideal position to excite the symmetric mode is at the center of the incoupler since the antisymmetric mode exhibits a field strength node at this location (blue arrows in Fig.7.1 b). In contrast, the symmetric mode has a field zero in the waveguide gap; hence, this would be the ideal position for the exclusive excitation of the antisymmetric mode. However, it is practically not possible to place a connection wire at this position. Alternatively, one can maximize the incoupling ratio between antisymmetric and symmetric mode by placing the junction at the outer sides of the waveguide, 70 nm away from the front edge (red arrows in Fig. 7.1 b). Due to drastic spatial field variations, displacing the excitation source by only a few nanometers strongly changes this ratio. Therefore, a very high accuracy in positioning the tunnel junction is required, which is achieved by combining FIB milling with the accurate placement of functionalized nanoparticles via DEP [20].

The sample layout shown in figure 4.1 is slightly modified for waveguides with two tunnel junctions. Figure 7.2 a depicts a structured gold platelet with a maximum of six plasmonic TWTLs, each connected to three electrodes. An exemplary structure before DEP is displayed in figure 7.2 b; its coarse shape is milled with gallium FIB (the exact dimensions are listed in the figure caption). The ground connector is placed such that its influence on plasmon propagation is minimal, while the two active connectors are attached according to red and blue arrows in figure 7.1 b. Feed gaps of single-junction waveguides are fabricated as before via gallium FIB; but for waveguides with two junctions, helium FIB is employed by Jessica Meier to mill sharp gaps between waveguide and connectors (see figure 7.2 c). An etching step can be added to remove remaining gold debris without strongly undermining the pointed features [21]. This method was chosen to manage the increasing difficulty of filling two consecutive gaps. Particles - after DEP - often end up in the gap slightly displaced by a few nanometers. This results in degraded mode-selectivity, due to the aforementioned spatial field variations (cf. figure 7.1 b). By interfacing a gold nanoparticle with sharp features, and thus small contact areas, a considerably higher accuracy in placing the tunnel junction is obtained leading to improved mode-selectivity.

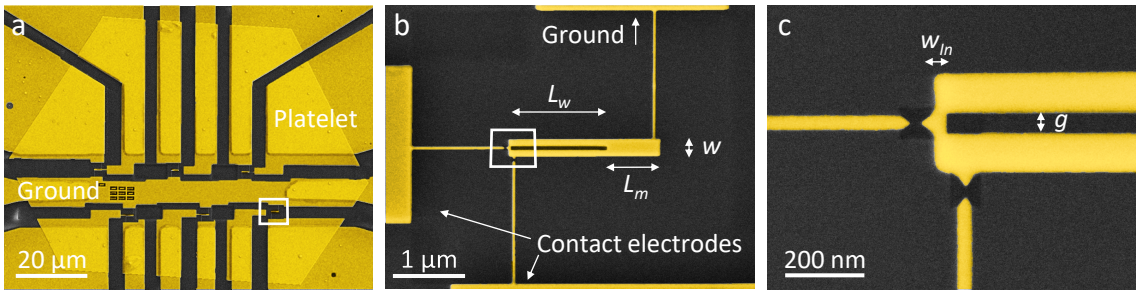

Figure 7.2: Structure layout and fabricated plasmonic waveguides. (a) Processed platelet on top of an evaporated electrode structure. The layout resembles that shown in figure 4.1 a, but only six waveguides are fabricated per platelet; each exhibiting one ground and two contact electrodes. (b) Zoom-in to a plasmonic waveguide before dielectrophoresis. Tiny wires connect the structure to the larger electrodes. (c) Further zoom-in to the front end of the waveguide. The sharp gaps, which are fabricated via helium ion milling, are later filled by dielectrophoresis in order to fabricate tunnel junctions. Each contact electrode is responsible for one tunnel junction. L_w (TWTL length): 2200 nm; L_m (mode detector length): 800 nm; w (waveguide width): 250 nm; g (waveguide gap size): 50 nm; w_{in} (incoupler width): 35 nm. Reprinted and adapted with permission from reference [21]. Copyright (2021) American Chemical Society.

In contrast to the previous chapter, live-feedback based on white-light scattering is not employed during DEP as the feed gap geometry in waveguides does not exhibit strong far-field scattering. Instead, a voltage is applied for a short and fixed period of time. To increase the likelihood of single particle deposition, parameters have been optimized by performing multiple DEP tests followed by SEM imaging. Most single particle junctions were observed by applying 1.5 V for 20 s at a frequency of 15 MHz. Note, that the particle solution is not diluted 1:500 with water, but 1:5000, in order to prevent particles from attaching to the much larger structure. In total, the success rate for consecutive filling of two feed gaps with single particles was below 10 %, nevertheless, several functioning devices were fabricated and are presented in the next section.

7.3 Optoelectronic Characterization

After discussing concept, design and fabrication of electrically driven plasmonic waveguides, this section presents the optoelectronic characterization of manufactured devices.

Figure 7.3 a and b show SEM images of two different single-junction nanocircuits, in which only one of the two plasmonic modes is excited. The feed gaps of both structures are filled with a single particle. Upon applying a DC voltage (1.8 V - 3 V) light is emitted and recorded in the image plane using the optical setup described in subsection 4.2.2. The corresponding electroluminescence (EL)

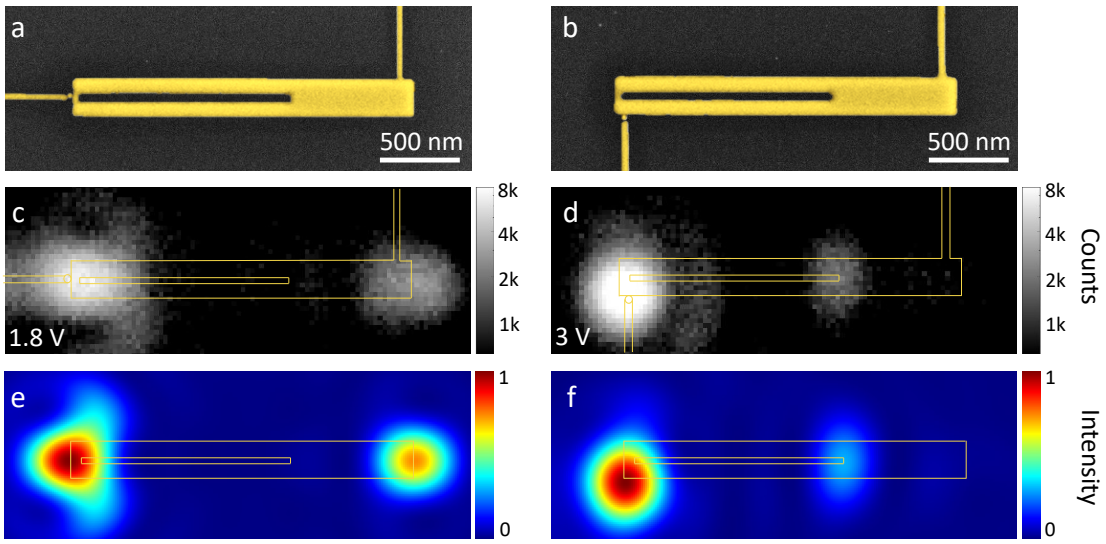

Figure 7.3: Electrical excitation of two distinct plasmonic modes in separate structures. (a) and (b) SEM images of electrically driven waveguides for the excitation of (a) symmetric and (b) antisymmetric mode. (c) and (d) Measured image-plane light emission of the respective waveguides upon applying a voltage for 5 s. The radiation at different positions of the mode detector clearly indicates the excitation of distinct plasmonic modes. (e) and (f) Simulated far-field response of the waveguides (calculated by Luka Zurak). The tunnel junctions in (a) and (b) as well as the excitation dipoles in (e) and (f) are positioned according to the blue and red arrows in figure 7.1 b. Reprinted with permission from reference [21]. Copyright (2021) American Chemical Society.

maps are shown in figure 7.3 c and d. In each case, strong emission is observed at the tunnel junction which is attributed to the excitation of photons coupling directly to the far-field. More importantly, a second emission spot is recorded for both waveguides indicating the excitation of distinct plasmonic modes that propagate along the TWTL and radiate at the corresponding position of the mode detector. It is thus possible to launch a single plasmonic mode with negligible contribution of the other mode by choosing the right tunnel junction position and making use of the precise electrical excitation offered by IET. Even though the position for exciting the antisymmetric mode is not ideal - the tunnel junction is not located in a field node of the symmetric mode (cf. figure 7.1 b) - the emission intensity at the end of the waveguide is very weak, thus verifying that the in-coupling to the antisymmetric mode dominates. The reduced emission intensity at the mode detector compared to the incoupler is attributed to damping along the waveguide. In order to compare the measurement with expectations, the emission for both waveguides is calculated using FDTD. For these simulations - carried out by Luka Zurak - a dipole source is placed at the respective tunnel junction position (cf. figure 7.3 a and b) and excites the structure at 750 nm. The resulting expected image plane emission is presented in figure 7.3 e and f,

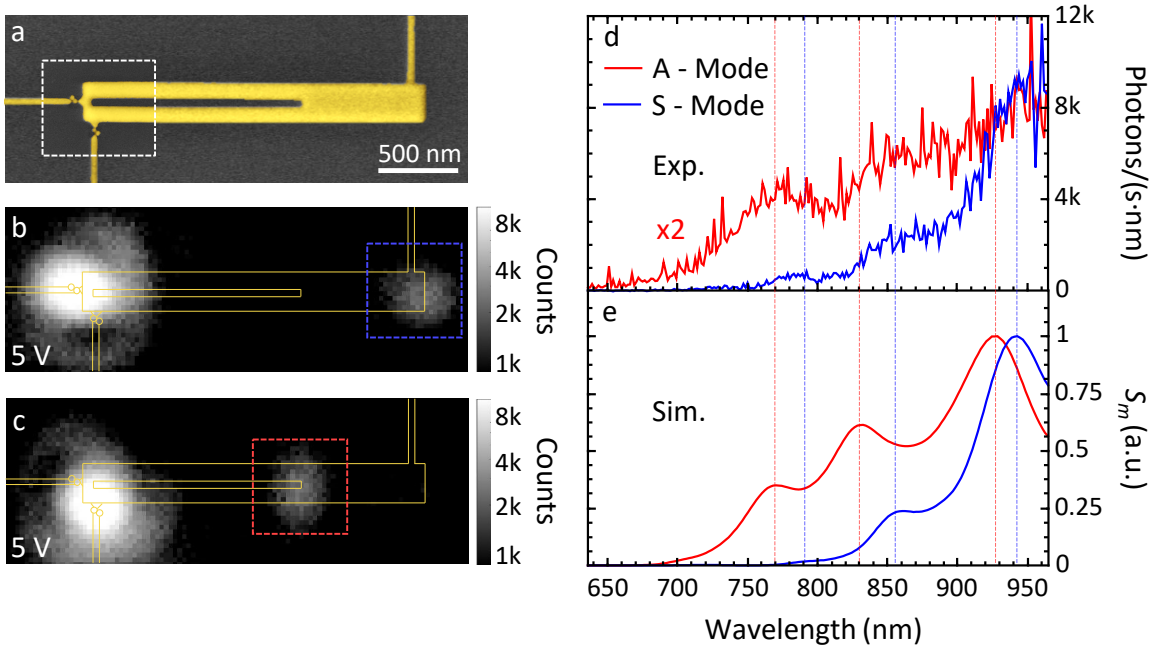

Figure 7.4: Mode-selective excitation within a single device. (a) SEM image of electrically driven waveguide with two distinct tunnel junctions. The dashed square indicates a high-resolution overlay image. (b) and (c) Measured image-plane light emission of the same device. A voltage of 5 V is applied to the (b) horizontal and (c) vertical tunnel junction for 5 s and 2 s, respectively. (d) Corresponding spectra of the symmetric (blue, S) and antisymmetric (red, A) mode. The spectra are recorded in the areas marked by rectangles in (b) and (c) using a polarization filter and are corrected by the quantum efficiency of the setup. (e) Simulated spectra (calculated by Luka Zurak). The dashed lines mark the peak positions in the simulations. Reprinted with permission from reference [21]. Copyright (2021) American Chemical Society.

showing good agreement with the measurements.

Next, I demonstrate a mode selective nanocircuit able to switch between the electrical excitation of antisymmetric and symmetric mode. Figure 7.4 a depicts the SEM image of a finalized structure; it resembles the device introduced in figure 7.1 a. Two tunnel junctions, which are placed at the previously discussed positions, allow to separately excite the two propagating modes. Feed gaps are filled consecutively via DEP: The horizontal electrode is connected to ground and an AC voltage is applied to the vertical electrode, thus placing a particle into the vertical feed gap. This procedure is then repeated for the other junction. However, in this example, both gaps are filled with two particles. As feedback is not used during DEP, the AC voltage was not turned off quickly enough resulting in the attraction of an additional particle. Nevertheless, the performance of this device is not diminished, which is attributed to the sharp and pointed gap fea-

tures (see figure 7.2 c). Due to the small contact area between particle and gap, a tunnel junction forms at the desired position after the first particle is trapped, and thus the second particle has a negligible influence. Note, the attraction of multiple particles could be prevented in the future by implementing a feedback system that is not based on far-field scattering, but instead relies on *e.g.* measuring the conductivity across the feed gap.

Corresponding EL maps are acquired as described before and are shown in figure 7.4 b and c. Again, strong emission spots are observed at the respective tunnel junctions. By applying a voltage $V_S = 5\,\mathrm{V}$ to the horizontal junction only the symmetric mode is excited leading to light emission at the end of the waveguide (cf. figure 7.4 b). In contrast, applying a voltage $V_A = 5\,\mathrm{V}$ to the vertical junction results in distinct excitation of the antisymmetric mode and radiation at the beginning of the mode detector (cf. figure 7.4 c). These measurements are in agreement with the results obtained in figure 7.3 and highlight the mode-selectivity of the two-junction nanocircuit. This is the first experimental demonstration of an electrically driven plasmonic TWTL that allows to actively switch between two propagating plasmonic modes. Due to the link between mode symmetry and far-field polarization, this device also represents the smallest electrically driven light source capable of actively switching between two linear polarization states.

In order to further investigate the radiated light, emission spectra are recorded at the mode detector and compared to simulations (see figure 7.4 d and e). The two experimental spectra show a similar pattern with oscillations resembling those of a Fabry-Perot resonator. This can qualitatively be reproduced in FDTD simulations, in which spectra are obtained according to equation 2.20. Remaining deviations are attributed to uncertainties in the gap geometry, such as particle placement. [21]. The oscillations originate from the cavity character of the waveguide that is fed by a spectrally broad excitation source, *i.e.* IET. In simulations, the tunneling process is modeled by the source efficiency, which is interchangeable with the current power spectrum introduced in subsection 2.2.2 [43, 48, 62]. Therefore, the excitation occurs over a broad range of frequencies - even at a fixed applied voltage. The waveguide acts as a Fabry-Perot cavity partially reflecting the propagating plasmons at the waveguide end; with the resonance wavelength being a multiple integer of the cavity length (see section 2.1). Hence, the out-coupled light intensity oscillates across the spectrum. Due to the difference in propagation length and effective wavelength between symmetric and antisymmetric mode, the peaks in the spectra are shifted compared to each other (cf. figure 7.4 d).

Moreover, the average plasmon launching efficiencies can be estimated. The number of out-coupled photons per tunneled electrons can be directly measured. Simulations then allow to approximate all losses due to propagation and radiation. This yields an average launching efficiency of $2{\cdot}10^{-5}$ and $1.4{\cdot}10^{-4}$ plasmons per electrons for the antisymmetric and symmetric mode, respectively, which is

comparable to previously obtained efficiencies [20, 43].

The appearance of modulated emission spectra is directly connected to the modal electric field, thus further demonstrating that plasmon excitation depends on the exact location of the source (tunnel junction). I want to emphasize this fascinating connection: the process of launching a plasmon is dictated by a standing wave pattern, which originates from interference between the same plasmonic mode and its reflection - even before the plasmon is actually excited.

7.4 Conclusion and Outlook

Here, I demonstrated - for the first time - the selective electrical excitation of two propagating plasmonic modes in TWTL waveguides. This chapter is thus a further example of the potential unlocked by electrically connecting nano-optical systems. Moreover, it highlights the capabilities and the accuracy of the employed fabrication procedure that yields refined optical nanocircuits with multiple tunnel junctions.

The key to almost-perfect mode-selectivity is the extremely confined excitation offered by IET as well as the exact location of the tunnel junction. The incoupling efficiency of a mode is directly related to the modal electric field at the position of excitation. In order to excite only one plasmonic mode, the tunnel junction must be placed at a location, at which the electric field amplitude of the other mode vanishes. Ideal positions were found via FDTD simulations and an advanced fabrication scheme based on gallium as well as helium FIB milling in combination with DEP was used to fabricate devices with the required nanometer accuracy. In addition, I demonstrated a two-junction nanocircuit able to actively switch between the electrical excitation of symmetric and antisymmetric mode, which further represents the smallest electrically-driven light source with directly switchable polarization states. Such mode selective operation constitutes a key advantage over conventional single-mode integrated photonics.

Plasmonic waveguides made from gold exhibit favorable chemical stability, but suffer from large propagation losses in the visible regime, thus they are mostly limited to proof-of-principle experiments. Silver offers much lower losses and supports surface plasmons across the spectral range from 300 nm to 1200 nm. It is therefore the preferred material for applied plasmonics [188]. Recently, the wet-chemical growth of large single-crystalline silver platelets was shown [152, 153] and first silver TWTLs were developed [25, 154], demonstrating the potential of silver based optical nanocircuitry. For this reason, our research group is currently exploring silver platelet growth and subsequent fabrication of silver structures.

In future experiments full control over the polarization state may be accomplished by further refining the waveguide geometry and exploiting the interfer-

ence of plasmonic modes. An electron tunneling across a single junction can, in principle, excite the symmetric and antisymmetric mode at the same time, if both modal electric field amplitudes are equal at this position. As the plasmons propagate along the waveguide - one confined to the waveguide gap and the other one guided on the outside - they experience different damping and thus a different phasaree shift (see figure 2.12 c in subsection 2.3.1). Once the modes interfere at the end of the waveguide, the polarization of the out-coupled light depends on the exact phase shift, which can be modified by changing the waveguide dimensions. This way, an ultra-compact circularly polarized light source can be realized, if the phase shift between both modes at the interference point is exactly 90 °. In a further step, this excitation scheme might be used in more sophisticated plasmonic nanocircuits, which route light in predefined pathways while conserving its polarization state [23, 24].

In the previous example, the phase shift is set by the waveguide geometry, but actively tuning the phase by *e.g.* applying a voltage to a gold wire is even more desirable (the waveguide geometry proposed here is not suitable anymore). It has been shown theoretically that locally changing the refractive index above an optical nanocircuit results in a strong phase shift and even leads to conversion between plasmonic modes [189]. Notably, several high-speed plasmonic modulators have been demonstrated by using the Pockels effect (linear electro-optic effect) and changing the refractive index of non-linear organic materials [15–18]. The footprint of these previous devices can be further reduced by applying a TWTL geometry in combination with an advanced fabrication scheme as discussed in this work. Instead of non-linear molecules, nanocircuits can also be covered with *e.g.* titanium dioxide, which leads to a Schottky-barrier between metal and oxide. Upon applying a voltage to one part of the nanocircuit, charge accumulation or depletion at the metal-oxide interface induces a significant change in the oxide's refractive index, thus electrically modifying plasmon propagation [190].

The current work, including the refined fabrication scheme, is a neat demonstration of what is possible today with electrically connected optical nanocircuits and paves the road for future experiments in the field of advanced nanoscale light routing and modulation.

8 | Conclusion and Outlook

Confining and guiding light at the nanoscale - way below the traditional diffraction limit - promises photonic-level transmission bandwidths at electronic-level dimensions [16, 17]. The basic building blocks for such optical nanocircuitry include metallic optical antennas and plasmonic waveguides. In the past, several fascinating experiments have been presented [24, 26, 30, 31, 154], but early demonstrations relied exclusively on the optical excitation of isolated structures. Yet, integrated devices require electrical access and local light generation. This led to the development of electrically driven optical antennas that emit light by inelastic tunneling of electrons across a nanometer gap (IET) [42, 43, 46, 50]. These examples, however, provided only limited functionality and the fabrication of tunnel junctions was tedious and suffered from low success rates.

In this work, the state of the art of metallic nano-optical systems has been further advanced. I focused specifically on structures, in which the electrical connection enables local light generation, but also plays a key role in the assembly of functional devices. It was shown, that the fabrication of tunnel junctions for IET as well as the chemical modification of surface properties can both be facilitated by applying electrical signals to nanoscale electrodes. Furthermore, different geometries were presented that allow to control the properties of the emitted light, such as radiation direction and polarization. Since the exact shape of the respective nanostructures is crucial for their performance, focused ion beam milling of single-crystalline gold platelets was employed to achieve a high fabrication accuracy [14, 53, 54].

The use of electrodes with different work functions is already well established in commercial OLEDs. Mimicking this concept at the nanoscale offers intriguing potential for nano-optoelectronic devices, but presents a major challenge. A solution was demonstrated in chapter 5, where the work function of gold nanoelectrodes was selectively modified by self-assembled monolayers (*SAMs*). In this procedure, surfaces are functionalized with thiolated molecules (e.g. alkanes or PEGs), which are subsequently removed from only one of the nanoelectrodes via oxidative desorption. This can be verified by Kelvin probe force microscopy mapping the effective surface potential of bare and functionalized gold surfaces. Moreover, it was shown that 1-octadecanethiol can block the formation of a subsequent *SAM*, allowing to functionalize both electrodes with

different molecules. Due to the molecule's effect on the metal work function, this technique enabled the fabrication of metal-organic nanoantennas with asymmetric current-voltage characteristics, further demonstrating the potential for nano-optoelectronics. Notably, site-selective functionalization also allows the deposition of oriented molecular assemblies, which paves the way for antenna controlled molecular machinery. A possible experiment is outlined in more detail in section 5.4.

Another focus of this work was the development of devices for nanoscale optical communication. Inspired by radio frequency antennas, chapter 6 presented the first electrically driven in-plane Yagi-Uda antennas that radiate light in a specific direction with forward-to-backward ratios of up to 9.1 dB (pixel method) or 6.5 dB (areal method). These structure are thus clearly outperforming all hitherto published antennas [40, 46, 158, 159]. Tunnel junctions were created via dielectrophoresis (DEP) replacing the tedious atomic force microscopy pushing as well as electromigration. By applying an AC voltage to antennas, surface-passivated gold nanoparticles are deposited in prefabricated 30 nm feed gaps, reducing the gap size to only 1 nm and enabling efficient electron tunneling. Based on the antenna scattering, a live feedback system was employed during this process and relatively high success rates (one particle in the gap) of 50 % were achieved. Light around 870 nm was emitted via antenna-enhanced IET and quantum efficiencies on the order of 10^{-5} to 10^{-4} were recorded. Yet, the presented antennas are not suitable to efficiently detect light. Therefore, further development is necessary in order to realize the optical communication between a set of nanoantennas. Missing steps as well as possible solutions are discussed in more detail in section 6.5.

Chapter 7 presented a further building block for optical nanocircuitry: the first electrically driven plasmonic two-wire transmission line. Distinct propagating modes were launched based on the exact position of tunnel junctions, which were placed with sub-10 nm accuracy by combining FIB milling and DEP. Furthermore, a mode-selective nanocircuit with two tunnel junctions was demonstrated that enables to switch between the excitation of symmetric and antisymmetric waveguide mode. Due to the near-field symmetries of the modes, this device also presents the smallest electrically driven light source with switchable linear polarization states.

So far, most of the possible applications and future experiments that have been discussed in this thesis are about optical communication (with the exception of antenna controlled supramolecular translation). Yet, the structures presented here are also among the smallest light sources that can be driven electrically, and, in combination with the polarization control offered by plasmonic waveguides, are an interesting option to scale down the size of pixels in display technology. Recently, a further step in this direction was made by demonstrating a color-switchable nanoantenna that mimics the function of OLEDs [51]. However, the development of real-world applications still faces several

challenges. In the following I want to focus on three aspects: material, fabrication and stability.

An immediate limitation is the use of gold, which is chemically stable, but exhibits large damping in the visible regime and is thus more suitable for near-infrared light. Single-crystalline silver, although more difficult to handle, offers antenna resonances covering the entire visible regime (red, blue and green) and, due to low damping, is especially interesting for plasmonic nanocircuitry [25, 154, 191]. Moreover, silver Yagi-Uda antennas can reach even higher directionalities as shown in section 6.4.

Even though the fabrication scheme presented here is key for the device functionality, neither FIB milling nor wet-chemical synthesis of gold or silver platelets is suitable for mass production of optoelectronic components. Thus, the fabrication of high quality nanostructures from evaporated silver (or other metals) via lithography techniques should be further investigated. Another aspect - which is not covered in detail here - is the CMOS compatibility of the metal structures [192]. In this context, copper and aluminum electrodes on top of silicon dioxide were recently explored in electrically driven plasmonic devices [187].

Further challenges for IET-based light sources are efficiency and stability (also discussed in section 6.5). While the efficiency can be increased by means of field enhancement [50] or resonant inelastic electron tunneling [75], (time) stability is a major obstacle. The tunneling current strongly depends on the atomic-scale gap geometry and since large electric fields on the order of 1 GV/m are created within the tunnel junction, the gap is subject to change, leading to fluctuating currents as well as light emission (spectrum and amplitude variations). Typically, the structures presented here exhibit stable light emission for 30 seconds [43, 74]. Controlling and maintaining the atomic-scale gap for a longer time is very challenging, and thus, IET devices are suitable for proof-of-principle experiments, but applications might require the use of a different light generation mechanism. A possible solution is the coupling of optical antennas to 2D semiconductors such as WSe_2. Such devices promise better efficiencies and stabilities [170–173], however, the emission frequency is limited by the semiconductor band gap. This means, that the broadband character of IET is traded for an improved stability. Note, layers of transition metal dichalcogenides can be grown via chemical vapor deposition, which, in principle, is a scalable production technique [169].

Although challenges remain, I am confident that we are going to see multiple fascinating experiments in basic and applied research in the future. I also want to highlight the potential of single-crystalline metal platelets, which are currently being investigated in our group as a platform for surface-enhanced Raman scattering applications. As shown here, the electrical connection of nano-optical systems enables local light generation and offers new strategies for device assembly as well as surface modification, yet, it paves the road for even

more functionality, ranging from plasmoelectric conversion [193] and optical field emission [194,195] to charge-modulated second harmonic generation. Moreover, the recent development of high-speed plasmonic modulators for optical interconnects - these devices are fed by external optical signals and do not generate light locally - proves that electro-plasmonics is closer to real-world applications than ever [15–18]. Personally, I am very excited about future developments in nanoantenna communication as well as antenna controlled molecular machinery.

Bibliography

[1] E. Abbe: *Beiträge zur Theorie des Mikroskops und der mikroskopischen Wahrnehmung*. Archiv für Mikroskopische Anatomie **9**, 413, 1873.

[2] Rayleigh: *Investigations in optics, with special reference to the spectroscope*. The London, Edinburgh, and Dublin Philosophical Magazine and Journal of Science **8**, 261, 1879.

[3] L. Novotny and B. Hecht: *Principles of Nano-Optics*. Cambridge University Press, Cambridge, 2012.

[4] G. Z. Mashanovich, M. Milosevic, P. Matavulj, S. Stankovic, B. Timotijevic, P. Y. Yang, E. J. Teo, M. B. H. Breese, A. A. Bettiol, and G. T. Reed: *Silicon photonic waveguides for different wavelength regions*. Semiconductor Science and Technology **23**, 064002, 2008.

[5] J. Cambiasso, G. Grinblat, Y. Li, A. Rakovich, E. Cortés, and S. A. Maier: *Bridging the Gap between Dielectric Nanophotonics and the Visible Regime with Effectively Lossless Gallium Phosphide Antennas*. Nano Letters **17**, 1219, 2017.

[6] L. Sortino, P. G. Zotev, C. L. Phillips, A. J. Brash, J. Cambiasso, E. Marensi, A. M. Fox, S. A. Maier, R. Sapienza, and A. I. Tartakovskii: *Bright single photon emitters with enhanced quantum efficiency in a two-dimensional semiconductor coupled with dielectric nano-antennas*. Nature Communications **12**, 6063, 2021.

[7] G. Grinblat, H. Zhang, M. P. Nielsen, L. Krivitsky, R. Berté, Y. Li, B. Tilmann, E. Cortés, R. F. Oulton, A. I. Kuznetsov, and S. A. Maier: *Efficient ultrafast all-optical modulation in a nonlinear crystalline gallium phosphide nanodisk at the anapole excitation*. Science Advances **6**, eabb3123, 2020.

[8] T. Shibanuma, T. Matsui, T. Roschuk, J. Wojcik, P. Mascher, P. Albella, and S. A. Maier: *Experimental Demonstration of Tunable Directional Scattering of Visible Light from All-Dielectric Asymmetric Dimers*. ACS Photonics **4**, 489, 2017.

[9] P. Biagioni, J.-S. Huang, and B. Hecht: *Nanoantennas for Visible and Infrared Radiation*. Reports on Progress in Physics **75**, 024402, 2012.

[10] R. Chikkaraddy, B. de Nijs, F. Benz, S. J. Barrow, O. A. Scherman, E. Rosta, A. Demetriadou, P. Fox, O. Hess, and J. J. Baumberg: *Single-molecule strong coupling at room temperature in plasmonic nanocavities*. Nature **535**, 127, 2016.

[11] H. Groß, J. M. Hamm, T. Tufarelli, O. Hess, and B. Hecht: *Near-field strong coupling of single quantum dots*. Science Advances **4**, eaar4906, 2018.

[12] E. Murphy: *Enabling optical communication*. Nature Photonics **4**, 287, 2010.

[13] J. Hecht: *The bandwidth bottleneck that is throttling the Internet*. Nature **536**, 139, 2016.

[14] J.-S. Huang, V. Callegari, P. Geisler, C. Bruening, J. Kern, J. C. Prangsma, X. Wu, T. Feichtner, J. Ziegler, P. Weinmann, M. Kamp, A. Forchel, P. Biagioni, U. Sennhauser, and B. Hecht: *Atomically Flat Single-Crystalline Gold Nanostructures for Plasmonic Nanocircuitry*. Nature Communications **1**, 150, 2010.

[15] C. Haffner, D. Chelladurai, Y. Fedoryshyn, A. Josten, B. Baeuerle, W. Heni, T. Watanabe, T. Cui, B. Cheng, S. Saha, D. L. Elder, L. R. Dalton, A. Boltasseva, V. M. Shalaev, N. Kinsey, and J. Leuthold: *Low-loss plasmon-assisted electro-optic modulator*. Nature **556**, 483, 2018.

[16] C. Haffner, W. Heni, Y. Fedoryshyn, J. Niegemann, A. Melikyan, D. L. Elder, B. Baeuerle, Y. Salamin, A. Josten, U. Koch, C. Hoessbacher, F. Ducry, L. Juchli, A. Emboras, D. Hillerkuss, M. Kohl, L. R. Dalton, C. Hafner, and J. Leuthold: *All-plasmonic Mach–Zehnder modulator enabling optical high-speed communication at the microscale*. Nature Photonics **9**, 525, 2015.

[17] M. Ayata, Y. Fedoryshyn, W. Heni, B. Baeuerle, A. Josten, M. Zahner, U. Koch, Y. Salamin, C. Hoessbacher, C. Haffner, D. L. Elder, L. R. Dalton, and J. Leuthold: *High-speed plasmonic modulator in a single metal layer*. Science **358**, 630, 2017.

[18] A. Melikyan, L. Alloatti, A. Muslija, D. Hillerkuss, P. C. Schindler, J. Li, R. Palmer, D. Korn, S. Muehlbrandt, D. Van Thourhout, B. Chen, R. Dinu, M. Sommer, C. Koos, M. Kohl, W. Freude, and J. Leuthold: *High-speed plasmonic phase modulators*. Nature Photonics **8**, 229, 2014.

[19] D. G. Lona, H. E. Hernández-Figueroa, A. Cerqueira S. Jr., G. Stefanini, and H. L. Fragnito: *Applicability of low macrobending loss hollow-core PCF to FTTH applications*. Journal of Microwaves, Optoelectronics and Electromagnetic Applications **10**, 251, 2011.

[20] R. Kullock, M. Ochs, P. Grimm, M. Emmerling, and B. Hecht: *Electrically-driven Yagi-Uda antennas for light*. Nature Communications **11**, 115, 2020.

[21] M. Ochs, L. Zurak, E. Krauss, J. Meier, M. Emmerling, R. Kullock, and B. Hecht: *Nanoscale Electrical Excitation of Distinct Modes in Plasmonic Waveguides*. Nano Letters **21**, 4225, 2021.

[22] P. Geisler, G. Razinskas, E. Krauss, X.-F. Wu, C. Rewitz, P. Tuchscherer, S. Goetz, C.-B. Huang, T. Brixner, and B. Hecht: *Multimode Plasmon Excitation and In Situ Analysis in Top-Down Fabricated Nanocircuits*. Physical Review Letters **111**, 183901, 2013.

[23] C. Rewitz, G. Razinskas, P. Geisler, E. Krauss, S. Goetz, M. Pawłowska, B. Hecht, and T. Brixner: *Coherent Control of Plasmon Propagation in a Nanocircuit*. Physical Review Applied **1**, 014007, 2014.

[24] E. Krauss, G. Razinskas, D. Köck, S. Grossmann, and B. Hecht: *Reversible Mapping and Sorting the Spin of Photons on the Nanoscale: A Spin-Optical Nanodevice*. Nano Letters **19**, 3364, 2019.

[25] C. Schörner and M. Lippitz: *Single Molecule Nonlinearity in a Plasmonic Waveguide*. Nano Letters **20**, 2152, 2020.

[26] D. E. Chang, A. S. Sørensen, E. A. Demler, and M. D. Lukin: *A single-photon transistor using nanoscale surface plasmons*. Nature Physics **3**, 807, 2007.

[27] A. Alù and N. Engheta: *Wireless at the Nanoscale: Optical Interconnects using Matched Nanoantennas*. Physical Review Letters **104**, 213902, 2010.

[28] K. F. Lee: *Principles of Antenna Theory*. John Wiley & Sons, New York, 1984.

[29] R. P. Feynman: *There's Plenty of Room at the Bottom*. Engineering and Science **23**, 22, 1960.

[30] P. Muhlschlegel, H.-J. Eisler, O. J. F. Martin, B. Hecht, and D. W. Pohl: *Resonant Optical Antennas*. Science **308**, 1607, 2005.

[31] L. Novotny and N. van Hulst: *Antennas for Light*. Nature Photonics **5**, 83, 2011.

[32] G. P. Acuna, F. M. Moeller, P. Holzmeister, S. Beater, B. Lalkens, and P. Tinnefeld: *Fluorescence Enhancement at Docking Sites of DNA-Directed Self-Assembled Nanoantennas*. Science **338**, 506, 2012.

[33] A. Kinkhabwala, Z. Yu, S. Fan, Y. Avlasevich, K. Muellen, and W. E. Moerner: *Large Single-Molecule Fluorescence Enhancements Produced by a Bowtie Nanoantenna*. Nature Photonics **3**, 654, 2009.

[34] E. B. Urena, M. P. Kreuzer, S. Itzhakov, H. Rigneault, R. Quidant, D. Oron, and J. Wenger: *Excitation Enhancement of a Quantum Dot Coupled to a Plasmonic Antenna*. Advanced Materials **24**, OP314, 2012.

[35] A. F. Koenderink: *Single-Photon Nanoantennas*. ACS Photonics **4**, 710, 2017.

[36] S. I. Bogdanov, M. Y. Shalaginov, A. S. Lagutchev, C.-C. Chiang, D. Shah, A. S. Baburin, I. A. Ryzhikov, I. A. Rodionov, A. V. Kildishev, A. Boltasseva, and V. M. Shalaev: *Ultrabright Room-Temperature Sub-Nanosecond Emission from Single Nitrogen-Vacancy Centers Coupled to Nanopatch Antennas*. Nano Letters **18**, 4837, 2018.

[37] T. B. Hoang, G. M. Akselrod, and M. H. Mikkelsen: *Ultrafast Room-Temperature Single Photon Emission from Quantum Dots Coupled to Plasmonic Nanocavities*. Nano Letters **16**, 270, 2016.

[38] T. Kosako, Y. Kadoya, and H. F. Hofmann: *Directional Control of Light by a Nano-Optical Yagi-Uda Antenna*. Nature Photonics **4**, 312, 2010.

[39] J. Dorfmueller, D. Dregely, M. Esslinger, W. Khunsin, R. Vogelgesang, K. Kern, and H. Giessen: *Near-Field Dynamics of Optical Yagi-Uda Nanoantennas*. Nano Letters **11**, 2819, 2011.

[40] A. G. Curto, G. Volpe, T. H. Taminiau, M. P. Kreuzer, R. Quidant, and N. F. van Hulst: *Unidirectional Emission of a Quantum Dot Coupled to a Nanoantenna*. Science **329**, 930, 2010.

[41] C. Sirtori: *Applied physics: Bridge for the Terahertz Gap*. Nature **417**, 132, 2002.

[42] J. C. Prangsma, J. Kern, A. G. Knapp, S. Grossmann, M. Emmerling, M. Kamp, and B. Hecht: *Electrically Connected Resonant Optical Antennas*. Nano Letters **12**, 3915, 2012.

[43] J. Kern, R. Kullock, J. Prangsma, M. Emmerling, M. Kamp, and B. Hecht: *Electrically Driven Optical Antennas*. Nature Photonics **9**, 582, 2015.

[44] J. Lambe and S. L. McCarthy: *Light Emission from Inelastic Electron Tunneling*. Physical Review Letters **37**, 923, 1976.

[45] D. Hone, B. Muehlschlegel, and D. J. Scalapino: *Theory of Light Emission From Small Particle Tunnel Junctions*. Applied Physics Letters **33**, 203, 1978.

[46] S. P. Gurunarayanan, N. Verellen, V. S. Zharinov, F. James Shirley, V. V. Moshchalkov, M. Heyns, J. Van de Vondel, I. P. Radu, and P. Van Dorpe: *Electrically Driven Unidirectional Optical Nanoantennas*. Nano Letters **17**, 7433, 2017.

[47] M. Parzefall, P. Bharadwaj, A. Jain, T. Taniguchi, K. Watanabe, and L. Novotny: *Antenna-coupled photon emission from hexagonal boron nitride tunnel junctions*. Nature Nanotechnology **10**, 1058, 2015.

[48] M. Parzefall and L. Novotny: *Optical antennas driven by quantum tunneling: a key issues review*. Reports on Progress in Physics **82**, 112401, 2019.

[49] A. Stolz, J. Berthelot, M.-M. Mennemanteuil, G. Colas des Francs, L. Markey, V. Meunier, and A. Bouhelier: *Nonlinear Photon-Assisted Tunneling Transport in Optical Gap Antennas*. Nano Letters **14**, 2330, 2014.

[50] H. Qian, S.-W. Hsu, K. Gurunatha, C. T. Riley, J. Zhao, D. Lu, A. R. Tao, and Z. Liu: *Efficient light generation from enhanced inelastic electron tunnelling*. Nature Photonics **12**, 485, 2018.

[51] P. Grimm, S. Zeißner, M. Rödel, S. Wiegand, S. Hammer, M. Emmerling, E. Schatz, R. Kullock, J. Pflaum, and B. Hecht: *Color-Switchable Subwavelength Organic Light-Emitting Antennas*. Nano Letters **22**, 1032, 2022.

[52] S. Simoncelli, Y. Li, E. Cortés, and S. A. Maier: *Nanoscale Control of Molecular Self-Assembly Induced by Plasmonic Hot-Electron Dynamics*. ACS Nano **12**, 2184, 2018.

[53] X. Wu, R. Kullock, E. Krauss, and B. Hecht: *Single-Crystalline Gold Microplates Grown on Substrates by Solution-Phase Synthesis*. Crystal Research and Technology **50**, 595, 2015.

[54] E. Krauss, R. Kullock, X. Wu, P. Geisler, N. Lundt, M. Kamp, and B. Hecht: *Controlled Growth of High Aspect-Ratio Single-Crystalline Gold Platelets*. Crystal Growth & Design, **18**, 1297, 2018.

[55] H. Yagi and S. Uda: *Projector of the Sharpest Beam of Electric Waves*. Proceedings of the Imperial Academy **2**, 49, 1926.

[56] W. Demtroeder: *Experimentalphysik 2*. Springer-Lehrbuch, Springer Berlin Heidelberg, Berlin, Heidelberg, 2009.

[57] D. K. Cheng: *Field and Wave Electromagnetics*. Addison-Wesley, New York, 1989.

[58] L. Novotny: *Effective Wavelength Scaling for Optical Antennas*. Physical Review Letters **98**, 266802, 2007.

[59] J.-S. Huang, J. Kern, P. Geisler, P. Weinmann, M. Kamp, A. Forchel, P. Biagioni, and B. Hecht: *Mode Imaging and Selection in Strongly Coupled Nanoantennas*. Nano Letters **10**, 2105, 2010.

[60] U. Hohenester and A. Trügler: *MNPBEM – A Matlab toolbox for the simulation of plasmonic nanoparticles*. Computer Physics Communications **183**, 370, 2012.

[61] U. Hohenester: *Simulating Electron Energy Loss Spectroscopy With the MNPBEM Toolbox*. Computer Physics Communications **185**, 1177, 2014.

[62] M. Parzefall and L. Novotny: *Light at the End of the Tunnel*. ACS Photonics **5**, 4195, 2018.

[63] P. Anger, P. Bharadwaj, and L. Novotny: *Enhancement and Quenching of Single-Molecule Fluorescence*. Physical Review Letters **96**, 113002, 2006.

[64] J.-S. Huang, T. Feichtner, P. Biagioni, and B. Hecht: *Impedance Matching and Emission Properties of Nanoantennas in an Optical Nanocircuit*. Nano Letters **9**, 1897, 2009.

[65] C. W. Marquardt, S. Grunder, A. Błaszczyk, S. Dehm, F. Hennrich, H. v. Löhneysen, M. Mayor, and R. Krupke: *Electroluminescence from a single nanotube–molecule–nanotube junction*. Nature Nanotechnology **5**, 863, 2010.

[66] T. Mueller, M. Kinoshita, M. Steiner, V. Perebeinos, A. A. Bol, D. B. Farmer, and P. Avouris: *Efficient narrow-band light emission from a single carbon nanotube p–n diode*. Nature Nanotechnology **5**, 27, 2010.

[67] P. Rai, N. Hartmann, J. Berthelot, J. Arocas, G. Colas des Francs, A. Hartschuh, and A. Bouhelier: *Electrical Excitation of Surface Plasmons by an Individual Carbon Nanotube Transistor*. Physical Review Letters **111**, 2013.

[68] E. D. Minot, F. Kelkensberg, M. van Kouwen, J. A. van Dam, L. P. Kouwenhoven, V. Zwiller, M. T. Borgström, O. Wunnicke, M. A. Verheijen, and E. P. A. M. Bakkers: *Single Quantum Dot Nanowire LEDs*. Nano Letters **7**, 367, 2007.

[69] P. Fan, C. Colombo, K. C. Y. Huang, P. Krogstrup, J. Nygård, A. Fontcuberta i Morral, and M. L. Brongersma: *An Electrically-Driven GaAs Nanowire Surface Plasmon Source*. Nano Letters **12**, 4943, 2012.

[70] K. C. Y. Huang, M.-K. Seo, T. Sarmiento, Y. Huo, J. S. Harris, and M. L. Brongersma: *Electrically driven subwavelength optical nanocircuits*. Nature Photonics **8**, 244, 2014.

[71] P. Février and J. Gabelli: *Tunneling time probed by quantum shot noise*. Nature Communications **9**, 4940, 2018.

[72] L. C. Davis: *Theory of Surface-Plasmon Excitation in Metal-Insulator-Metal Tunnel Junctions*. Physical Review B **16**, 2482, 1977.

[73] M. Parzefall and L. Novotny: *Correction to Light at the End of the Tunnel*. ACS Photonics **8**, 682, 2021.

[74] M. Ochs: *Electroluminescence from Optical Yagi-Uda Antennas*. Master's thesis, Julius-Maximilians University of Würzburg, 2017.

[75] H. Qian, S. Li, S.-W. Hsu, C.-F. Chen, F. Tian, A. R. Tao, and Z. Liu: *Highly-efficient electrically-driven localized surface plasmon source enabled by resonant inelastic electron tunneling*. Nature Communications **12**, 3111, 2021.

[76] R. W. Rendell and D. J. Scalapino: *Surface Plasmons Confined by Microstructures on Tunnel Junctions*. Physical Review B **24**, 3276, 1981.

[77] H. F. Hofmann, T. Kosako, and Y. Kadoya: *Design Parameters for a Nano-Optical Yagi-Uda Antenna*. New Journal of Physics **9**, 217, 2007.

[78] https://www.elprocus.com/design-of-yagi-uda-antenna/.

[79] R. L. Olmon, B. Slovick, T. W. Johnson, D. Shelton, S.-H. Oh, G. D. Boreman, and M. B. Raschke: *Optical Dielectric Function of Gold*. Physical Review B **86**, 235147, 2012.

[80] A. Taflove and S. C. Hagness: *Computational Electrodynamics: The Finite-Difference Time-Domain Method*. Artech House, Norwood, 2000.

[81] S. D. Gedney: *An Anisotropic Perfectly Matched Layer-Absorbing Medium for the Truncation of FDTD Lattices*. IEEE Transactions on Antennas and Propagation **44**, 1630, 1996.

[82] S. A. Maier, M. L. Brongersma, P. G. Kik, S. Meltzer, A. a. G. Requicha, and H. A. Atwater: *Plasmonics—A Route to Nanoscale Optical Devices*. Advanced Materials **13**, 1501, 2001.

[83] S. A. Maier, P. G. Kik, H. A. Atwater, S. Meltzer, E. Harel, B. E. Koel, and A. A. G. Requicha: *Local detection of electromagnetic energy transport below the diffraction limit in metal nanoparticle plasmon waveguides*. Nature Materials **2**, 229, 2003.

[84] E. Ozbay: *Plasmonics: Merging Photonics and Electronics at Nanoscale Dimensions*. Science **311**, 189, 2006.

[85] M. Quinten, A. Leitner, J. R. Krenn, and F. R. Aussenegg: *Electromagnetic energy transport via linear chains of silver nanoparticles*. Optics Letters **23**, 1331, 1998.

[86] P. Tuchscherer, C. Rewitz, D. V. Voronine, F. J. G. d. Abajo, W. Pfeiffer, and T. Brixner: *Analytic coherent control of plasmon propagation in nanostructures*. Optics Express **17**, 14235, 2009.

[87] D. K. Gramotnev and S. I. Bozhevolnyi: *Plasmonics beyond the diffraction limit*. Nature Photonics **4**, 83, 2010.

[88] Y. Fu, X. Hu, C. Lu, S. Yue, H. Yang, and Q. Gong: *All-Optical Logic Gates Based on Nanoscale Plasmonic Slot Waveguides*. Nano Letters **12**, 5784, 2012.

[89] H. Ditlbacher, A. Hohenau, D. Wagner, U. Kreibig, M. Rogers, F. Hofer, F. R. Aussenegg, and J. R. Krenn: *Silver Nanowires as Surface Plasmon Resonators*. Physical Review Letters **95**, 257403, 2005.

[90] Y. Fang, Z. Li, Y. Huang, S. Zhang, P. Nordlander, N. J. Halas, and H. Xu: *Branched Silver Nanowires as Controllable Plasmon Routers*. Nano Letters **10**, 1950, 2010.

[91] P. Bharadwaj, A. Bouhelier, and L. Novotny: *Electrical Excitation of Surface Plasmons*. Physical Review Letters **106**, 226802, 2011.

[92] M. Song, A. Bouhelier, P. Bramant, J. Sharma, E. Dujardin, D. Zhang, and G. Colas-des Francs: *Imaging Symmetry-Selected Corner Plasmon Modes in Penta-Twinned Crystalline Ag Nanowires*. ACS Nano **5**, 5874, 2011.

[93] T. Shegai, V. D. Miljković, K. Bao, H. Xu, P. Nordlander, P. Johansson, and M. Käll: *Unidirectional Broadband Light Emission from Supported Plasmonic Nanowires*. Nano Letters **11**, 706, 2011.

[94] Z. Li, K. Bao, Y. Fang, Y. Huang, P. Nordlander, and H. Xu: *Correlation between Incident and Emission Polarization in Nanowire Surface Plasmon Waveguides*. Nano Letters **10**, 1831, 2010.

[95] D.-S. Ly-Gagnon, K. C. Balram, J. S. White, P. Wahl, M. L. Brongersma, and D. A. B. Miller: *Routing and photodetection in subwavelength plasmonic slot waveguides*. Nanophotonics **1**, 9, 2012.

[96] P. M. Krenz, R. L. Olmon, B. A. Lail, M. B. Raschke, and G. D. Boreman: *Near-field measurement of infrared coplanar strip transmission line attenuation and propagation constants*. Optics Express **18**, 21678, 2010.

[97] M. Schnell, P. Alonso-González, L. Arzubiaga, F. Casanova, L. E. Hueso, A. Chuvilin, and R. Hillenbrand: *Nanofocusing of mid-infrared energy with tapered transmission lines*. Nature Photonics **5**, 283, 2011.

[98] P. Then, G. Razinskas, T. Feichtner, P. Haas, A. Wild, N. Bellini, R. Osellame, G. Cerullo, and B. Hecht: *Remote detection of single emitters via optical waveguides*. Physical Review A **89**, 053801, 2014.

[99] I. Taniguchi, K. Toyosawa, H. Yamaguchi, and K. Yasukouchi: *Reversible electrochemical reduction and oxidation of cytochrome c at a bis(4-pyridyl) disulphide-modified gold electrode*. Journal of the Chemical Society, Chemical Communications pp. 1032–1033, 1982.

[100] R. G. Nuzzo and D. L. Allara: *Adsorption of bifunctional organic disulfides on gold surfaces*. Journal of the American Chemical Society **105**, 4481, 1983.

[101] F. Schreiber: *Structure and growth of self-assembling monolayers*. Progress in Surface Science **65**, 151, 2000.

[102] J. C. Love, L. A. Estroff, J. K. Kriebel, R. G. Nuzzo, and G. M. Whitesides: *Self-Assembled Monolayers of Thiolates on Metals as a Form of Nanotechnology*. Chemical Reviews **105**, 1103, 2005.

[103] C. Vericat, M. E. Vela, G. Benitez, P. Carro, and R. C. Salvarezza: *Self-assembled monolayers of thiols and dithiols on gold: new challenges for a well-known system*. Chemical Society Reviews **39**, 1805, 2010.

[104] S. Casalini, C. A. Bortolotti, F. Leonardi, and F. Biscarini: *Self-assembled monolayers in organic electronics*. Chemical Society Reviews **46**, 40, 2017.

[105] M. S. Inkpen, Z.-F. Liu, H. Li, L. M. Campos, J. B. Neaton, and L. Venkataraman: *Non-chemisorbed gold–sulfur binding prevails in self-assembled monolayers*. Nature Chemistry **11**, 351, 2019.

[106] V. Kriegisch and C. Lambert: *Self-Assembled Monolayers of Chromophores on Gold Surfaces*. In F. Würthner (editor), *Supermolecular Dye Chemistry*, Topics in Current Chemistry, pp. 257–313, Springer, Berlin, Heidelberg, 2005.

[107] M. Zharnikov, S. Frey, H. Rong, Y.-J. Yang, K. Heister, M. Buck, and M. Grunze: *The effect of sulfur–metal bonding on the structure of self-assembled monolayers*. Physical Chemistry Chemical Physics **2**, 3359, 2000.

[108] D. A. Egger, F. Rissner, G. M. Rangger, O. T. Hofmann, L. Wittwer, G. Heimel, and E. Zojer: *Self-assembled monolayers of polar molecules on Au(111) surfaces: distributing the dipoles*. Physical Chemistry Chemical Physics **12**, 4291, 2010.

[109] D. J. Lavrich, S. M. Wetterer, S. L. Bernasek, and G. Scoles: *Physisorption and Chemisorption of Alkanethiols and Alkyl Sulfides on Au(111)*. The Journal of Physical Chemistry B **102**, 3456, 1998.

[110] N. A. Kautz and S. A. Kandel: *Alkanethiol/Au(111) Self-Assembled Monolayers Contain Gold Adatoms: Scanning Tunneling Microscopy before and after Reaction with Atomic Hydrogen*. Journal of the American Chemical Society **130**, 6908, 2008.

[111] M. H. Schoenfisch and J. E. Pemberton: *Air Stability of Alkanethiol Self-Assembled Monolayers on Silver and Gold Surfaces*. Journal of the American Chemical Society **120**, 4502, 1998.

[112] K. L. Prime and G. M. Whitesides: *Self-Assembled Organic Monolayers: Model Systems for Studying Adsorption of Proteins at Aurfaces*. Science **252**, 1164, 1991.

[113] J. Rundqvist, J. H. Hoh, and D. B. Haviland: *Poly(ethylene glycol) Self-Assembled Monolayer Island Growth*. Langmuir **21**, 2981, 2005.

[114] R. W. Zehner, B. F. Parsons, R. P. Hsung, and L. R. Sita: *Tuning the Work Function of Gold with Self-Assembled Monolayers Derived from X-[C6H4 -CC-]nC6H4-SH (n = 0, 1, 2; X = H, F, CH3 , CF3 , and OCH3)*. Langmuir **15**, 1121, 1999.

[115] P. C. Rusu and G. Brocks: *Surface Dipoles and Work Functions of Alkylthiolates and Fluorinated Alkylthiolates on Au(111)*. The Journal of Physical Chemistry B **110**, 22628, 2006.

[116] D. M. Alloway, M. Hofmann, D. L. Smith, N. E. Gruhn, A. L. Graham, R. Colorado, V. H. Wysocki, T. R. Lee, P. A. Lee, and N. R. Armstrong:

Interface Dipoles Arising from Self-Assembled Monolayers on Gold: UV-Photoemission Studies of Alkanethiols and Partially Fluorinated Alkanethiols. The Journal of Physical Chemistry B **107**, 11690, 2003.

[117] D. M. Alloway, A. L. Graham, X. Yang, A. Mudalige, R. Colorado, V. H. Wysocki, J. E. Pemberton, T. R. Lee, R. J. Wysocki, and N. R. Armstrong: *Tuning the Effective Work Function of Gold and Silver Using ω-Functionalized Alkanethiols: Varying Surface Composition through Dilution and Choice of Terminal Groups*. The Journal of Physical Chemistry C **113**, 20328, 2009.

[118] B. de Boer, A. Hadipour, M. M. Mandoc, T. van Woudenbergh, and P. W. M. Blom: *Tuning of Metal Work Functions with Self-Assembled Monolayers*. Advanced Materials **17**, 621, 2005.

[119] J. Pflaum, G. Bracco, F. Schreiber, R. Colorado, O. E. Shmakova, T. R. Lee, G. Scoles, and A. Kahn: *Structure and electronic properties of CH3- and CF3-terminated alkanethiol monolayers on Au(111): a scanning tunneling microscopy, surface X-ray and helium scattering study*. Surface Science **498**, 89, 2002.

[120] C. A. Widrig, C. Chung, and M. D. Porter: *The electrochemical desorption of n-alkanethiol monolayers from polycrystalline Au and Ag electrodes*. Journal of Electroanalytical Chemistry and Interfacial Electrochemistry **310**, 335, 1991.

[121] J. J. Calvente, Z. Kováčová, M. D. Sanchez, R. Andreu, and W. R. Fawcett: *Desorption of Spontaneously Adsorbed and Electrochemically Readsorbed 2-Mercaptoethanesulfonate on Au(111)*. Langmuir **12**, 5696, 1996.

[122] T. Kawaguchi, H. Yasuda, K. Shimazu, and M. D. Porter: *Electrochemical Quartz Crystal Microbalance Investigation of the Reductive Desorption of Self-Assembled Monolayers of Alkanethiols and Mercaptoalkanoic Acids on Au*. Langmuir **16**, 9830, 2000.

[123] C. Wälti, R. Wirtz, W. A. Germishuizen, D. M. D. Bailey, M. Pepper, A. P. J. Middelberg, and A. G. Davies: *Direct Selective Functionalization of Nanometer-Separated Gold Electrodes with DNA Oligonucleotides*. Langmuir **19**, 981, 2003.

[124] A. Musgrove, A. Kell, and D. Bizzotto: *Fluorescence Imaging of the Oxidative Desorption of a BODIPY-Alkyl-Thiol Monolayer Coated Au Bead*. Langmuir **24**, 7881, 2008.

[125] E. H. J. Wong, G. L. May, and C. P. Wilde: *Oxidative desorption of thiols as a route to controlled formation of binary self assembled monolayer surfaces*. Electrochimica Acta **109**, 67, 2013.

[126] E. Pensa, C. Vericat, D. Grumelli, R. C. Salvarezza, S. H. Park, G. S. Longo, I. Szleifer, and L. P. M. D. Leo: *New insight into the electrochemical desorption of alkanethiol SAMs on gold*. Physical Chemistry Chemical Physics **14**, 12355, 2012.

[127] R. L. Garrell, J. E. Chadwick, D. L. Severance, N. A. McDonald, and D. C. Myles: *Adsorption of Sulfur Containing Molecules on Gold: The Effect of Oxidation on Monolayer Formation and Stability Characterized by Experiments and Theory*. Journal of the American Chemical Society **117**, 11563, 1995.

[128] I. Utke, P. Hoffmann, and J. Melngailis: *Gas-assisted focused electron beam and ion beam processing and fabrication*. Journal of Vacuum Science & Technology B: Microelectronics and Nanometer Structures **26**, 1197, 2008.

[129] D. R. Strachan, D. E. Smith, D. E. Johnston, T.-H. Park, M. J. Therien, D. A. Bonnell, and A. T. Johnson: *Controlled fabrication of nanogaps in ambient environment for molecular electronics*. Applied Physics Letters **86**, 043109, 2005.

[130] T. Dadosh: *Conductance and Surface-Enhanced Raman Scattering of Single Molecules Utilizing Dimers of Nanoparticles*. Ph.D. thesis, Weizmann Institute of Science, 2008.

[131] T. B. Jones: *Electromechanics of Particles*. Cambridge University Press, New York, 1995.

[132] J. Kern, S. Grossmann, N. V. Tarakina, T. Haeckel, M. Emmerling, M. Kamp, J.-S. Huang, P. Biagioni, J. C. Prangsma, and B. Hecht: *Atomic-Scale Confinement of Resonant Optical Fields*. Nano Letters **12**, 5504, 2012.

[133] W. Melitz, J. Shen, A. C. Kummel, and S. Lee: *Kelvin probe force microscopy and its application*. Surface Science Reports **66**, 1, 2011.

[134] W. Du, T. Wang, H.-S. Chu, and C. A. Nijhuis: *Highly Efficient On-Chip Direct Electronic-Plasmonic Transducers*. Nature Photonics **11**, 623, 2017.

[135] A. Dasgupta, M.-M. Mennemanteuil, M. Buret, N. Cazier, G. Colas-des Francs, and A. Bouhelier: *Optical wireless link between a nanoscale antenna and a transducing rectenna*. Nature Communications **9**, 1992, 2018.

[136] P. Stoliar, R. Kshirsagar, M. Massi, P. Annibale, C. Albonetti, D. M. de Leeuw, and F. Biscarini: *Charge Injection Across Self-Assembly Monolayers in Organic Field-Effect Transistors: Odd-Even Effects*. Journal of the American Chemical Society **129**, 6477, 2007.

[137] M. A. Bartucci, J. Florián, and J. W. Ciszek: *Spectroscopic Evidence of Work Function Alterations Due to Photoswitchable Monolayers on Gold Surfaces*. The Journal of Physical Chemistry C **117**, 19471, 2013.

[138] I. Aprahamian: *The Future of Molecular Machines*. ACS Central Science **6**, 347, 2020.

[139] S. Erbas-Cakmak, D. A. Leigh, C. T. McTernan, and A. L. Nussbaumer: *Artificial Molecular Machines*. Chemical Reviews **115**, 10081, 2015.

[140] T. Mosciatti, P. Greco, T. Leydecker, M. Eredia, F. Biscarini, and P. Samorì: *Asymmetric Injection in Organic Transistors via Direct SAM Functionalization of Source and Drain Electrodes*. ACS Omega **2**, 3502, 2017.

[141] R. D. Piner, J. Zhu, F. Xu, S. Hong, and C. A. Mirkin: *"Dip-Pen" Nanolithography*. Science **283**, 661, 1999.

[142] J. Rundqvist, J. H. Hoh, and D. B. Haviland: *Directed Immobilization of Protein-Coated Nanospheres to Nanometer-Scale Patterns Fabricated by Electron Beam Lithography of Poly(ethylene glycol) Self-Assembled Monolayers*. Langmuir **22**, 5100, 2006.

[143] S. Friebel, J. Aizenberg, S. Abad, and P. Wiltzius: *Ultraviolet lithography of self-assembled monolayers for submicron patterned deposition*. Applied Physics Letters **77**, 2406, 2000.

[144] M. Tencer and P. Berini: *Toposelective Electrochemical Desorption of Thiol SAMs from Neighboring Polycrystalline Gold Surfaces*. Langmuir **24**, 12097, 2008.

[145] A. Liscio, E. Orgiu, J. M. Mativetsky, V. Palermo, and P. Samorì: *Bottom-Up Fabricated Asymmetric Electrodes for Organic Electronics*. Advanced Materials **22**, 5018, 2010.

[146] R. L. Wells and T. Fort: *Adsorption of water on clean gold by measurement of work function changes*. Surface Science **32**, 554, 1972.

[147] Y. S. Chi, H. R. Byon, B. S. Lee, B. Kong, H. C. Choi, and I. S. Choi: *Polymeric Rulers: Distance-Dependent Emission Behaviors of Fluorophores on Flat Gold Surfaces and Bioassay Platforms Using Plasmonic Fluorescence Enhancement*. Advanced Functional Materials **18**, 3395, 2008.

[148] N. Crivillers, S. Osella, C. Van Dyck, G. M. Lazzerini, D. Cornil, A. Liscio, F. Di Stasio, S. Mian, O. Fenwick, F. Reinders, M. Neuburger, E. Treossi, M. Mayor, V. Palermo, F. Cacialli, J. Cornil, and P. Samorì: *Large Work Function Shift of Gold Induced by a Novel Perfluorinated Azobenzene-Based Self-Assembled Monolayer*. Advanced Materials **25**, 432, 2013.

[149] Y. Aeschi, S. Drayss-Orth, M. Valášek, F. Raps, D. Häussinger, and M. Mayor: *Assembly of [2]Rotaxanes in Water*. European Journal of Organic Chemistry **2017**, 4091, 2017.

[150] L. Jucker, Y. Aeschi, and M. Mayor: *Aqueous assembly of a (pseudo)rotaxane with a donor–π–acceptor axis formed by a Knoevenagel condensation*. Organic Chemistry Frontiers **8**, 4399, 2021.

[151] Y. Aeschi, L. Jucker, D. Häussinger, and M. Mayor: *Slow Formation of Pseudorotaxanes in Water*. European Journal of Organic Chemistry **2019**, 3384, 2019.

[152] D. L. Lyutov, K. V. Genkov, A. D. Zyapkov, G. G. Tsutsumanova, A. N. Tzonev, L. G. Lyutov, and S. C. Russev: *Synthesis and structure of large single crystalline silver hexagonal microplates suitable for micromachining*. Materials Chemistry and Physics **143**, 642, 2014.

[153] C.-Y. Wang, H.-Y. Chen, L. Sun, W.-L. Chen, Y.-M. Chang, H. Ahn, X. Li, and S. Gwo: *Giant colloidal silver crystals for low-loss linear and nonlinear plasmonics*. Nature Communications **6**, 7734, 2015.

[154] C. Schörner, S. Adhikari, and M. Lippitz: *A Single-Crystalline Silver Plasmonic Circuit for Visible Quantum Emitters*. Nano Letters **19**, 3238, 2019.

[155] A. P. Francisco, D. Botequim, D. M. F. Prazeres, V. V. Serra, S. M. B. Costa, C. A. T. Laia, and P. M. R. Paulo: *Extreme Enhancement of Single-Molecule Fluorescence from Porphyrins Induced by Gold Nanodimer Antennas*. The Journal of Physical Chemistry Letters **10**, 1542, 2019.

[156] L. B. Kish: *End of Moore's law: thermal (noise) death of integration in micro and nano electronics*. Physics Letters A **305**, 144, 2002.

[157] I. S. Maksymov, I. Staude, A. E. Miroshnichenko, and Y. S. Kivshar: *Optical Yagi-Uda nanoantennas*. Nanophotonics **1**, 65, 2012.

[158] K.-M. See, F.-C. Lin, T.-Y. Chen, Y.-X. Huang, C.-H. Huang, A. T. M. Yeşilyurt, and J.-S. Huang: *Photoluminescence-Driven Broadband Transmitting Directional Optical Nanoantennas*. Nano Letters **18**, 6002, 2018.

[159] J. Ho, Y. H. Fu, Z. Dong, R. Paniagua-Dominguez, E. H. H. Koay, Y. F. Yu, V. Valuckas, A. I. Kuznetsov, and J. K. W. Yang: *Highly Directive Hybrid Metal–Dielectric Yagi-Uda Nanoantennas*. ACS Nano **12**, 8616, 2018.

[160] D. Emerson: *The gain of an endfire array*. AARL Antenna Compendium **5**, 87, 1996.

[161] G. J. Burke and A. J. Pogio: *Numerical Electromagnetics Code (NEC)-Method of Moments. A User-Oriented Computer Code for Analysis of the Electromagnetic Response of Antennas and Other Metal Structures. Part 1: Program Description-Theory. Part 2: Program Description-Code. Volume 1. Revised*. Technical Report UCID 18834, Lawrence Livermore National Laboratory, 1981, accessible via https://apps.dtic.mil/docs/citations/ADA956129.

[162] T. C. A. Molteno: *NEC2++: An NEC-2 compatible Numerical Electromagnetics Code*. Electronics Technical Report 2014-3, University of Otago, Dunedin, New Zealand, 2014, code from https://github.com/tmolteno/necpp.

[163] Z. Yuan, B. E. Kardynal, R. M. Stevenson, A. J. Shields, C. J. Lobo, K. Cooper, N. S. Beattie, D. A. Ritchie, and M. Pepper: *Electrically Driven Single-Photon Source*. Science **295**, 102, 2002.

[164] X. Shi, D. V. Verschueren, and C. Dekker: *Active Delivery of Single DNA Molecules into a Plasmonic Nanopore for Label-Free Optical Sensing*. Nano Letters **18**, 8003, 2018.

[165] A. V. Uskov, J. B. Khurgin, I. E. Protsenko, I. V. Smetanin, and A. Bouhelier: *Excitation of plasmonic nanoantennas by nonresonant and resonant electron tunnelling*. Nanoscale **8**, 14573, 2016.

[166] M. W. Knight, H. Sobhani, P. Nordlander, and N. J. Halas: *Photodetection with Active Optical Antennas*. Science **332**, 702, 2011.

[167] Z. Fang, Z. Liu, Y. Wang, P. M. Ajayan, P. Nordlander, and N. J. Halas: *Graphene-Antenna Sandwich Photodetector*. Nano Letters **12**, 3808, 2012.

[168] D. Chi, K. E. J. Goh, and A. T. S. Wee: *2D Semiconductor Materials and Devices*. Elsevier, San Diego, 2019.

[169] S. Manzeli, D. Ovchinnikov, D. Pasquier, O. V. Yazyev, and A. Kis: *2D transition metal dichalcogenides*. Nature Reviews Materials **2**, 1, 2017.

[170] K. Han, G. H. Ahn, J. Cho, D.-H. Lien, M. Amani, S. B. Desai, G. Zhang, H. Kim, N. Gupta, A. Javey, and M. C. Wu: *Bright electroluminescence in*

ambient conditions from WSe2 p-n diodes using pulsed injection. Applied Physics Letters **115**, 011103, 2019.

[171] J. S. Ross, P. Klement, A. M. Jones, N. J. Ghimire, J. Yan, D. G. Mandrus, T. Taniguchi, K. Watanabe, K. Kitamura, W. Yao, D. H. Cobden, and X. Xu: *Electrically tunable excitonic light-emitting diodes based on monolayer WSe2 p–n junctions*. Nature Nanotechnology **9**, 268, 2014.

[172] N. R. Pradhan, J. Ludwig, Z. Lu, D. Rhodes, M. M. Bishop, K. Thirunavukkuarasu, S. A. McGill, D. Smirnov, and L. Balicas: *High Photoresponsivity and Short Photoresponse Times in Few-Layered WSe2 Transistors*. ACS Applied Materials & Interfaces **7**, 12080, 2015.

[173] B. W. H. Baugher, H. O. H. Churchill, Y. Yang, and P. Jarillo-Herrero: *Optoelectronic devices based on electrically tunable p–n diodes in a monolayer dichalcogenide*. Nature Nanotechnology **9**, 262, 2014.

[174] M. M. Petrić, M. Kremser, M. Barbone, A. Nolinder, A. Lyamkina, A. V. Stier, M. Kaniber, K. Müller, and J. J. Finley: *Tuning the Optical Properties of a MoSe $_2$ Monolayer Using Nanoscale Plasmonic Antennas*. Nano Letters **22**, 561, 2022.

[175] S. Butun, S. Tongay, and K. Aydin: *Enhanced Light Emission from Large-Area Monolayer MoS2 Using Plasmonic Nanodisc Arrays*. Nano Letters **15**, 2700, 2015.

[176] J. Kern, A. Trügler, I. Niehues, J. Ewering, R. Schmidt, R. Schneider, S. Najmaei, A. George, J. Zhang, J. Lou, U. Hohenester, S. Michaelis de Vasconcellos, and R. Bratschitsch: *Nanoantenna-Enhanced Light–Matter Interaction in Atomically Thin WS2*. ACS Photonics **2**, 1260, 2015.

[177] J. Kern, I. Niehues, P. Tonndorf, R. Schmidt, D. Wigger, R. Schneider, T. Stiehm, S. Michaelis de Vasconcellos, D. E. Reiter, T. Kuhn, and R. Bratschitsch: *Nanoscale Positioning of Single-Photon Emitters in Atomically Thin WSe2*. Advanced Materials **28**, 7101, 2016.

[178] W. Wang, A. Klots, D. Prasai, Y. Yang, K. I. Bolotin, and J. Valentine: *Hot Electron-Based Near-Infrared Photodetection Using Bilayer MoS2*. Nano Letters **15**, 7440, 2015.

[179] T.-Y. Chen, J. Obermeier, T. Schumacher, F.-C. Lin, J.-S. Huang, M. Lippitz, and C.-B. Huang: *Modal Symmetry Controlled Second-Harmonic Generation by Propagating Plasmons*. Nano Letters **19**, 6424, 2019.

[180] X. Wu, P. Jiang, G. Razinskas, Y. Huo, H. Zhang, M. Kamp, A. Rastelli, O. G. Schmidt, B. Hecht, K. Lindfors, and M. Lippitz: *On-Chip Single-Plasmon Nanocircuit Driven by a Self-Assembled Quantum Dot*. Nano Letters **17**, 4291, 2017.

[181] W.-H. Dai, F.-C. Lin, C.-B. Huang, and J.-S. Huang: *Mode Conversion in High-Definition Plasmonic Optical Nanocircuits*. Nano Letters **14**, 3881, 2014.

[182] D. M. Koller, A. Hohenau, H. Ditlbacher, N. Galler, F. Reil, F. R. Aussenegg, A. Leitner, E. J. W. List, and J. R. Krenn: *Organic plasmon-emitting diode*. Nature Photonics **2**, 684, 2008.

[183] P. Neutens, L. Lagae, G. Borghs, and P. Van Dorpe: *Electrical Excitation of Confined Surface Plasmon Polaritons in Metallic Slot Waveguides*. Nano Letters **10**, 1429, 2010.

[184] W. Du, T. Wang, H.-S. Chu, L. Wu, R. Liu, S. Sun, W. K. Phua, L. Wang, N. Tomczak, and C. A. Nijhuis: *On-chip molecular electronic plasmon sources based on self-assembled monolayer tunnel junctions*. Nature Photonics **10**, 274, 2016.

[185] C. Zhang, J.-P. Hugonin, A.-L. Coutrot, C. Sauvan, F. Marquier, and J.-J. Greffet: *Antenna surface plasmon emission by inelastic tunneling*. Nature Communications **10**, 4949, 2019.

[186] W. Du, Y. Han, H. Hu, H.-S. Chu, H. V. Annadata, T. Wang, N. Tomczak, and C. A. Nijhuis: *Directional Excitation of Surface Plasmon Polaritons via Molecular Through-Bond Tunneling across Double-Barrier Tunnel Junctions*. Nano Letters **19**, 4634, 2019.

[187] F. Wang, Y. Liu, T. X. Hoang, H.-S. Chu, S.-J. Chua, and C. A. Nijhuis: *CMOS-Compatible Electronic–Plasmonic Transducers Based on Plasmonic Tunnel Junctions and Schottky Diodes*. Small **18**, 2105684, 2022.

[188] M. Rycenga, C. M. Cobley, J. Zeng, W. Li, C. H. Moran, Q. Zhang, D. Qin, and Y. Xia: *Controlling the Synthesis and Assembly of Silver Nanostructures for Plasmonic Applications*. Chemical Reviews **111**, 3669, 2011.

[189] Y.-T. Hung, C.-B. Huang, and J.-S. Huang: *Plasmonic mode converter for controlling optical impedance and nanoscale light-matter interaction*. Optics Express **20**, 20342, 2012.

[190] A. Calà Lesina, D. Goodwill, E. Bernier, L. Ramunno, and P. Berini: *Tunable Plasmonic Metasurfaces for Optical Phased Arrays*. IEEE Journal of Selected Topics in Quantum Electronics **27**, 1, 2021.

[191] C. Schörner: *Crystalline Silver Plasmonic Nanocircuitry for Efficient Coupling with Single Organic Molecules*. Ph.D. thesis, University of Bayreuth, 2021.

[192] G. V. Naik, V. M. Shalaev, and A. Boltasseva: *Alternative Plasmonic Materials: Beyond Gold and Silver*. Advanced Materials **25**, 3264, 2013.

[193] M. T. Sheldon, J. van de Groep, A. M. Brown, A. Polman, and H. A. Atwater: *Plasmoelectric potentials in metal nanostructures*. Science **346**, 828, 2014.

[194] M. R. Bionta, F. Ritzkowsky, M. Turchetti, Y. Yang, D. Cattozzo Mor, W. P. Putnam, F. X. Kärtner, K. K. Berggren, and P. D. Keathley: *On-chip sampling of optical fields with attosecond resolution*. Nature Photonics **15**, 456, 2021.

[195] M. Ludwig, G. Aguirregabiria, F. Ritzkowsky, T. Rybka, D. C. Marinica, J. Aizpurua, A. G. Borisov, A. Leitenstorfer, and D. Brida: *Sub-femtosecond electron transport in a nanoscale gap*. Nature Physics **16**, 341, 2019.

Acknowledgments

I would like to take this opportunity to thank all the people who have supported me during my research and beyond.

First, I would like to thank **Prof. Dr. Bert Hecht** for his guidance and supervision throughout the last years. I really appreciate the freedom I was given to work on a variety of interesting projects. I also thank **Prof. Dr. Marcel Mayor** and **Prof. Dr. Jens Pflaum** for further discussions and their co-supervision. The working atmosphere has always been pleasant and I enjoyed working with you very much.

This thesis would not have been possible without the help of **Laurent Jucker**, with whom I had endless discussions about chemistry, molecular machines and site-selective functionalization, as well as **Luka Zurak** and **Philipp Grimm**, whose simulations are integral part of my dissertation and the corresponding papers.

My thanks go to **Dr. René Kullock**, who had worked with me since my master's thesis and built most of the setups used in this work. Moreover, I thank **Monika Emmerling**, who prepared electrode structures for me and took care of the clean room.

I would like to thank the entire **Nano-Optics Group**; I really enjoyed being part of this team.
Special thanks go to my colleagues and friends **Luka Zurak**, **Patrick Pertsch**, **Jessica Meier** and **Enno Schatz** for all the successful and unsuccessful group projects, the scientific and non-scientific discussions, and, of course, the occasional *Stammtisch*.

Finally, the continuous support of my **family** has made the last four years so much easier. Thanks to my **parents**, my **brother** and my **grandparents** for all the help outside of work. A special thank you goes to my girlfriend **Ezgi**. Your mental support and encouragement has been indispensable over the last years.

We will see what happens next